Investigating the use of C-band phase closure data to produce soil moisture maps

Nikiforos Koliolios

Delft University of Technology

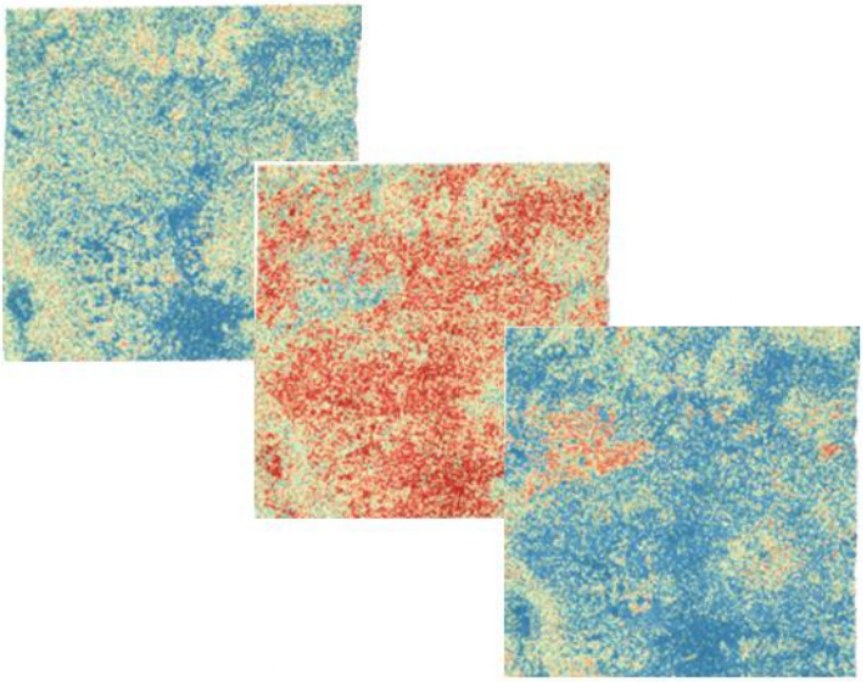

TU Delft Delft University of Technology

Challenge the future

Investigating the use of C-band phase closure data to produce soil moisture maps

by

Nikiforos Koliolios

in partial fulfillment of the requirements for the degree of

Master of Science
in Civil Engineering

at the Delft University of Technology,
to be defended publicly on Friday January 31, 2020 at 3:00 pm.

Supervisor:	Prof. dr. ir. R. F. Hanssen,	TU Delft, Geoscience and Remote Sensing
Thesis committee:	Prof. dr. ir. J. F. Lopez-Dekker,	TU Delft, Geoscience and Remote Sensing
	Prof.dr. S. Steele-Dunn,	TU Delft, Geoscience and Remote Sensing
Daily supervisor:	ir. F. M. G. Heuff,	TU Delft, Geoscience and Remote Sensing

Delft
University of
Technology

Abstract

Soil Moisture is a key hydrological variable since it controls the interactions between the atmosphere, biosphere and hydrosphere. It is responsible for the partitioning of precipitation into evaporation, transpiration, percolation and run-off. Soil Moisture monitoring is used to indicate droughts in vegetated areas and is an important parameter to early warning systems for flood. Therefore, throughout the years human population attempted to monitor and control it. The advent of Remote Sensing, during the past decades, enormously influenced soil moisture research by enabling acquisition of large scale data. Many Remote Sensing systems were developed exclusively to study this variable.

Land subsidence, triggered both by human activity and natural processes, is another phenomenon whose monitoring is crucial for the environment and the human populationa and is thus an essential variable which needs to be continuously monitored in vulnerable areas, since it can damage buildings' foundations. Remote Sensing and more specifically Microwave remote sensing has been pivotal in studying land deformation and subsidence in near real time. Detecting and monitoring land subsidence and deformation with InSAR method has been meticulously researched however there are still obstacles to overcome such as vegetation.

The aim of this research is to study whether InSAR closure phases can be used to detect moisture changes. The idea of using closure phases for soil moisture estimation was proposed by De Zan, Parizzi, et al. 2013 and further studied by Zwieback, Hensley, and Hajnsek 2015a. The closure phase inversion model of De Zan and Gomba 2018 is implemented in this thesis using Sentinel-1 C-band for the inversion and SMAP data for the evaluation of the results. The results support the idea that this method has potential over bare soil and low vegetated areas but struggles to overcome vegetation due to its limited penetration capability. Furthermore, soil moisture changes may introduce a systematic error to land subsidence measurements. For this reason, the idea was to make use of the generated soil moisture data to produce interferometric phase corrections over the study areas. However, the results are inconclusive due to the poor quality of the data over vegetated areas.

Preface

This thesis is the product of several months of dedication to research and it marks the end of my MSc studies at the track of Water Management. I would like to express my gratitude to everyone who helped and supported me during this period.

First, I would like to thank my daily supervisor Floris Heuff who introduced me and guided me through the field of microwave remote sensing. I would like to thank Prof. Ramon Hanssen who provided me the opportunity to work on this interesting topic, for his feedback, the knowledge he imparted to me, his patience and his interest in my progress especially when i failed to bring him up to date due to being lost in a mountain of code.

My sincere thanks go to Prof. Susan Steele-Dunne for reading through my thesis and for her insightful comments on it. The feedback I received was invaluable and I am grateful for her contribution. Last but not least, I would also like to express my gratitude to Prof. Paco Lopez-Dekker for his insightful feedback and eagerness to help me during this period

During the MSc studies and my stay in the Netherlands, I got to meet countless new people as well as make new friends who supported me emotionally throughout my studies and spent a lot of time together with me studying and having fun (often combining those two). Many of them I now consider family and I, therefore, feel obliged to express my deepest gratitude to Dimitris, Dionysia, Giorgos Ch, Giorgos Tz, Vasilis, Eleni & Konstantinos for filling those years with joy, laughter and happy memories. Dimitris and Dionysia were my fellow neighbours with whom I spent endless hours studying together, relaxing after a stressful day at the university and discussing over a warm cup of coffee. Giorgos Ch. is the mastermind behind the adventures all over Europe, Vassilis and Konstantinos were always eager to listen to my worries regarding my research and help me think out of the box. Eleni is always there to discuss and offer us counselling. Giorgos Tz. is always there to lighten the mood. I would also like to thank Jasper and Ingo for turning the multidisciplinary project in Nepal, into an unforgettable experience. I will never forget the time we spent together brainstorming working overtime as well as our endless conversations at our balcony during the evening. Lots of thanks should also be given to my friends back in Greece who supported me throughout my studies.

Last but not least, I would like to thank and say a few words about my parents Nikos and Antigoni and sister Dimitra for their moral support and unconditional love throughout my whole life and academic career. It goes without saying that without you I wouldn't have been able to study in TU Delft, pursue my dreams and be the person I am.

Nikiforos Koliolios
Delft, January 2020

Contents

List of Figures ix

1 Introduction 1
- 1.1 Research motivation . . . 1
- 1.2 Introduction to Microwave Remote Sensing . . . 2
  - 1.2.1 Introduction to InSAR . . . 3
- 1.3 Problem Statement and Objectives . . . 3
  - 1.3.1 Research question . . . 3
- 1.4 Research Questions . . . 4
  - 1.4.1 Thesis outline . . . 5

2 Background Information 7
- 2.1 Soil Moisture . . . 7
  - 2.1.1 Soil Moisture & Microwave Remote Sensing . . . 7
  - 2.1.2 Climatology and atmospheric moisture . . . 8
  - 2.1.3 Hydrology . . . 9
  - 2.1.4 Geomorphology & Biogeography . . . 10
- 2.2 SAR Remote Sensing . . . 11
  - 2.2.1 SAR Principles . . . 11
  - 2.2.2 Interferometric SAR (InSAR) . . . 12
  - 2.2.3 Decorrellation in InSAR . . . 14
  - 2.2.4 Closure phase & ensuing ambiguities . . . 16
- 2.3 Study Areas . . . 19
  - 2.3.1 Mexico . . . 19
  - 2.3.2 Netherlands . . . 20

3 Methodology 25
- 3.1 Data acquisition & pre-processing . . . 25
  - 3.1.1 Data used . . . 26
  - 3.1.2 Orbital information . . . 26
  - 3.1.3 Coregistration & ESD . . . 27
  - 3.1.4 Terrain Correction . . . 27
  - 3.1.5 Multilook . . . 27
- 3.2 Propagation Model . . . 28
  - 3.2.1 Microwave incidence and refraction . . . 28
  - 3.2.2 Dielectric constant of soil . . . 30
- 3.3 Replication of the closure phase inversion method . . . 31
  - 3.3.1 Initial optimization of the inversion algorithm . . . 31
  - 3.3.2 Solving the ambiguity . . . 33
  - 3.3.3 Final moisture results & conversion to interferometric variables . . . 34
- 3.4 Evaluation of soil moisture product . . . 35

4 Results **37**
4.1 SAR Parameters 37
4.2 Inversion algorithm 41
4.3 Inverted moisture results & validation 44
  4.3.1 Mexico Model 1 44
  4.3.2 Mexico Model 2 49
  4.3.3 Holland Physical & Simplified Model 50
4.4 Interferometric phase corrections 55

5 Conclusions & Recommendations **57**
5.1 Conclusions 57
5.2 Recommendations 58

List of Figures

1.1 Land subsidence map of the Netherlands (left), the area around Delft and Delfland (middle) and the given legend (right) (bodemdalingskaart.nl) (total) (Bodemdalingskaart 2018) . . . 2

2.1 Global energy balance from (Physics of Evaporation) by (A.M.J. Coenders-Gerrits) 8
2.2 Average continental evaporation and precipitation recycling ratios . . . 9
2.3 Layout of a lumped conceptual model. P is precipitation, E is evapotranspiration while S_u and $S_{u,max}$ are the current and the maximum storage respectively in the unsaturated zone. R_f is runoff and R_s is slow response (infiltration) (Aalbers 2015) . . . 9
2.4 Imaging geometry of a side-looking SAR. (Engdahl et al. 2013) . . . 12
2.5 Geometrical configuration of repeat-pass SAR interferometry. Sat1 and Sat2 are the master and slave acquisitions respectively, while B is the baseline, θ_0 is the look or squint angle, i_0 is the incidence angle and ρ is the slant range . (Tobita et al. 1998) . . . 13
2.6 Interferometric phase maps of the isle of Leykada, Greece before (left) and after (right) the 2015's earthquake. The earthquake induced deformation phase is clearly visible as several concentric fringes forming around the epicentre. A deformation of 28,5cm was estimated using InSAR data (own work). . . . 14
2.7 Examples of consistency on a flat plane (left) and inconsistency on a non-flat one (right) (De Zan, Zonno, and López-Dekker 2015) . . . 18
2.8 Different soil moisture (bare soil case) time series yielding similar closure phase, indicating the issue of ambiguity (Zwieback, Hensley, and Hajnsek 2017) . . . 19
2.9 The study area as seen from Google Earth (a) and its land types as detected by ESA. Red is urban, Yellow is cropland, White is bare soil and Green is forest (ESA CCI Land Cover). . . . 20
2.10 The Trans-Mexican volcanic belt and the location of the study area (Ferrari 2003) . . . 21
2.11 Average monthly Precipitation (a) and Temperature (b) at the Valley of Puebla (climate-data.org n.d.) . . . 21
2.12 Above and below sea level (a) (Actueel Hoogtebestand Nederland n.d.) and soil types in the Netherlands (b) (Brus, Lame, and Nieuwenhuis 2009). . . . 22
2.13 Land cover types located at the study area (Copernicus-Land Monitoring Service 2015) . . . 23
2.14 Example of a borehole log profile (DINOloket n.d.) . . . 23
2.15 Average monthly Precipitation (a) and Temperature (b) in the area of interest (climate-data.org n.d.) . . . 24

3.1 This chart shows the sequence of the processes leading up to the analysis of the phase closures. The circled part is presented in chapter 3.2 but is included for the sake of presenting the whole picture. . . . 25
3.2 Geometry of topographical distortions in SAR imagery (STEP ESA n.d.). . . . 28

3.3 Probability density functions for different coherence levels. Slimmer curves correspond to highest coherence. L is the number of multi looked images (R. F. Hanssen 2001). . . . 28
3.4 Wave propagation and scattering profile of a lossy medium (De Zan, Parizzi, et al. 2013) . . . 29
3.5 Complex dielectric constant values for different organic matter content as modelled by the semi empirical model by (J. Liu et al. 2013) . . . 31
3.6 Process scheme of the inversion algorithm . . . 32
3.7 Example of a circularly permutated moisture order. Finding the link between wettest and driest is the key to solve the ambiguity. . . . 33
3.8 Example of ambiguity solution. Coherence plots for two maximum candidates 1 (a) and 7 (b) . . . 34
3.9 Example of world map SMAP L4 surface moisture imaging. . . . 35
3.10 Annual cycles of daily precipitation (mm/d) for Delft (left) and Zegveld (right) documented by the KNMI stations located at the respective areas. The daily timeseries were used to evaluate the implementation of the soil moisture inversion (Koninklijk Nederlands Meteorologisch Instituut 2019) . . . 36

4.1 Coherence maps of the study area in Mexico at four different time stamps. For the sake of consistency, for all four maps displayed, SLCs with an interval of 12 days were used . . . 38
4.2 Coherence maps of the study area in the Netherlands at two different time stamps both with a time interval of 12 days . . . 38
4.3 Closure phase maps of the study area in Mexico at four different time stamps. 1a low levels of closure phase is related to low monthly precipitation, especially when compared wwith 1b which lies in the middle of Mexico's wet season . . . 39
4.4 Closure phase maps of the study area in the Netherlands at four different time stamps. . . . 40
4.5 Antecedent precipitation estimated by using data provided by KNMI. The sensors in Delft and Zegveld have a correlation rate of 0.88 . . . 40
4.6 Left: The Soil Moisture time series as observed by SMAP and two ground sensors at Zegveld, Netherlands. Both sensors were deactivated from 10/8 to 22/8, hence the absence of measurements. Right: The corresponding scatter plot. 41
4.7 Single pixel moisture sequences estimated by the minimization algorithm in the 11 acquisition Mexico model, with random initial values. Each run of the minimization algorithm may result in a correct sequence, a circularly equivalent one or a completely different one. . . . 43
4.8 Single pixel moisture sequences estimated by the minimization algorithm in the 6 acquisition Mexico model, with random initial values. Each run of the minimization algorithm may result in a correct sequence, a circularly equivalent one or a completely different one. . . . 43
4.9 Comparison of Mexico inversion results with validation data (SMAP). . . . 44
4.10 The region of Puebla and its land types as detected by ESA. Red is urban, Yellow is cropland, White is bare soil and Green is forest (ESA CCI Land Cover). 45
4.11 Histograms of the decorrelation rate τ for the different land cover types. . . . 45
4.12 Volumetric Soil Moisture (m^3/m^3) inversion results for the 11 acquisition Mexico model. . . . 47
4.13 Index of the image with the highest moisture level per pixel. . . . 48

4.14 Mexico inversion results for different land types and their respective SMAP values. Cropland 1 refers to the major cropland, while Cropland 2 refers to the northwest region. 48
4.15 Comparison of Mexico Model 2 inversion results with validation data (SMAP). 49
4.16 Volumetric Soil Moisture (m^3/m^3) inversion results for the 6 acquisition Mexico model 49
4.17 Mexico inversion results for different land types and their respective SMAP values. Cropand 1 refers to the major cropland, while Cropland 2 refers to the northwest region. 50
4.18 Inversion results for the three different land types and their respective SMAP values. 51
4.19 Volumetric Soil Moisture (m^3/m^3) inversion results for the 11 acquisition Physical Holland model 52
4.20 Volumetric Soil Moisture (m^3/m^3) inversion results for the 11 acquisition Simplified Holland model 53
4.21 Comparison of the Physical (a) and the Simplified (b) Holland model inversion results with the available validation data (SMAP). 54
4.22 Histograms of the decorrelation rate τ for the different land cover types. 54
4.23 The region of Netherlands studied and its land types as detected by (Copernicus-Land Monitoring Service 2015). The water bodies studied are circled. 55
4.24 Compensated interferometric phase (mean Dlos = 0.47mm)(a) and (mean Dlos = -0.14mm) (b) 55
4.25 Total moisture induced displacement 56
4.26 Compensated interferometric phase (mean Dlos = 0.47mm)(a) and Total moisture induced displacement (b) 56

1

Introduction

Soil moisture content (SMC) is a key hydrological and climatic variable in various applications domain (Paloscia et al. 2013) and responds dynamically to sequences of the complex processes in the soil. Soil moisture is one of the most important general characteristics of the soil and has an extremely variable value over time and space. Soil moisture which in essence is the water than is held in the soil within reach of the plants' roots controls the interactions among the atmosphere, biosphere and hydrosphere (Wagner, Lemoine, and Rott 1999). Changes in soil moisture may trigger or accelerate multiple processes on the land surface such as flood events, landslides and land subsidence, the latter being the most important for the present thesis. Apart from the effect on the aforementioned processes, soil moisture changes may induce systematic errors and bias to the spatial and temporal patterns of land deformation measurements, produced by microwave remote sensing, which are not yet well studied and understood (Zwieback, Hensley, and Hajnsek 2015b). Consequently, its monitoring is of utmost importance to a wide range of scientific disciplines, such as hydrology, geohydrology, geology etc.

1.1. Research motivation

Land subsidence is a prevailing issue in many areas all around the world, with many of them being in coastal areas close to river deltas. There is both human and non-human induced land-subsidence. Pair that with an increase of the mean sea level globally and the issue is becoming even more apparent. The Netherlands is a prime example of that where land subsidence due to anthropogenic (groundwater extraction), geochemical (peat oxidation) geological subsidence in tandem with sea level rise, pose a threat to the inhabitants. In a sense, Netherlands is a fertile ground for land subsidence studies as different areas are subjected to subsidence stemming from different human or non-human induced processes.

Figure 1.1 presents the current situation for the whole of the Netherlands as well as for the area of Delft and Delfland. At the north of the country lies the Groningen gas field, Europe's largest gas field. The extraction of gas reduces the pressure of the underground chamber leading to its compaction and subsequent land subsidence on the ground above. Due to its close proximity to the sea and the looming dangers, the rate of subsidence is put under close inspection (Thienen-Visser, Pruiksma, and Breunese 2015). The western part of the Netherlands came to be habitable from the reclamation of peatlands and lakes. This kind of drainage exposed peat to aerobic conditions leading to its oxidization. Nowadays the subsidence continues in rural areas because of groundwater extraction causing peat oxidization and in urban areas due to soil consolidation.

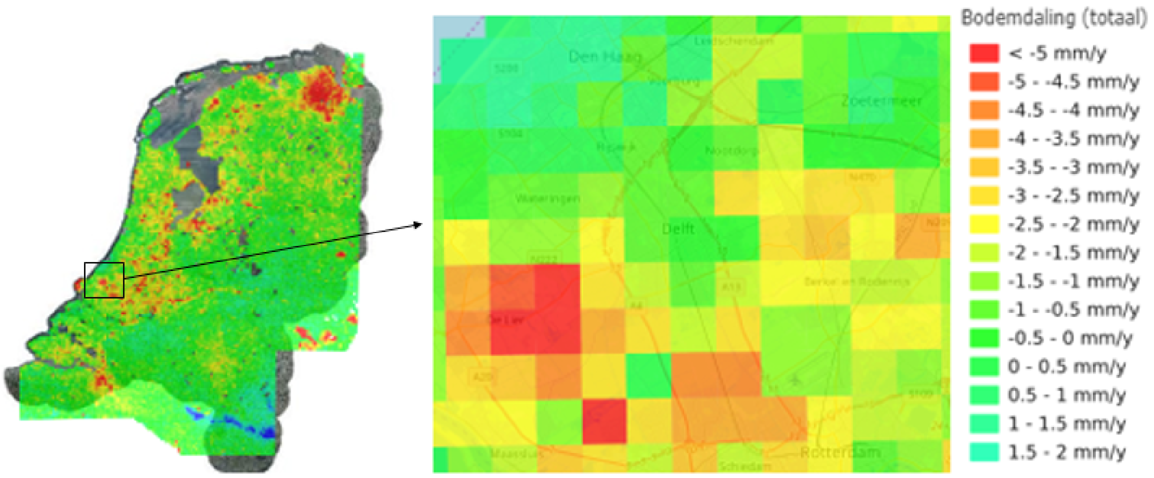

Figure 1.1: Land subsidence map of the Netherlands (left), the area around Delft and Delfland (middle) and the given legend (right) (bodemdalingskaart.nl) (total) (Bodemdalingskaart 2018)

Throughout the years different technologies have been implemented to detect and quantify land subsidence, the most common being remote sensing techniques. Soil moisture and its temporal variability is one of the components affecting the quality of said techniques. The focus of this research will primarily be to investigate whether microwave remote sensing can be used to initially estimate soil moisture and then examine the possibility of using the generated soil moisture data to correct land subsidence measurements.

1.2. Introduction to Microwave Remote Sensing

Remote sensing is the science of studying elements on the surface of the Earth without making in situ contact with them. Different remote sensing methods have been developed over the years in order to be implemented in a vast array of science disciplines and other fields, from cartography, ecology and earthquake geology to military spying activities and even locating houses without a building permit.

Remote sensing systems employ sensors which operate on certain ranges of the electromagnetic spectrum. On one hand, systems making use of visible, near infrared nd shortwave infrared sensors are classified as optical remote sensing. On the other hand, those operating on the microwave wavelength region are classified as microwave remote sensing. Remote sensing systems are usually mounted on either satellite, planes and even drones or rails (Ground Based SAR). All microwave systems fall under two categories, passive and active.

The passive sensors receive radiation from two sources: sunlight radiation reflected from the surface of the Earth and radiation emitted by the object themselves depending on the physical attributes of the object. Passive methods are usually applied for the detection of snowmelt but also for soil moisture. Active sensors emit their own energy in the form of an electromagnetic wave and then receive the reflected radiation which is backscattered by the different objects it comes in contact with. Active microwave systems are independent of external energy sources, while both active and passive systems have the ability to penetrate clouds depending on the wavelength they operate. Hence they can be used to retrieve images at all times and in all weather conditions. Backscatter from targets on the ground depends both on physical parameters such as geometric shape, surface roughness, dielectric properties etc.

and on electromagnetic parameters of the radar system used like incidence angle, polarization, frequency etc.

1.2.1. Introduction to InSAR

Synthetic Aperture Radar (SAR) is a side-looking active microwave system that produces high resolution images of the land surface or objects on it. SAR is a monostatic radar (single antenna to emit and receive microwaves) platform where both temporal (revisit time) and spatial resolution vary depending on the special characteristics of the satellite constellation. A very important trait of the SAR technique is that it is a coherent imaging system, meaning that the amplitude and the phases of the emitted pulses are preserved. This characteristic allows the implementation of interferometry (Engdahl et al. 2013).

InSAR (Interferometric Synthetic Aperture Radar) is a technique based on utilizing the phase differences between two or more SAR images. There are different forms of InSAR, depending on the acquisitions' temporal and/or spatial baseline and the parameters of the radar system used. This thesis will focus on two different but not mutually exclusive InSAR forms: repeat pass interferometry and differential interferometry, in order to use the phase difference information to estimate soil moisture changes and eventually land deformation. Repeat pass interferometry employs acquisitions taken at different times, allowing the study phenomena inducing land changes such as land subsidense, ice dynamics etc. Differential Interferometry is the technique where using a DEM, the contribution of the altitude is subtracted from the interferometric phase allowing the estimation of the terrain motion component (Ferretti et al. 2007).

1.3. Problem Statement and Objectives

The area of Delfland, south of Delft is such an area where peat soils are prevalent and land subsidence has been noted. In order to monitor and study the subsidence of this particular area, the method of InSAR, among others, has been implemented. However, the products of this method have been plagued with systematic errors, caused by the effects that both vegetation and the high organic content of the soil have on the SAR signal.

At this point, the possibility to take advantage of InSAR closure phases to estimate soil moisture changes, a novel method proposed by De Zan, Parizzi, et al. 2013, De Zan, Gomba, and Yokoya 2018 (Zan et al., 2014; De Zan and Gomba, 2018) and De Zan and Gomba 2018, and studied by Zwieback, Hensley, and Hajnsek 2015a; Zwieback, Hensley, and Hajnsek 2015b; Zwieback, Hensley, and Hajnsek 2017, comes into play. The study by De Zan, Parizzi, et al. 2013provide insight into using phase triplets, from SAR products, to obtain information regarding soil moisture changes. This method is quite promising since the benefits are twofold. First of all, it may be able to generate soil moisture data with fine spatial resolution (pixel size less than 1x1km). Second, soil moisture information can prove to be very useful for land deformation monitoring studies since changes in it induce significant noise in InSAR data. Knowing the soil moisture, would result in its quantification into phase correction De Zan and Gomba 2018 to insert into InSAR estimates.

1.3.1. Research question

To this date, a vast array of techniques has been developed to retrieve large scale soil moisture data, however closure phases remains a seldomly touched domain. This thesis research aims to contribute to current knowledge about the utility of InSAR closure phases as a means to derive soil moisture. According to literature, L-band closure phase data have shown potential in soil moisture retrieval over bare ((De Zan, Parizzi, et al. 2013))and vegetated ((De Zan and Gomba 2018)) areas, however no extensive research has been done so far using C-band data.

Hence, the scope can be summarised as:

- To determine whether soil moisture in vegetated areas can be accurately estimated using the method of phase closure inversion of C-band data
- Produce a time series of soil moisture data of the study area
- Test whether soil moisture is correlated to land deformation and model its contribution

1.4. Research Questions

The research question that arises during the problem statement is related to this thesis is formulated and presented as follows:

Is it possible to detect soil moisture changes with the method of closure phase inversion, using Sentinel-1 C-band data?

The main research question can be then split to sub questions:

1. Does the phase closure inversion method proposed by De Zan work in C-band?

   So far, the method proposed by De Zan has only been implemented using L-band Alos-2 data and the results so far have been quite promising. It is a priori known that due to a shorter wavelength C-band's penetration ability is weaker than L-band's, since the penetration capability of a microwave is inversely proportional to the frequency of the signal. C-band penetration depth has beenfound to be 1-2 cm, while L-band's is betwwen 5 and 8 cm (Owe and Van de Griend 1998). Consequently, the quality of C-band derived soil moisture is expected to be somewhat lower than that of L-band.

2. How does land cover affect the closure phase dataset?

   The texture of the soil plays a major role in the natural processes revolving around soil moisture and therefore it has to be taken into account by the employed method. However, on top of that, there is a wide range of objects on the surface obstructing the radar signal from reaching the soil. These objects can be different types of vegetation, ranging from bushland to forest, snow, permafrost etc. Moreover, there are also areas where man-made structures completely replaced soil and thus the drainage is artificial, ergo, it is of interest to observe how closure phases behave for different land cover types. There are methods which can be used to possibly filter out vegetation effects but they will not be investigated in this study.

3. Is the detected soil moisture spatially consistent with land cover?

   This comes up as a follow up to the previous question. Consistency is an important parameter in order to decide whether the results are arbitrary or can be trusted. Pixels belonging in the same land cover would ideally have similar coherence and closure phase history which would result in similar soil moisture trajectory.

4. Is it possible to use the produced soil moisture timeseries for interferometric phase corrections?

   The method employed for the estimation of soil moisture fluctuation can be reverse engineered to convert those time series into interferometric phase correction. We know for a fact that soil moisture changes induce noise/systematic error to InSAR phases, which is yet to be adressed and accounted for into modern models. Due to this, it would be interesting to test whether the proposed model can provide accurate phase corrections to be subsequently used to possibly correct land deformation measurements by filtering out this “noise displacement”

1.4.1. Thesis outline

This thesis consists of five chapters and an appendix. Chapter 2 covers most of the basics regarding the scientific and technical background of both soil moisture and Interferometry. This knowledge will be valuable to further comprehend the following chapters. Last, a brief introduction to the study areas will be given. In Chapter 3 the methodology of this research is meticulously presented. First, there is an overview of the data acquisition and preprocessing, followed by the description of the soil moisture estimation method that is implemented and the follow up “translation” of the produced timeseries into land deformation correction. In Chapter 4 the most important results of this research are presented and discussed. The rest of the results and the interferograms can be found in the Appendix. Finally, the soil moisture results produced will be evaluated and the possibility of them being used to enhance InSAR land deformation monitoring. In conclusion, Chapter 5 will present brief answers to the research questions introduced in chapter 1 and present some recommendations for further research. Finally, additionally produced figures will be included in the Appendix.

2

Background Information

This research has two main objectives, them being study whether soil moisture differences can be modelled from InSAR phase closure as well as whether those now modelled soil moisture differences can reduce the uncertainty in land deformation monitoring. The basic concepts of soil moisture and Interferometry will be explained in this chapter.

2.1. Soil Moisture

Soil moisture is an essential component of the earth system, notably but not exclusively in the water balance of a water catchment area. It has a key role in the feedback processes between land and atmosphere, hence the importance to estimate soil moisture storage in order to gain a better grasp of the processes involved. The fundamental equation for soil moisture modelling is the following:

$$\frac{dS}{dt} = P - ET - R \tag{2.1}$$

Which can be also presented in a more detailed fashion:

$$\frac{dS}{dt} = (P_r + M)\text{-}(E + T)\text{-}(R_o + R_s + R_g) \tag{2.2}$$

Where the change of soil moisture in time depends on the tradeoff between the moisture input from precipitation P_r and snowmelt M and the moisture loss through evapotranspiration (evaporation E and plant transpiration T) and runoff R. Runoff can be further partitioned in Hortonian overland flow R_o, subsurface lateral flow R_s and percolation to groundwater R_g. Furthermore, the soil moisture content of the root zone defines the availability of water to plants (Legates et al. 2010).

Soil moisture is the underlying factor in all three major subdivisions of physical geography: climatology, hydrology & geomorphology as well as biogeography. A deep understanding of its nature and variability helps to identify interactions between the three aforementioned branches.

2.1.1. Soil Moisture & Microwave Remote Sensing

During the past three decades, microwave remote sensing has been employed to detect surface soil moisture changes over bare and vegetated soils. This is possible due to the ability of microwave remote sensing to make estimations of the soil's dielectric properties based on land surface emissivity (Mohanty et al. 2017).

In microwave remote sensing soil moisture (SM) refers to the volumetric water content (VWC) θ of a soil and is defined as the volume of water V_w existing in a volume of soil V_s.

Volumetric water content is expressed as a ratio $[m^3/m^3]$ and its maximum value is equal to the soil's porosity.

$$\theta = V_w/V_s[m^3/m^3] \tag{2.3}$$

Typically, low frequency radars (X-, C- and L-band) have been used to estimate near-surface (0-5cm) soil moisture. This near-surface soil moisture should not be confused with root zone soil moisture which can not be detected using Microwaves due to their limited penetration capability. Over the years, multiple satellite platforms have been employed to acquire global soil moisture products, both passive and active. Both passive and active systems rely on either (semi-)empirical or physical models to describe the dielectric behavior of moist soils as a function of soil physical parameters at microwave frequencies (Hallikainen et al. 1985). Additional models are implemented for soil moisture estimation over vegetated areas such as the Water Cloud model, crop model and the f-k model (Zhang and Zhou 2016).

2.1.2. Climatology and atmospheric moisture

The energy balance is a mechanism where soil moisture serves as an integral cogwheel. It is responsible for the partitioning of energy at the land-atmosphere interface into latent (evaporation) and sensible (heating the air) heat (Duerinck 2014). The following equation presents the so-called energy balance:

$$R_n = H + \rho_w \lambda \mathrm{E} + G \tag{2.4}$$

Where R_n is the net radiation available at the surface of the Earth needed to heat the air H, evaporate water $\rho_w \lambda \mathrm{E}$ and heat the ground G.

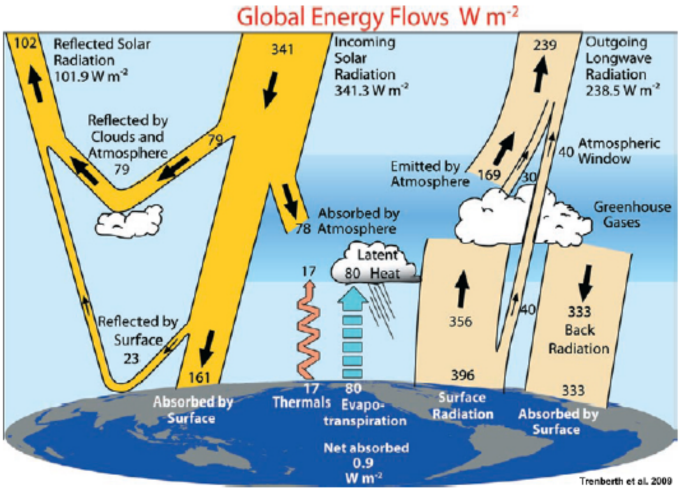

Figure 2.1: Global energy balance from (Physics of Evaporation) by (A.M.J. Coenders-Gerrits)

Comprehensive studies by (Ent et al. 2010) (Yoshimura et al. 2004) showed that a significant portion of the global precipitation originates from atmospheric moisture generated by terrestrial evaporation as illustrated by 2.2. This phenomenon is called moisture recycling. It was estimated that on average 40% of global precipitation is provided by continentally generated moisture, ranging from as low as 20% in Oceania to as high as 48% in Africa, while 57% of terrestrial evaporation returns to continents in the form of precipitation, with a high of 66% for Europe. The contribution of terrestrial evaporation varies both spatially and temporally and there are numerous reasons for that. Moreover, (van der Ent et al., 2010) provided a parameter called rainfall multiplier (m_c) indicating the amplification of precipation with a global average value of 1,67.

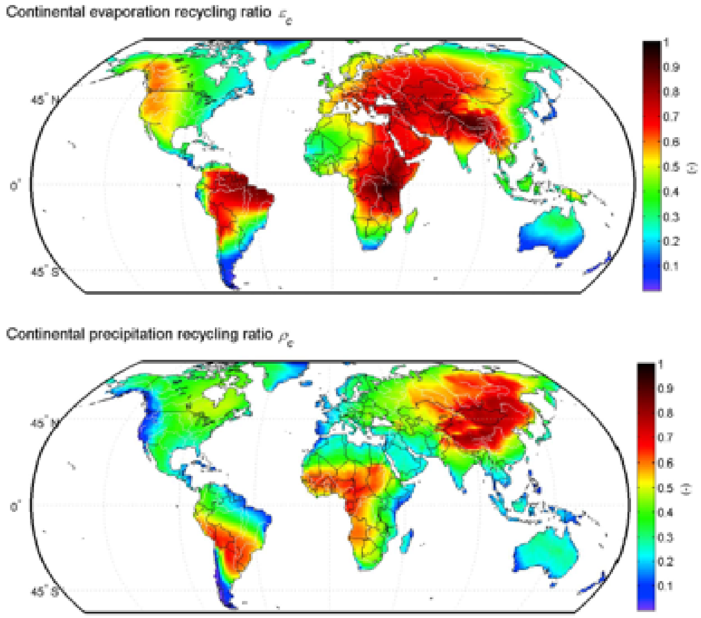

Figure 2.2: Average continental evaporation and precipitation recycling ratios

2.1.3. Hydrology

Hydrology is the science where the distribution and movement of water within the hydrologic cycle is studied. The soil and in particular the unsaturated zone lies at the interface between land surface and the first layer of the atmosphere, thus being key-variable acting as the partition controller of the input (precipitation) into three components (Brocca, Melone, and Moramarco 2005). The three partition paths are evapotranspiration, infiltration and surface runoff and their interaction with the soil water content of the unsaturated zone can be understood by studying the layout of a lumped conceptual hydrological model 2.3.

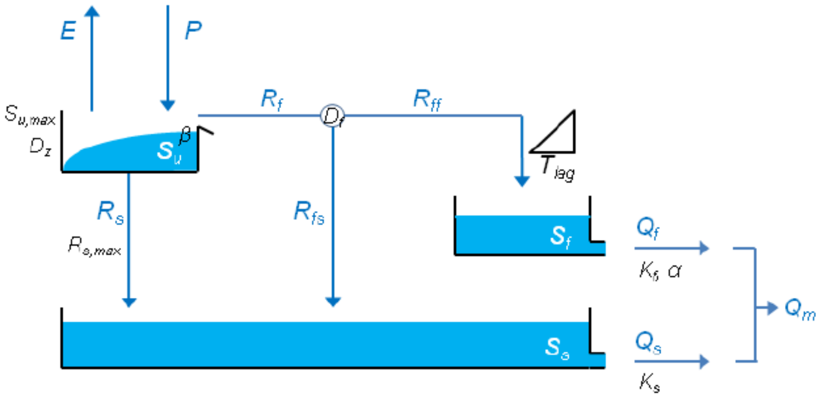

Figure 2.3: Layout of a lumped conceptual model. P is precipitation, E is evapotranspiration while S_u and $S_{u,max}$ are the current and the maximum storage respectively in the unsaturated zone. R_f is runoff and R_s is slow response (infiltration) (Aalbers 2015)

This model, called FLEX, which was developed by (Fenicia et al. 2006) acts as a simplified, abstract, yet not dumbed down, representation of a drainage basin (typical scale of a hydrological system). The water content of the unsaturated zone can be perceived as a reservoir which receives precipitation as input and then distributes (hydrological response) it to various parts of the system. The presence of the unsaturated zone storage at the majority of the governing equations of the FLEX model signify the importance of soil moisture on the early stage of the hydrological cycle.

$$E = E_p * min(1, \frac{S_u}{S_{u,max}} \frac{1}{L_p}) \tag{2.5}$$

where E_p is the potential evaporation and $L_p(-)$ the fraction of maximum storage below which evaporation is constrained by moisture. In similar fashion for infiltration R_f and fast runoff R_f respectively:

$$P_i = (1 - \rho) * P \tag{2.6}$$

$$R_f = \rho * P \tag{2.7}$$

Precipitation P fills (infiltrates) the reservoir over time, until a certain threshold is exceeded, which depends on its physical properties (soil texture etc.). Afterwards, the precipitation is partitioned into two parts, the first being infiltration and the latter being fast runoff. The runoff coefficient , which dictates the division into the aforementioned flows, depends on both soil moisture and saturation threshold.

$$R_S = \frac{S_u}{S_{u,max}} * R_{S,max} \tag{2.8}$$

The percolation rate to the underground is linearly constrained by the relative soil moisture content (Aalbers 2015).

2.1.4. Geomorphology & Biogeography

Geomorphology is another scientific study where soil moisture behavior is key knowledge to understand a wide spectrum of natural phenomena. Two main categories of such phenomena will be presented at this subchapter, hydrologic-aeolian erosion and mass wasting.

Soil erosion is a perpetual natural land process, which can be accelerated and enhanced by human-induced activities. This enhancement is by no means positive, as increased soil erosion leads to soil degradation, which has adverse effects on agriculture and environmental quality (Lal et al. 1994). This kind of degradation is especially apparent and hazardous in dryland areas. This environmental disaster only progresses geometrically, as increased soil degradation leads to aridity which further exacerbates the issue. There are two major factors affecting soil erosion, wind and soil water content, the latter's impact often being discounted. According to (Thomas and Middleton 1997) wind and water erosion contribute to 87% of the degraded land. On one hand, wind erosion is more dominant in arid climate. Among the reasons wind erosion is prevalent is the absence of soil moisture. Moisture has a direct effect on the bonding forces of soil particles. Those bonding forces are further increased by vegetation which actively protects soil from wind erosion (Ravi et al. 2010). This kind of erosion is deterred by the presence of biological soil crusts, often consisting of a mixture of fungi, algae and soil particles, as they increase soil stability.

On the other hand, water erosion prevails in humid climate. It is associated with processes related to the hydrologic cycle such as rainfall and runoff. The impact of the raindrops on the ground break the soil aggregates which are then dislodged due to the kinetic energy of the generated by rainfall. At the previous chapter, the effect of antecedent soil moisture on runoff generation was mentioned (Ravi et al. 2010). This antecedent soil moisture also indirectly affects the nutrient and sediment loss caused by overland flow (Legates et al. 2010).

Mass wasting or mass movement is a poll of natural processes where soil, rock etc will move downhill following the local relief. Common triggering mechanisms are earthquakes, overburden from structures and increased soil moisture. As it has been already mentioned, water surface's tension is essential to maintain soil cohesion. A simple example is building a sand castle, where water is needed to construct the walls and the towers, yet if the structure is flushed with water it will eventually collapse. Slope stability obeys to the same law of nature: a small amount of water is needed to maintain cohesion, yet too much of it will diminish friction effects and will lead to a landslide or soil creep (Lumen Physical geography 2017). Fieldwork studies have indicated, that the rapid increase of pore-water pressure is pivotal for the initiation of slope failure (Tohari, Nishigaki, and Komatsu 2007). Precipitation introduces infiltrating water which in turn dissipates the soil suction in the unsaturated zone, resulting in reduction of shear strength. (Ray, Jacobs, and Alba 2010) that a concurrent increase of unsaturated zone water content and a rising groundwater table increase the vulnerability of slope failure.

2.2. SAR Remote Sensing

A SAR is an active microwave imaging radar, mounted on a moving platform, which illuminates the surface with its own radiation, thus making the system independent of solar radiation. It has the ability to penetrate clouds, precipitation and depending on the microwave frequency used, it may also penetrate foliage, vegetation even ground. The backscattered signal is collected by the same radar antenna. As shown in 2.4 the satellite, on which the antenna is mounted, flies in azimuth direction, also called along track, the antenna is facing the Earth. The direction of the antenna's Line of sight (LOS) is called across track and since the system is side looking, the look angle forms an angle θ to the nadir direction (Engdahl et al. 2013).

Furthermore, the radiation emitted by the system is coherent, meaning that the frequency and waveform are always the same and the phase difference between two waves is always a constant. This is an essential characteristic of SAR as it allows the implementation of interferometry.

This thesis research mainly revolves around the exploitation of interferometry, a widely known and applied SAR technique, in order to obtain information regarding soil moisture. In addition to classic interferometry, a novel method developed by (De Zan, Parizzi, et al. 2013) involving phase triplets and coherence magnitude to quantitatively estimate soil moisture changes. This chapter will introduce and elaborate on these concepts.

2.2.1. SAR Principles

First of all, what does synthetic aperture mean? We know that the radars sensor is transmitting and receiving signal continuously in a strip mode. The received signal has a very low resolution due to the physical constraint of the antenna. However, this resolution is sharpened dramatically, by using multiple consecutive low-resolution images to reconstruct the backscattering making use of the system's degrees of freedom (redundancy). Consequently, a single image of a "synthetic aperture" is created via the method termed SAR focusing (R. F. Hanssen 2001). The focused SAR images are stored in a format known a single-look complex (SLC) data. In this format every pixel's value consists of a complex phasor P as

$$P = Re(P) + iIm(P) = Aexp(\iota\varphi) \tag{2.9}$$

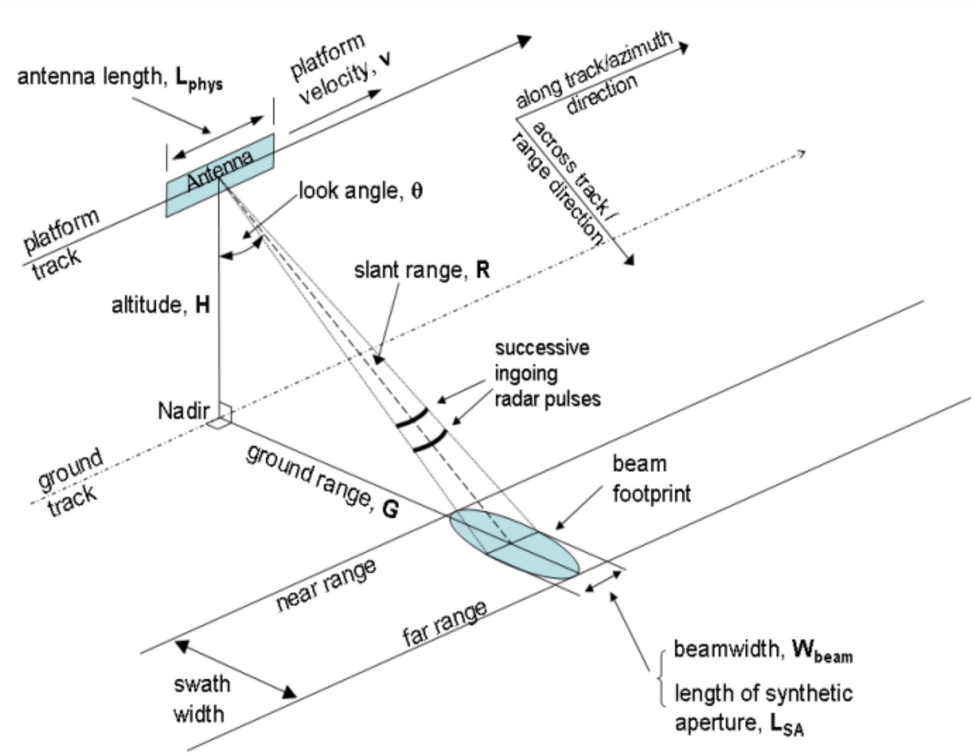

Figure 2.4: Imaging geometry of a side-looking SAR. (Engdahl et al. 2013)

$$\varphi = \frac{2\pi}{\lambda} 2r = \frac{4\pi}{\lambda} r \tag{2.10}$$

where $Re(P)$ and Im(P) are the real and imaginary parts of the complex phasor (Samiei Esfahany 2017), λ is the radar's operating wavelength , r denotes the slant range distance between the antenna and the surface objects projected onto the respective pixel. The phase φ of the SLC has a number of components as presented below:

$$\varphi = \varphi^{range} + \varphi^{atmo} + \varphi^{scat} + \varphi^{noise} \tag{2.11}$$

with φ^{range} referring to the range dependent phase, φ^{atmo} to the delay in phase caused by the atmospheric conditions, φ^{scat} to the phase related to the distribution of the scatterers and φ^{noise} to the phase induced by the radar's system noise. It should be noted here that the values of the phase are wrapped with the modulo-2 operator. $Re(P)$ and Im(P) are the real and imaginary parts of the complex phasor as (Samiei Esfahany 2017).

$$Re(P) = Acos(\varphi), \quad Im(P) = Asin(\varphi) \tag{2.12}$$

Which are derived from equation (2.11) and the implementation of Euler's formula:

$$exp(i\varphi) = cos(\varphi) + sin(\varphi) \tag{2.13}$$

2.2.2. Interferometric SAR (InSAR)

InSAR is a SAR technique widely applied in Geodesy and Remote Sensing, predominantly used to detect land movement and displacement. Its applications include among others the monitoring of volcanic deformation, land subsidence and glacial motion. SAR interferometry requires two coherent and coregistered images to measure the phase difference between them.

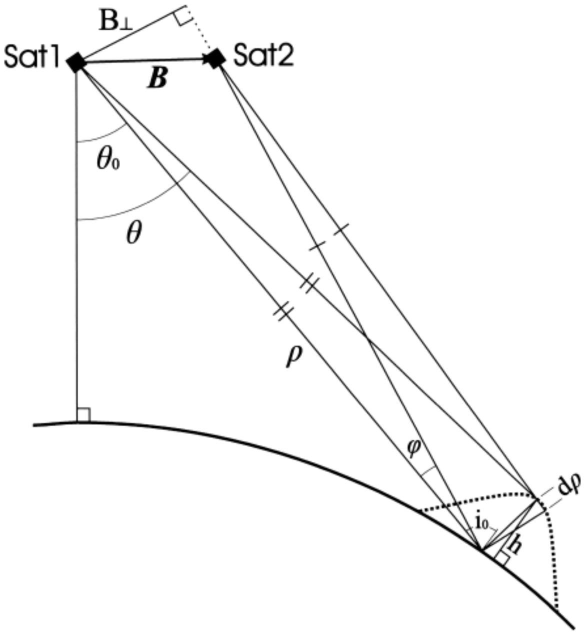

Figure 2.5: Geometrical configuration of repeat-pass SAR interferometry. Sat1 and Sat2 are the master and slave acquisitions respectively, while B is the baseline, θ_0 is the look or squint angle, i_0 is the incidence angle and ρ is the slant range . (Tobita et al. 1998)

By recording the same area from different squint angles, as shown in 2.5, the phase difference can be estimated and then translated to displacement following a procedure, where the stack of images used will first be resampled on a unique grid and its spectra will be appropriately processed (Goldstein filtering etc.) before calculating those phase differences. Normally, a difference would be calculated by subtracting one value from another. Since the SLC data are complex this procedure is done by performing a complex image multiplication, where the 'master' image is multiplied with complex conjugate of the 'slave' image as shown next (asterisk denoting the conjugate):

$$I = P_M.P_S^* = A_M A_S.exp\ (i\varphi_M - i\varphi_S)) \tag{2.14}$$

The I being the complex interferogram of the two images. The interferometric amplitude is the product of multiplying the respective amplitudes for master and slave while the interferometric phase is the residual of subtracting the respective phases. The interferometric phase consists of the same phase terms as a regular SAR image (refer to equation 2.10). The range related phase term of an interferogram φ^{range} can be split into the following components

$$\varphi^{range} = \varphi^{defo} + \varphi^{topo} + \varphi^{flat} \tag{2.15}$$

where φ^{flat} is the effect of the curvature of the reference ellipsoid (e.g. WGS84 for Sentinel) on the interferometric phase and the baseline of the interferometric pair, while φ^{topo} is the distortion caused by the surface height above the reference surface. The final phase component is φ^{defo} which represents the phase offset caused by a deformation of the surface, which took place between the master and slave acquisitions (Samiei Esfahany 2017).

In land deformation studies using InSAR, the objective is to get rid of the rest of the components of the interferometric phase and determine an accurate value for the land deformation induced phase. This component can be then used to determine the actual deformation using the following equation:

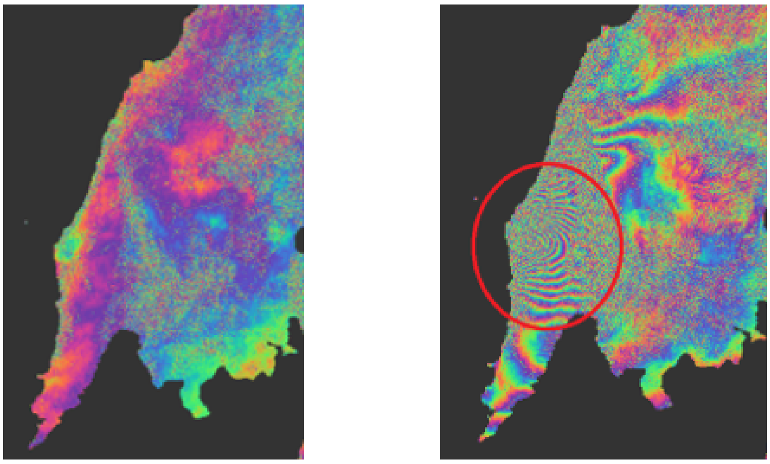

Figure 2.6: Interferometric phase maps of the isle of Leykada, Greece before (left) and after (right) the 2015's earthquake. The earthquake induced deformation phase is clearly visible as several concentric fringes forming around the epicentre. A deformation of 28,5cm was estimated using InSAR data (own work).

$$\varphi^{defo} = \frac{-4\pi}{\lambda} D_{LOS} \tag{2.16}$$

where D_{LOS} is the projection of the 3D displacement along the radar's Line of Sight (LOS) direction. Since SAR uses side looking radar, this displacement can be projected on the 3D space:

$$D_{LOS} = D_U cos(\theta_{inc}) - sin(\theta_{inc})[D_N cos(a_h - \frac{3\pi}{2}) + D_E sin(a_h - \frac{3\pi}{2})] \tag{2.17}$$

where D_U, D_N, D_E, are the components in Upward, North and East direction respectively, whereas a_h is the satellite's heading angle. However, in order to extract direction-oriented deformation extra information is needed. This is done by combining ascending and descending interferograms to recover the two vector of a 3D displacement. The last one requires assumption on the characteristics of the displacement (R. F. Hanssen 2001).

2.2.3. Decorrellation in InSAR

Decorrelation is among the main limitations of InSAR, hence the need to elaborate on the decorrelation mechanism as well as on its implication on this thesis. Among the components of phase one can find the φ^{scat}, which is the interferometric scattering phase, which is induced by the difference in scattering phase between master and slave acquisitions.

$$\varphi^{scat} = \varphi_M^{scat} + \varphi_S^{scat} \tag{2.18}$$

This scattering phase is a function of different components, such as the location of elementary scatterers within a resolution cell relative to the radar sensor and the electrical traits of the scatterers. Usually, decorrelation can be partitioned in 4 prevailing mechanisms (Samiei Esfahany 2017):

1. Baseline decorrelation: It is a fact that in master and slave acquisitions the radar antennas always have a slightly different position and therefore different incidence angle. In this case, not only the angle but also the range distance differs and hence the scattering phase will vary from acquisition to acquisition. The relative position of two acquisitions is

called baseline and this component is called baseline decorrelation as it increases together with an increase in the baseline. Spectral filtering is employed to overcome baseline decorrelation.

2. Doppler centroid decorrelation: This decorrelation component stems also from an angle difference, the squint angle (look angle θ in 2.4) which is the angle formed between the nadir line and the pointing direction of the antenna. This difference of the viewing direction in azimuth introduces the doppler centroid decorrelation. This kind of decorrelation operates in a similar way to the baseline one and is also mitigated with spectral filtering. Since these first two components can be successfully countered with existing methods and are somewhat irrelevant to this thesis there is no point of further elaborating.

3. Volume decorrelation: Although, the two abovementioned mechanisms are associated with $2D$ scattering, since reality is $3D$, there is also decorrelation caused by disturbance in the 3^{rd} dimension. This is caused by potential displacement of the scatterers in height which induces different imaging geometry. Volume displacement is common in vegetated areas (forests, crops etc.), where plant growth results in unpredictable random volume scattering. At this point, the operational wavelength of the radar comes into play, as its capability to penetrate into a volume of scatterers is directly related to it, with long wavelengths having greater penetration capability than shorter ones. Radar systems with large wavelengths (L-band) have decreased volume decorrelation compared to smaller wavelengths (C-band).

4. Temporal decorrelation: Last but not least, temporal decorrelation is caused by changes in the physical properties of the imaged objects between acquisitions (Morishita and R. Hanssen 2014). Such changes are caused by both human (soil plowing, cultivation) and non-human (snow fall, plant growth, natural phenomena) related drivers. In general, urban areas and the built environment are on the low end of temporal decorrelation as changes are scarce, while rural areas are more prone to changes which will result in high temporal decorrelation. Soil moisture is one the phenomena responsible for temporal decorelation, as it affects the dielectric properties of the soil and hence the backscatter.

A common way to quantify correlation between two images is the magnitude of the complex correlation coefficient or coherence, called absolute coherence ($|\gamma|$). The complex coherence is defined as:

$$\gamma = \frac{E\{y_1 y_2^*\}}{\sqrt{E\{|y_1^2|\}E\{|y_2^2|\}}} \tag{2.19}$$

Estimating the rate of temporal decorrellation over a dataset with given repeat interval is key to assess the possibility of retrieving coherent information. To achieve this, (Morishita and R. Hanssen 2014) presented the following method. Starting on:

$$\gamma(t) = \gamma_0 e^{-t/\tau} \tag{2.20}$$

where $\gamma(t)$ is the coherence observed at different t, γ_0 is the initial coherence and τ is the decorrellation rate which in turn is the time it takes for coherence to drop to $1/e$ of its initial value. Since zero coherence can not be observed due to bias in the coherence estimator and persistent dominant scatterers within the multilooking window the previous equation is transformed to:

$$\gamma\hat{o}(t) = (\gamma_0 - \gamma_\infty)e^{-t/\tau} + \gamma_\infty \tag{2.21}$$

where γ_∞ symbolizes the minimum attainable coherence. At this point the decorrellation rate τ stands for the time it take for coherence to drop to γ_∞ (Morishita and R. Hanssen 2014).

The total coherence can be broken down in different multiplicative coherence terms (Samiei Esfahany 2017):

$$\gamma_{total} = \gamma_B \gamma_{dc} \gamma_{vol} \gamma_{temp} \gamma_{thermal} \gamma_{procc} \tag{2.22}$$

Where γ_B is the coherence term related to baseline decorrelation, γ_{dc} related to doppler centroid decorrelation, γ_{vol} related to volume decorrelation, γ_{temp} related to temporal decorrelation and the final two terms are related to thermal and processing induced noise. The following equation expresses temporal decorrelation in terms of wavelength λ and variance of the motion of the scatterers σ_r (Morishita and R. Hanssen 2014):

$$\gamma_{temp} = exp(-\frac{1}{2}(\frac{4\pi}{\lambda})^2 \sigma_r^2) \tag{2.23}$$

It becomes obvious when looking at the equation, that longer wavelengths result in reduced temporal decorrelation, however the variance of the scatterers is equally important. This variance can be improved by increasing the temporal resolution of the timeseries which can only achieved by shorter repeat intervals.

2.2.4. Closure phase & ensuing ambiguities

The concept of interferometry is not strictly confined in SAR. Instead it is applied in other scientific fields like astronomy and oceanography. The concept of closure phase was first applied in astronomy to increase phase stability in VLBI (Very Long Baseline Interferometry) by Jennison in 1958. Closure phase is the sum of three phases resulting from a closed triangle, where the three points are positions of telescopes and the sides are the three baselines. This sum is independent of telescope-specific phase shifts induced by the atmosphere or the telescope system (Monnier, Perrin, and Malbet 2003).

Despite the widespread application of closure phases in astronomical VLBI technique, with its most prominent implementation being the imaging of a black hole (Event Horizon Telescope 2019), using closure phases in InSAR is a fairly novel technique, first introduced in 2013 (De Zan, Parizzi, et al. 2013). Currently, since research into closure phase for InSAR purposes is still at an early stage, contribution has been limited to that of De Zan, Zwieback and their respective research teams.

A statistic term used in astronomic interferometry to derive the insensitivity of closure phase is the bispectrum. Now, assuming a set of three SAR acquisitions, there are three possible interferograms $I_{mn}, I_{no} \& I_{mo}$. (Zwieback, Hensley, and Hajnsek 2015a) proposed to adapt bispectrum to InSAR's bicoherence Γ_{mno} which is defined as the triple product of the complex coherences $(\gamma_{mn}, \gamma_{no}, \gamma_{mo})$the three interferograms, with $*$ symbolizing the complex conjugate.

$$\Gamma_{mno} = \gamma_{mn} \cdot \gamma_{no} \cdot \gamma_{mo}^* \tag{2.24}$$

$$\Xi_{mno} = \varphi_{mn} + \varphi_{no} + \varphi_{mo} \tag{2.25}$$

The argument of which is the closure phase Ξ_{mno}. One would expect the phase closure to sum up to zero since each one of the phase components for range φ^r, atmosphere φ^{at}, scattering φ^{sc} and noise φ^n , will appear twice but with opposite sign.

$$\varphi_{mn} = (\varphi_n^r - \varphi_m^r) + (\varphi_n^{at} - \varphi_m^{at}) + (\varphi_n^{sc} - \varphi_m^{sc}) + (\varphi_n^n - \varphi_m^n) \tag{2.26}$$

$$\varphi_{no} = (\varphi_o^r - \varphi_n^r) + (\varphi_o^{at} - \varphi_n^{at}) + (\varphi_o^{sc} - \varphi_n^{sc}) + (\varphi_o^n - \varphi_n^n) \tag{2.27}$$

$$\varphi_{mo} = (\varphi_o^r - \varphi_m^r) + (\varphi_o^{at} - \varphi_m^{at}) + (\varphi_o^{sc} - \varphi_m^{sc}) + (\varphi_o^n - \varphi_m^n) \tag{2.28}$$

It would be expected that the sum of the three phases would sum up to zero, since the closure phase is invariant to topographic or atmospheric effects, as well as piston-like deformations (De Zan, Zonno, and López-Dekker 2015). Piston-like deformation describes a phenomenon where the subject moves uniformly within the time period. This means that the displacement between the SLC_m and SLC_o should equal the respective displacements between SLC_m and SLC_n plus that between SLC_n and SLC_o (Zwieback, X. Liu, et al. 2016).

This lack of consistency indicates the presence of additional underlying phenomena, which have to be taken into account. First of all, this inconsistency can be due to noise produced by decorrelation, mostly temporal and volume. Especially stacks of SAR images with significant temporal resolution decorrelation is a major obstacle in the analysis of phase closures, since a certain level of coherence is mandatory to have consistent signal. Temporal decorrelation depends on both the terrain and the satellite configuration (wavelength and repeat interval). In general, short repeat interval are necessary. Moreover, longer wavelengths (L-band) have an advantage over shorter ones (C-band) regarding decorrelation rate (Morishita and R. Hanssen 2014). There appears to be a critical range between 0.15 and 0.20 which defines whether an interferogram can be used. When coherence is below 0.15 no phase information can be extracted; 0.15 to 0.20 is an area where information can be obtained depending on the area type and above 0.20, phase information can be successfully retrieved (Wei and Sandwell 2010).

Nevertheless, decorrelation is of major importance for retrieval of phase information and consequently equally importance for phase triplets. Therefore, an issue emerging from the attempts at utilising the closure phase signal in InSAR, is identifying and separating the different mechanisms responsible for the measured closure errors, which is crucial for its correct interpretation.

It is important to examine whether the closure phase timeseries can be attributed either to noise alone or to other sources which will be mentioned next. According to the findings of a statistical test on the significance of these non-random effects on Ku- and X-band datasets (Zwieback, X. Liu, et al. 2016), the significance of the observed phase triplets varies seasonally and depends on both land type and coherence magnitude. The seasonality is linked to the precipitation pattern which in turn is reflected on soil moisture variation and snow melt detetcion, meaning that those phenomena can be detected via an analysis of the closure phases. However, often the sheer magnitude of the decorrelation noise ”breaks” the closure phases and puts wrench in the works of identifying and quantifying the underlying mechanisms.

A couple of such mechanisms inducing phase inconsistencies have been identified so far will be briefly presented (De Zan, Zonno, and López-Dekker 2015):

- Volume scattering: scattering produced when radiation moves from one medium to another, due to different permittivities (Elements such as leaves, branches, crowns of trees, rainfall etc.). The volume scattering phase inconsistencies occur due to vegetation growth (altering scattering profile) or baseline differences (altering incidence angle)

- Volume scattering occurring due to baseline variation. Typical in crossing-orbit interferometry. The ver tical scattering profile's skewness is directly linked with phase closures (Equation 2.26)

- Soil moisture variations: Multiple studies have shown that interferometric and closure phase contain information regarding soil moisture (De Zan, Parizzi, et al. 2013)(Morrison et al. 2011). This stems from the fact that the wavenumbers in soil are moisture dependent and thus a moisture difference between acquisitions will result in a phase difference. Experiments over bare soils (absence of vegetation induced volume scattering) indicate that the phase excess is possibly explained by soil moisture discrepancies.

- Vegetation water content variations: In some obsrvations over forested areas, the resulting phase inconsistencies cannot be explained solely by volumetric scattering effects. A hypothesis was made, where differences in vegetation water content explain the phase offset. This hypothesis is supported by (Albinet et al. 2012) using TropiScat P-band data and as for recently, also by (De Zan and Gomba 2018) using ALOS-2 L-band data.

A novel method, to actually exploit the loss of consistency due to underlying mechanisms, was developed by (De Zan, Parizzi, et al. 2013), when researchers noticed that in the case of multilooked interferograms the sum of the triple phase difference will not be zero, indicating a correlation of closure phase with soil moisture. This observation was backed up by the findings of (Zwieback, Hensley, and Hajnsek 2015b) where a linear dependence of closure phase with soil moisture change was observed.

The magnitude of the closure phase shows a reverse proportionality with coherences, as it tends to decrease when coherence increases and vice-versa (Zwieback, X. Liu, et al. 2016). Therefore, as a rule of thumb, one would expect higher closure phases when a drop in coherence is observed.

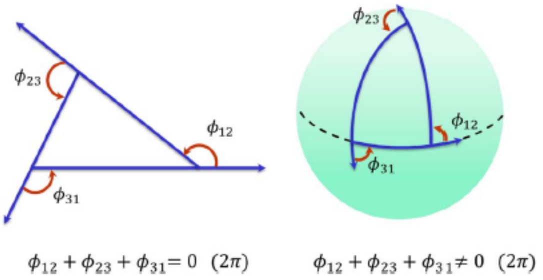

Figure 2.7: Examples of consistency on a flat plane (left) and inconsistency on a non-flat one (right) (De Zan, Zonno, and López-Dekker 2015)

A parallel to this finding regarding the inconsistency of a phase triplet can be drawn by looking at the inconsistency of the angles on a curved geometry. In Eucliden geometry (flat plane), the sum of the angles measured along a closed path should always equal zero (consistency). However, this does not hold in non-flat geometries, where the same closed path would result in a non-zero angle total (inconsistency).

In InSAR the inconsistency due to the effect of underlying mechanisms manifests as closure phase. In Geodesy, the inconsistency due to the effect of Earth's curvature manifests as spherical excess; the sum of the interior angles exceeds 180^o.

The main obstacle of using phase triplets to obtain soil moisture information is the ensuing ambiguity (Zwieback, Hensley, and Hajnsek 2017). Ambiguities are inherent to closure phase and refer to the fact that a single closure phase value Ξ_{mno} may correspond to multiple soil moisture time series. These time series can either have a systematic offset or opposite sign step changes as shown in 2.8.

Phase is antisymmetric with respect to permutations, since phase can take values from $-\pi$ to π, meaning that assuming acquisitions i, j the following relation between the possible interferometric values occur:

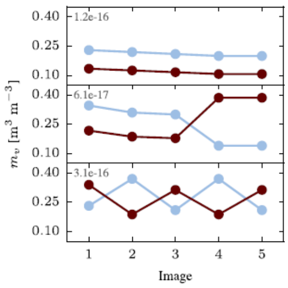

Figure 2.8: Different soil moisture (bare soil case) time series yielding similar closure phase, indicating the issue of ambiguity (Zwieback, Hensley, and Hajnsek 2017)

$$\varphi_{i,j} = -\varphi_{j,i} \tag{2.29}$$

This relation passes on to phase triplets, where triplets are antisymmetric to odd permutations and symmetric to even ones (Zwieback, Hensley, and Hajnsek 2017). An example of it is presented next, where Ξ stands for phase triplet:

$$\Xi_{mno} = -\Xi_{nmo} = \Xi_{omn} \tag{2.30}$$

This symmetry extends to any anumber of acquisitions and possible phase triplets and is responsible for the absence of sensitivity at detecting step changes andd sawtooth patterns. Moreover, this permutational symmetry propagates to any number of acquisitions and potential phase triplets.

The ambiguity of soil moisture can be solved by either using external data (ground truthing) or by using other SAR parameters, like coherence. A method to overcome the obstacle of ambiguities, was proposed and implemented by (De Zan and Gomba 2018),(De Zan, Gomba, and Yokoya 2018) based on the premise of symmetry or cyclical permutation, is part of the methodology and as such will be presented in Chapter 3 of this study.

2.3. Study Areas

The research of this thesis focuses on two distinct areas in Mexico and the Netherlands. The availability of Sentinel-1 closure phase maps over Mexico (De Zan, Gomba, and Yokoya n.d.); alas in a very crude form (no legend) meant that there was data available for a first qualitative analysis of my own generated closure phase maps. Moreover, this part of Mexico, like the Netherlands, also suffers from land subsidence. Thus, this particular area in Mexico was selected as the second study area.

2.3.1. Mexico

The study area in Mexico covers parts of two Mexican states: the Free and Sovereign states of Tlaxcala and Puebla. The area covered by the SAR dataset is 2226 km^2. It is located at the East-Central Mexico, between the capital, Mexico City and the largest port on Mexico's east coast, Veracruz. Different land cover types can be found at the study area as presented in Figure 2.9 (b) with the major ones being cropland, forest and urban. There are also shrublands (brown color) as well as patches of bare soil situated on the mountain tops of the national park.

The study area (Figure 2.9 (a)) covers a major part of the Valley of Puebla or Valley of Cuetlaxcoapan which is surrounded by the mountains and volcanoes of the Trans-Mexican volcanic belt (TMVB). At the southeast corner of the study area lies part of the National Park of Iztaccihuatl-Popocatepetl named after the 3rd and 2nd highest volcanoes in Mexico, Iztaccihuatl and Popocatepetl with an altitude of 5286 and 5426 m respectively. At the mid-east lies

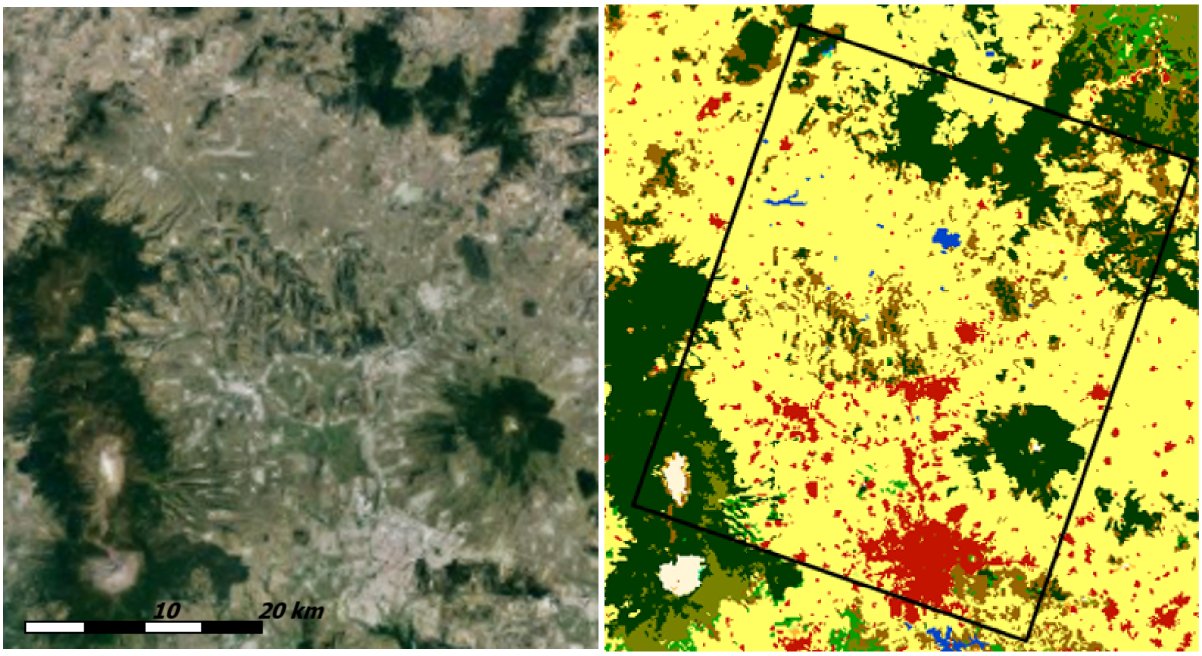

(a) (b)

Figure 2.9: The study area as seen from Google Earth (a) and its land types as detected by ESA. Red is urban, Yellow is cropland, White is bare soil and Green is forest (ESA CCI Land Cover).

La Malinche a dormant volcano (5th highest in Mexico) with an elevation of 4461m while the northern part is dominated by rugged terrain covered with forest, shrubs and cropland. The valley is covered by either croplands or urbanized areas. Major cities are the city of Puebla at the South, Tlaxcala at the middle of the study area and Apizaco north of Tlaxcala, while smaller towns can be found scattered all around the valley.

The Trans-Mexican volcanic belt (Figure 2.10 is a 1000km volcanic arc related to the subduction of the Cocos an Riveras plate beneath the North American plate. The Valley of Puebla is volcanic center of the TMVB, shaped during the Pliocene-Quaternary age (Gómez-Tuena et al. 2003). Due to the active volcanoes surrounding the valley, the soil consists of coarse volcanic ash and pumice rocks (42%) combined with finer loam and clay soils (Urbina-Flores et al. 2016),(Segura-Castruita 2006). These soils are called residual moisture soils (RMS) and have greater water retantion capacity than sandy soils, mainly dueto the pumice rock component.

The climate of the Valley is classfied as Cwb in the Köppen-Geiger classification system (Kottek et al. 2006). Cwb refers to Oceanic: Subtropical Highland climate, which exists in elevated areas (average valeey elevation is 2200m) within either the tropics or the subtropics. The climate is temperate at the Valley and cold at the surrounding elevated regions. Precipitation occurs mainly during the rain season lasting from May to October with a yearly average of 827mm with a dry season from November through April. Figure 2.11 presents average precipitation and temperature data for the study area.

2.3.2. Netherlands

The study area covers a large part of the municipality of Zuid Holland and the eastern part of the municipality of Utrecht. The area covered by the SAR dataset is 720 km^2. It is situated in the west of the Netherlands, on the North Sea. The terrain is mostly flat and the majority of the area is below sea level as presented in Figure 2.12(a).

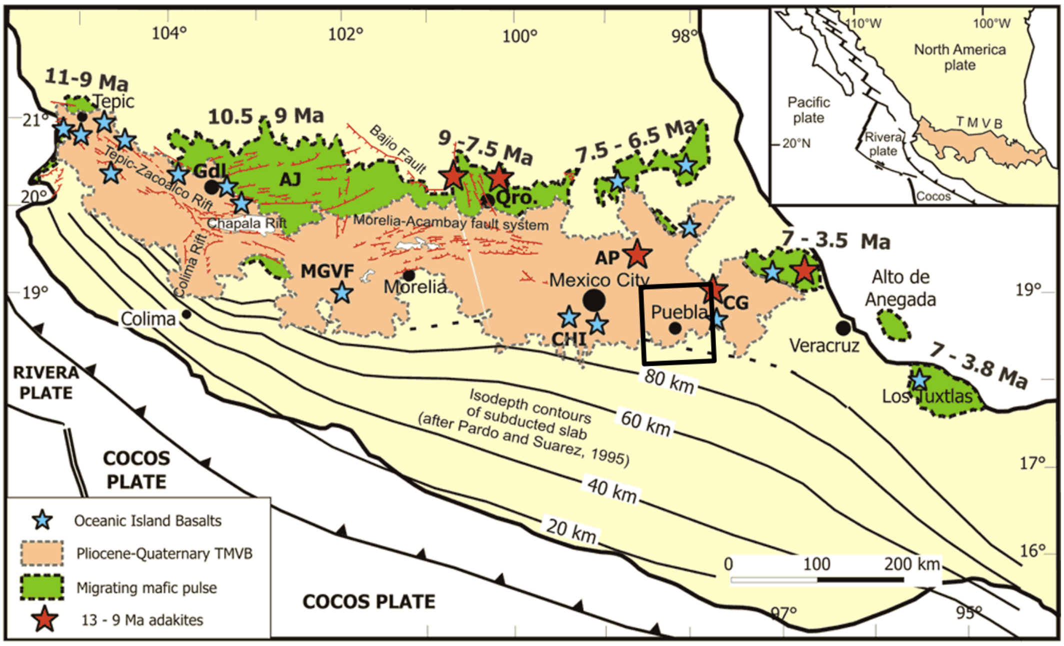

Figure 2.10: The Trans-Mexican volcanic belt and the location of the study area (Ferrari 2003)

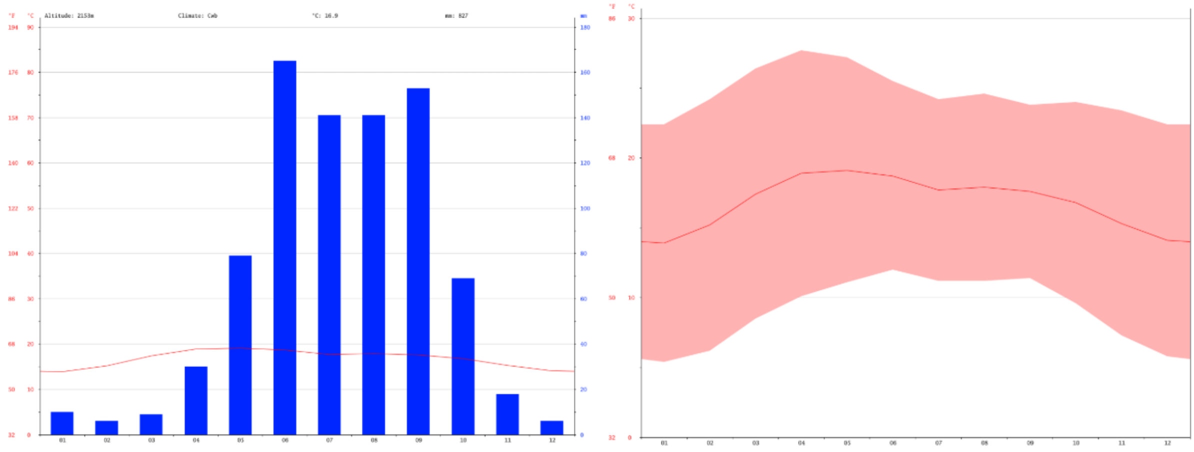

(a)

(b)

Figure 2.11: Average monthly Precipitation (a) and Temperature (b) at the Valley of Puebla (climate-data.org n.d.)

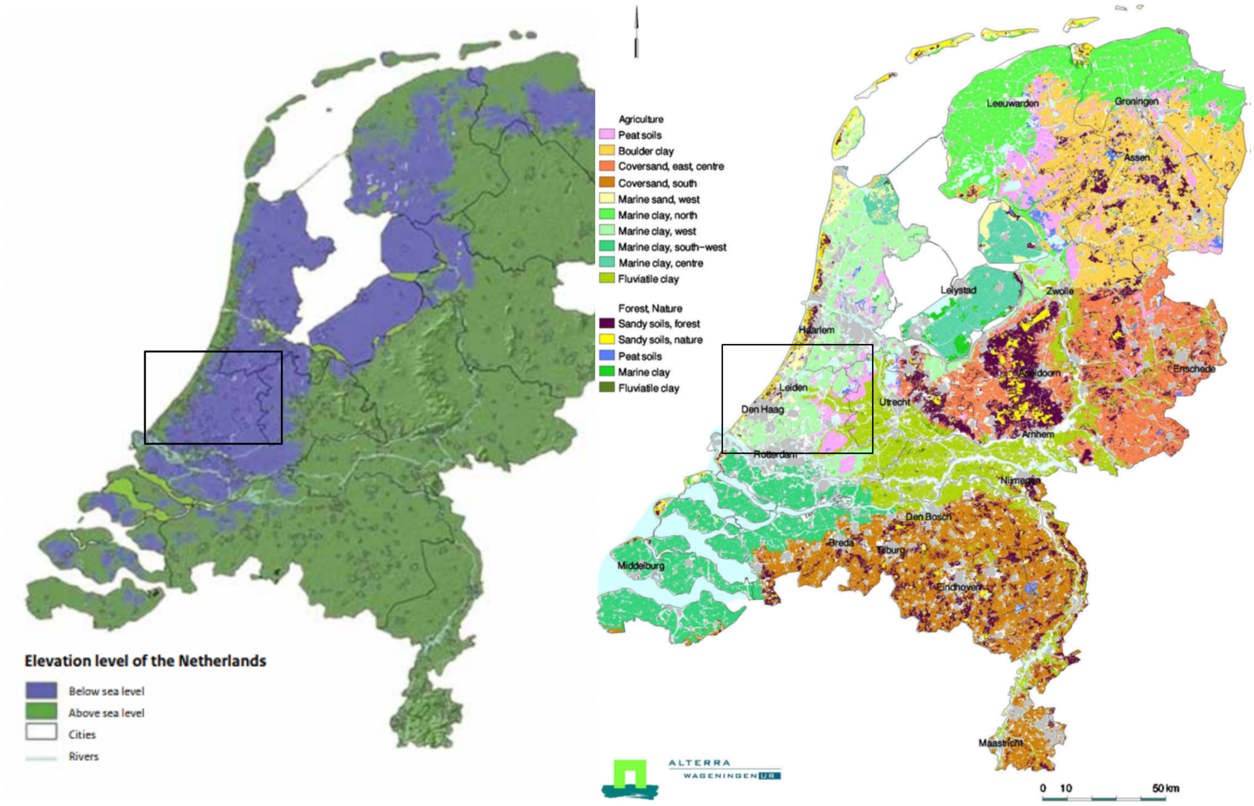

(a) (b)

Figure 2.12: Above and below sea level (a) (Actueel Hoogtebestand Nederland n.d.) and soil types in the Netherlands (b) (Brus, Lame, and Nieuwenhuis 2009).

Land cover data are presented in Figure 2.13. The majority of the area is classified as cropland, which includes different types of crops and grassland. Urban areas cover a significant part of the studied area with major municipalities such as The Hague, Rotterdam, Leiden, Delft and Utrecht. Forested areas can be found all over the map and usually around urban areas. Lastly, herbaceous vegetation exists primarily along the coastline (coinciding with the location of sand dunes for water defense) and thinly spread around the map.

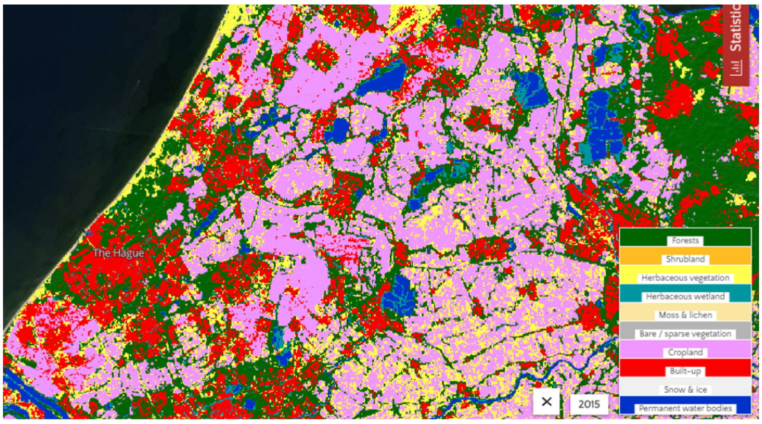

Figure 2.13: Land cover types located at the study area (Copernicus-Land Monitoring Service 2015)

The soil of this region is dominated by the presence of clay and peat (Figure 2.12)(b), while the shoreline is rich in sandy soils (Brus, Lame, and Nieuwenhuis 2009). The substrate of the study area consists of early Holocene deposits alluvial and lagoonal peat and clay sequences, which are called the the Naaldwijk and Nieuwkoop formations (Marc Hijma 2017). The Naaldwijk formation is characterized by variations of sand and clay while the Niewkoop primarily consists of clay and secondarily of clay deposits. The DINOloket database, a collaboration between TNO's and the Geological Survey of the Netherlands, consists of a dense network of boreholes providing among others useful information regarding the soil profile and texture of the area of interest (DINOloket n.d.). The borehole profiles show that both aforementioned formations may appear on the top soil with an example shown in Figure 2.14

The Netherlands is a small and flat country and climatological differences are therefore small. The climate of the Netherlands can be classified as Cfb in the Köppen-Geiger classification system (Kottek et al. 2006). Cfb refers to Oceanic: Marine West coast climate. The climate is influenced by the North Sea and the Atlantic Ocean, with moderate winters and cool summers. Precipitation is distributed throughout the year, with a slightly dryer period from February to June with a yearly average of 800mm. Figure 2.15 presents average precipitation and temperature data for the study area.

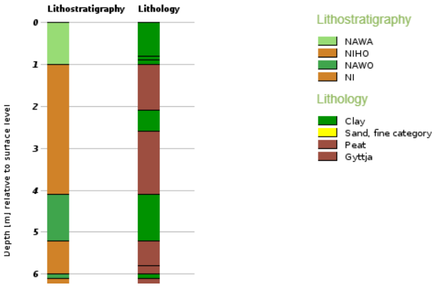

Figure 2.14: Example of a borehole log profile (DINOloket n.d.)

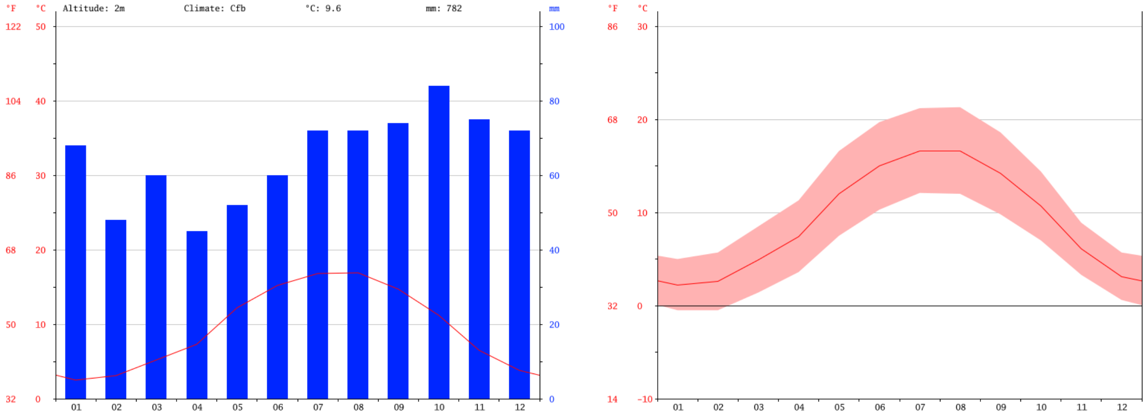

(a) (b)

Figure 2.15: Average monthly Precipitation (a) and Temperature (b) in the area of interest (climate-data.org n.d.)

3

Methodology

The goal of this study is to investigate the potential of soil moisture retrieval using Sentinel-1 C-band plase triplets. Thus, SAR data were collected and used to carry through with the research. The methodology can be broken down in 5 discrete steps, which will be presented in this chapter.

3.1. Data acquisition & pre-processing

At this point the criteria regarding the selection of the satellite products used will be explained, followed by a brief description of the pre-processing steps leading to the interferogram creation. The steps and the logic behind them are going to be explained without giving in to either describing how the software works or its respective commands. To keep things simple and avoid repetition, from this point on all processing steps are done using SNAP unless it is stated otherwise. These steps are listed below:

- Split and apply orbit
- Coregistration of master-slave images
- Create interferogram and eliminate redundant lines with deburst
- Removal of the topographic component of the phase

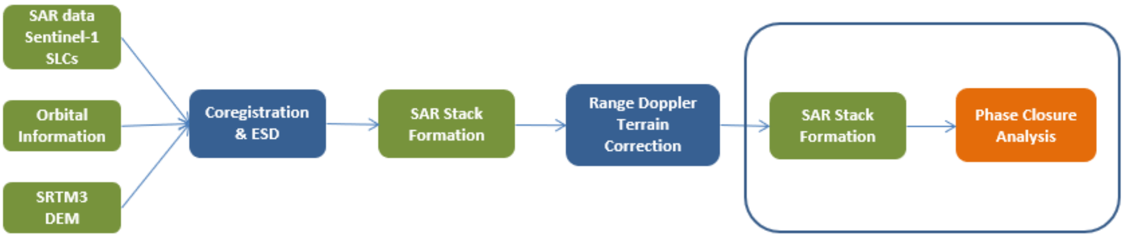

Figure 3.1: This chart shows the sequence of the processes leading up to the analysis of the phase closures. The circled part is presented in chapter 3.2 but is included for the sake of presenting the whole picture.

,

3.1.1. Data used

In general, there are a lot of different satellite constellations and products which can be used to perform deformation analysis using InSAR. Such could be C-band Radar satellite 2 (Rsat-2), C-band Sentinel-1 (S1), L-band PALSAR-2 ALOS2 products etc. For this study, Sentinel-1 data will be used and the major reason behind this decision lies in the fact that, during the early stages of this thesis, it was decided to use SNAP for the pre-processing of the SLCs up to the creation of the interferograms. A known disadvantage of choosing C-band over L-band is that the expected coherence is lower, which will result in smaller closure phases (De Zan and Gomba 2018). Also, the temporal sampling of Sentinel-1 (12 days) is likely insufficient for soil moisture measurements, taking into account the expected temporal decorrelation. Despite the drawbacks mentioned above, Sentinel-1 mission's major advantage is that it provides temporally consistent, worldwide coverage, freely accessible to anyone interested.

SNAP is a software developed by ESA encompassing all of Sentinel toolboxes in order to do earth observation processing and analysis. Another reason behind the selection of Sentinel-1 data is that ESA through the RUS service, provides an on-line free-access platform to promote the uptake of Copernicus data and support the scaling up of R&D activities. This is very useful since although InSAR processing requires high end hardware which is not easily accessible, it can be easily overcome, employing a virtual machine provided by the Copernicus mission.

For this study Level-1 Single Look Complex (SLC) IW products will be used. The Interferometric Wide (IW) swath mode is the main acquisition mode over land and satisfies the majority of service requirements. It acquires data with a 250 km swath at 5 m by 20 m spatial resolution (single look). IW mode captures three sub-swaths using Terrain Observation with Progressive Scans SAR (TOPSAR) [1]. IW SLC products contain one image per sub-swath and one per polarization channel, for a total of three (single polarization) or six (dual polarization) images in an IW product. The IW mode has 2,7x22m resolution and 2,3x14,1m pixel spacing.

Since, there are two areas of interest, at least two datasets had to be collected. Regarding the Netherlands, a total of 29 SLCs were used in this study, covering a period starting from February 9th 2017 to January 24th 2018. The study area of Mexico was considerably bigger and due to constraints in computing power, had to be split in two different subsets. Both subsets used the same Sentinel-1 acquisitions from December 12th 2014 to November 15th 2015. Considering the goal was to study the possible interactions between soil moisture fluctuation and land subsidence, a period of a year was deemed necessary to have adequate data to study the phenomenon.

3.1.2. Orbital information

First of all, the accuracy of interferometry depends heavily on information regarding the relative position of the satellites during the time the 2 paired images were taken. Consequently, uncertainties in the available orbit information may distort the imaging geometry, the data geocoding, as the geographic coordinates of each scatterer depends on the geometry of the acquisition) (Engen and Johnsen 2010), as well as the resulting phase differences and thus precise orbital data are crucial in InSAR data processing. Orbital products for the Sentinel missions are provided by Copernicus Precise Orbit Determination (CPOD) service for Near Real-Time (NRT) etc., while the accuracy is assessed by external validation authorities (Fernández et al. 2015). Those orbit files are fetched and applied on the SLCs to improve the results of the following step: coregistration.

3.1.3. Coregistration & ESD

The particularity of this method lies to the fact that instead of using pairs of SLCs as usual, instead triplets are used. Each dataset needs to be coregistered, meaning that identical scatterers need to be identified and combined, which becomes possible once the grid of both images is aligned to each other. In order to do so, one SLC will act as the "master" image while the rest become the "slaves", the pixels of which have to be aligned with pixels of the former. In the given case, the first SLC in terms of temporal acquisition will be designated as the "master" image.

For InSAR applications, the sub-pixel registration of the focused SAR images is a strict requirement for interferometric processing, especially for terrain observation with progressive scan (TOPS) mode applied on Sentinel-1 satellite. SNAP employs DEM-based coregistration, where the offsets are computed based on the orbit information provided in the previous step and by the DEM (Samiei Esfahany 2017). This procedure is precisely described in (Sansosti et al. 2006) consequently, delving into details will be a redundancy. The aforementioned DEM is provided by NASA's Shuttle Radar topography Mission 3 arc-sec (SRTM3), with a resolution of 3 arc-sec which translates to 90m on the ground. The DEM resampling method as well as the resampling method was selected to be bilinear-interpolation. This method is preferred to conventional polynomial approximations, especially in case of rough topography or long baselines (Nitti et al. 2010), the latter being the main driver for this choice of operator. Coregistration took place in SNAP using the Back-geocoding operator which is suitable for Sentinel-1 TOPS scans. After the identical scatterers are identified with the assistance of the DEM, the slave images have to be resampled into the master's frame.

3.1.4. Terrain Correction

At this point, there is one last step before forming the SAR interferograms and triplets, which is the correction of the topographical distortions of SAR images caused over areas with elevated and/or alternating terrain. Those distortions are created, as a result of the nature of the SAR range mapping, reflectance functions and the tilt of the sensor and the geometry of the phenomenon is presented in Figure 3.2. There are different methods available to overcome this issue by compensating for those distortions in order to have an image, the geometry of which will be as close to the real world as possible. In this case, the Range Doppler Terrain Correction operator was implemented and a brief description of the method used will be given. This operator employs the orthorectification method (Schubert et al. 2014) for geocoding SAR imagery. It is a back-geocoding method where the input image (SLC) is resampled onto a provided DEM's geometry (SRTM3) by using the range and azimuth indices as the common denominator. The resampling method set was Bilinear Interpolation. After this step the SAR stacks of Mexico and the Netherlands are exported from SNAP as the implementation of the soil moisture inversion method is done in the MATLAB environment.

3.1.5. Multilook

Loss of coherence, especially related to volume and temporal decorrelation is the major obstacle in the processing of long time series of SAR data. Consequently, it is essential to increase coherence as much as possible, before implementing the phase closure inversion method. A common method to get rid of some of the phase noise is to spatially average pixels and is called complex multilooking. This method was proposed by Goldstein as a way to enhance radiometric accuracy at the cost of image resolution. According to (R. F. Hanssen 2001), multilooking can effectively reduce noise variance of the interferometric phase, assuming spatial smoothness of the signal and ergodicity (Samiei Esfahany 2017). Figure 3.3 shows that the implementation of a multilooking process significantly increases the probability of high coherence.

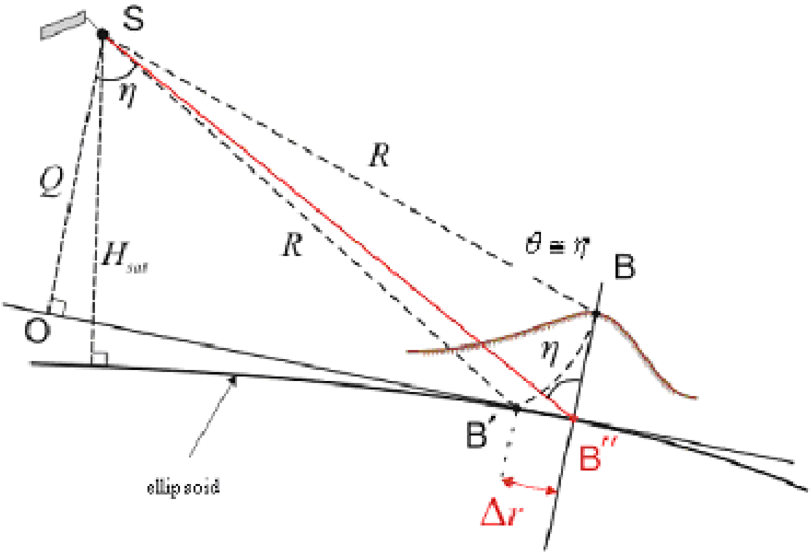

Figure 3.2: Geometry of topographical distortions in SAR imagery (STEP ESA n.d.).

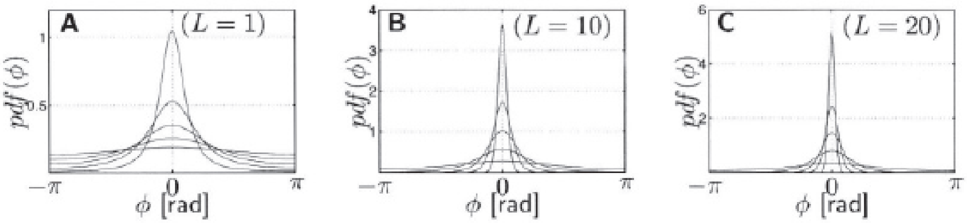

Figure 3.3: Probability density functions for different coherence levels. Slimmer curves correspond to highest coherence. L is the number of multi looked images (R. F. Hanssen 2001).

In this study, in order to increase the coherence levels in both study areas multilooking was applied. To be more specific, a multilooking window of 20x20 pixels was applied in both Mexico and the Netherlands for the sake of consistency. Multilooking results in a coarser pixel resolution, from 5x20m to 100x400m, which is a necessary evil, in the pursue of coherent interferograms.

3.2. Propagation Model

In order to study soil moisture changes over Mexico and the Netherlands using Sentinel-1 SAR data, it is essential to understand how moisture affects the propagation and the backscatter of the signal in the soil. Soil is considered a dissipative (lossy) medium, which means that a significant amount of the energy of a propagating electromagnetic wave is absorbed to heat the medium, thus a percentage of the energy is permanently lost.

3.2.1. Microwave incidence and refraction

Since the soil is lossy, it has to be modelled as such, having complex dielectric properties and a complex refraction index, where the imaginary part of those complex numbers is associated with the energy dissipation of the attenuating wave. Further information regarding the approach towards modelling the dielectric parameters is given at the following subchapter. At this point the geometry of the propagating wave, presented in 3.4, will be explained.

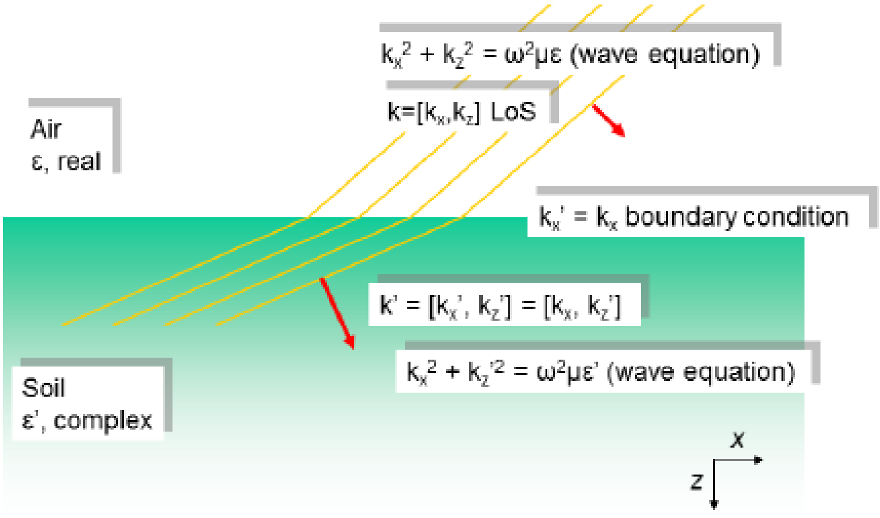

Figure 3.4: Wave propagation and scattering profile of a lossy medium (De Zan, Parizzi, et al. 2013)

The main goal is to associate the propagation of the incident wave with the moisture state of the soil medium and thus with its dielectric properties. To do so, the expected number of an interferogram will be expressed in terms of the wavenumber, which is the spatial frequency of the wave emitted by the SAR instrument. The general wavenumber equation is:

$$\kappa = \frac{\omega}{\upsilon} = 2\pi\lambda \tag{3.1}$$

where $\omega = 2\pi f$ is the angular frequency (radians/sec), f is the wave frequency (Hz), λ is the wavelength (cm) and υ is the phase velocity. The phase velocity is expressed as:

$$\theta = \frac{1}{\sqrt{\varepsilon\mu}} \tag{3.2}$$

Where μ is the permeability of the medium (H/m) and ε is the permittivity or dielectric constant of the soil (F/m also expressed as s2/mH). Combining those two equations, the wavenumber equation for normal incidence (De Zan, Parizzi, et al. 2013) is introduced:

$$\kappa = \sqrt{\omega^2\varepsilon\mu} \tag{3.3}$$

Since the medium is lossy, the wavenumber becomes complex and the wavenumber equation for incidence on a lossy medium is introduced:

$$\kappa_\chi^2 + \kappa_\zeta^2 = \omega^2\varepsilon\mu \tag{3.4}$$

Finally, given the known incidence angle θ_{inc}, which can be retrieved from the S-1 data (for best incidence angle from ellipsoid is chosen), the complex form of permittivity ($\varepsilon = \varepsilon' + \varepsilon''$) and the boundary condition between soil and air $k_x' = k_x$ has to be met, the final wavenumber equation which will be implemented to relate interferometric differences with the soil dielectric constants is derived:

$$\kappa_\zeta'(\varepsilon') = \sqrt{\omega^2\varepsilon\mu - \kappa_\chi^2} \tag{3.5}$$

The expected value of an interferogram with a change in soil moisture and thus varying κ_ζ' as derived by (De Zan, Parizzi, et al. 2013) is:

$$\mathrm{I}(\varepsilon_1', \varepsilon_2') = \int_0^\infty f(\zeta) e^{-j2\kappa_{\zeta 1}' \zeta} (e^{-j2\kappa_{\zeta 2}' \zeta})^* d\zeta \tag{3.6}$$

Where $f(\zeta)$ a scattering profile in the soil.If we assume that the scattering profile is exponential $f(\zeta) = exp(-2\alpha), a > 0$ the resulting interferogram is:

$$\mathrm{I}_{l,m} = \frac{\frac{1}{2}}{j(\kappa_l - \kappa_m^*) + \alpha} \tag{3.7}$$

Now that the equation for a single interferogram is known, the closure phase for any interferometric triplet can be computed using the equation 3.8 to end up with equation 3.9.

$$\Phi_{lmn} = arg(\mathrm{I}_{l,m}\mathrm{I}_{m,n}\mathrm{I}_{n,l}) \tag{3.8}$$

$$\Phi_{lmn} \approx -\alpha^{-3}(\kappa_l - \kappa_m)(\kappa_m - \kappa_n)(\kappa_n - \kappa_l) \tag{3.9}$$

Based on equation 3.9, (De Zan, Gomba, and Yokoya 2018) proposed a simplified alternative to it by getting rid of the wavenumber parameter by approximating a wavenumber difference $(\kappa_l - \kappa_m)$ to be equivalent to a moisture difference $(\theta_l - \theta_m)$ (m^3/m^3). This approximation results in the following equation:

$$\Phi_{lmn} \approx -\alpha^{-3}(\theta_l - \theta_m)(\theta_m - \theta_n)(\theta_n - \theta_l) \tag{3.10}$$

At this point we have two models with slight albeit not negligible differences, the physical model (3.9) and the simplified one (3.10). (De Zan and Gomba 2018) who developed this method, tested both models using L-band (ALOS) data and reported that the physical model returns better results.

3.2.2. Dielectric constant of soil

Estimating and using dielectric constant values of the soil is a tricky field as there is no universal model or database including all soil types. Soil is a four-component dielectric blend consisting of air, bulk soil, bound and free water and hence the dielectric dispersion spectrum is more complex and different from that of a single component. Water alone behaves differently under bound and free condition; however, both are functions of electromagnetic frequency f, physical temperature T and salinity S. Overall, the dielectric constant of soil is a function of f, T, S, bulk soil density pb, the shape of soil particles and water inclusions as well as the total volumetric water content mv (Hallikainen et al. 1985). There are two different semi-empirical models widely used to estimate the soil dielectric constant for different spectra, developed by (Dobson et al. 1985) & (Mironov and Fomin 2009). The first one is part of the SMOS's algorithm since the beginning of its mission and requires sand, clay content and bulk density, while the second one is also implemented in SMOS since 2012 and requires less input parameters, just clay content and temperature (Mialon et al. 2015). In order to relate moisture changes with refraction (De Zan, Parizzi, et al. 2013) chose to use the empirical model proposed by (Hallikainen et al. 1985), which was developed in tandem with Dobson's model (Dobson et al. 1985). Therefore, the same empirical curves will be employed in the current research. The drawback of this model is that it does not take organics into consideration, which will therefore introduce an unknown bias when applied on peat soils where organics prevail.

This inability of the empirical model impedes the application of the method in the Netherlands' case as the soil at both Delfland and Zegveld is mostly peat. Throughout the years quite some research has been conducted towards determining the dielectric constants of various organic soils such as (Mironov and Bobrov 2003) and (Karim, Kamaruddin, and Hasan 2018), yet as of today there is no research linking the percentage of organics to the variation of the

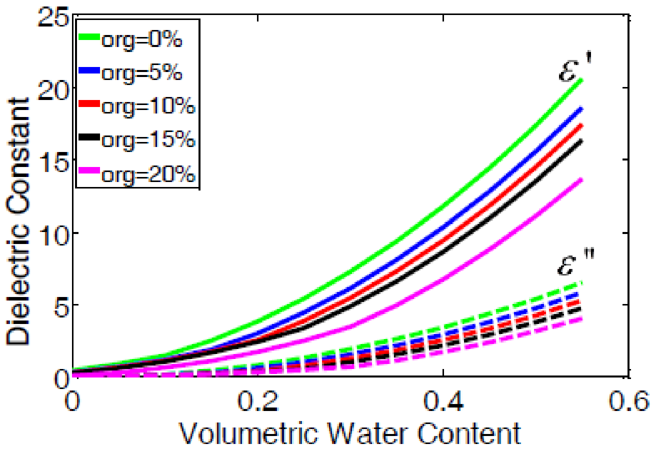

Figure 3.5: Complex dielectric constant values for different organic matter content as modelled by the semi empirical model by (J. Liu et al. 2013)

dielectrics. Satellite missions such as SMOS and SMAP make use of dielectric mixing models but none so far has taken soil organic matter under consideration (Jin et al. 2017).

(J. Liu et al. 2013) proposed a semi-empirical model to describe the behaviour of the dielectric constant at soils with organic matter. The results of this semi-empirical model are presented in 3.5 using soil samples in the respective study area (China). The finings of this study are valid for SOM (soil organic matter) ranging from 0.03 to 17.84%. The drawback of this method, although highly detailed, is that it requires input data in the form of soil sampling, which in tandem with the given uncertainty of the model, makes it unfeasible for this research unless extensive soil sampling takes place which exceeds the scope of the thesis. According to (Lesschen et al. 2012), the SOM varies within the studied region from 5% to more than 20%. To be more specific regarding the area of Delfland the organic matter exceeds 20% of the total soil matter. Among the conclusions of Liu's study (J. Liu et al. 2013) is that organic presence in the soil decreases the bulk density and increases the adsorption forces. This results in a decreased dielectric constant which will possibly lead to an underestimation of the soil moisture changes unless it is being taken into account.

Calling back on those findings we expect the emergence of a systematic error in areas where organics are a prevalent part of the soil texture, potentially rendering the physical model unreliable in terms of accurate value prediction. However, the major concern of this study is whether C-band closure phases can determine the changes in soil moisture For this reason, in the case of the Netherlands (where organics prevail) both physical and simplified soil moisture inversion methods will be implemented to examine whether the simplified model will prove to be more accurate than the physical one.

3.3. Replication of the closure phase inversion method

The closure phase inversion method consists of a number of processes as shown in Figure 3.6. The entirety of the inversion method was done using MATLAB. The post processing of the resulting images was done part using Matlab and part using QGIS.

3.3.1. Initial optimization of the inversion algorithm

The goal of this part is to obtain a set of moisture values which will explain the observed closure phases. Consequently, the first step is to generate those closure phases for each one of the study areas. For any N given number of images there is a set amount of possible closure

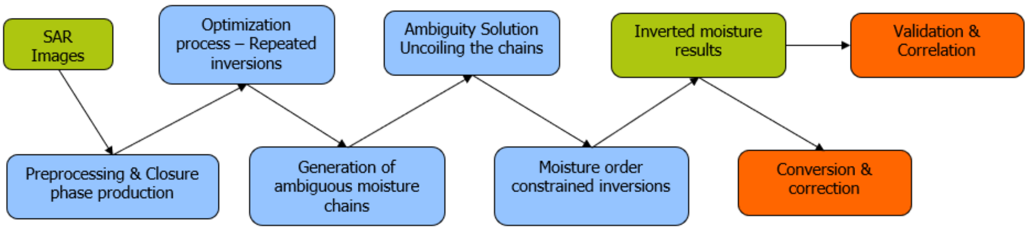

Figure 3.6: Process scheme of the inversion algorithm

No. of images	No. of Fourier phases	No. of independent closure phases	% of phase information
3	3	1	33,1
6	15	10	66,7
11	55	45	81,8
21	210	190	90,5
50	1225	1176	96,0

Table 3.1: Percentages of phase information depending on the number of acquisitions.

phases according to (Monnier, Perrin, and Malbet 2003),

$$''N\,choose\,3'' : \frac{(N)(N-1)(N-2)}{(2)(3)} \tag{3.11}$$

However, not all of them are independent, since the independent Fourier phases are ($''N\,choose\,2'' :$ $(N)(N-1)/2$. In order to compute independent phase closures, one image has to be fixed, in our case the first image acquisition time wise. The independent closure phases now for $N-1$ images are $(N-1)(N-2)/2$ and therefore as many will be computed for the implementation of the inversion method. The drawback is that since the computations are made for $N-1$ images, the algorithm does not have enough sensitivity to estimate the initial moisture level.

An important remark is that the independent closure phases will always be less than the Fourier phases, meaning there will always be a phase information deficit, which goes down as the number N increases 3.1.

$$\%\ of\ phase\ information = \frac{No.\ of\ independent\ closure\ phases}{No.\ of\ Fourier\ phases} \tag{3.12}$$

In our case, due to limitations on computing power, sets of 11 acquisitions will be used (and a set of 6 purely for reference and comparison purposes). Once the prerequisite closure phases are produced from the collected data, they will be used as input of the inversion algorithm, whereas the moisture levels will be the unknowns. These moisture changes will be estimated by minimizing the follow figure of merit (residual sum of squares):

$$f(\theta) = \sum_{l,m,n}^{y} (\Phi'_{l,m,n} - \Phi_{l,m,n})^2 \tag{3.13}$$

Where the primed symbols are the observed triplet values, the unprimed ones are determined from the propagation model and y is the number of times the minimization algorithm is repeated per pixel. For the optimization process a gradient descent iterative algorithm is required. For this study the fmincon, nonlinear multivariable, function was employed.

The minimizing procedure is repeated with different random starting points in order to achieve a global search, since we know there can be more than one local minima. The moisture values have to be manually constrained during the minimization process and the triplet differences will be wrapped in the $[-\pi, +\pi]$ range, which is directly responsible for the arising ambiguities. Each solution returns a possibly correct solution, correct being a solution where the acquisitions are correctly ordered based on their moisture level. The solution with the smallest cost per pixel is considered to either be the correct one or, due to the permutation symmetry of phase triplets, a circularly equivalent one.

For more details on the subject of permutation symmetry, the reader is referred to the phase closure subsection of Chapter 2.

3.3.2. Solving the ambiguity

At this point, we have a potential solution in the form of a moisture sequence, which can be reorganized in a monotonically increasing order and due to the ensuing ambiguities is subject to circular permutation symmetry. For example assuming that a solution to a 7 acquisition minimization problem is the following moisture sequence monotonically sorted from highest to lowest: [3,1,5,7,6,2,4]. Every other solution where the values are circularly shifted ([5,7,6,2,4,3,1] or [1,5,7,6,2,4,3]) are equally viable and there is no way to distinguish them, thus the solution is constrained on a ring where the relative position of each element is known but there is no way to tell where the array starts and ends. In essence, an optimization algorithm based on closure phases will order the acquisitions correctly according to the moisture level, provided that the result is put on a ring. It has no way to determine where the breaking point of the ring is; it being between the wettest and driest acquisition

The scope of this step is to break and unfold the ring like solution, thus getting rid of the ambiguity. To do so extra data are needed for the obstacle to be overcome and for this reason the parameter of interferometric coherence will be employed (De Zan and Gomba 2018). The goal at this point is to tell the wettest from driest acquisition which due to the circular permutation have to be next to each other and uncoil the permutation chain 3.7. The basic assumption is that changes in soil moisture result in different backscattering and thus loss of coherence and consequently, coherence must be higher for pairs with similar soil moisture or minor change.

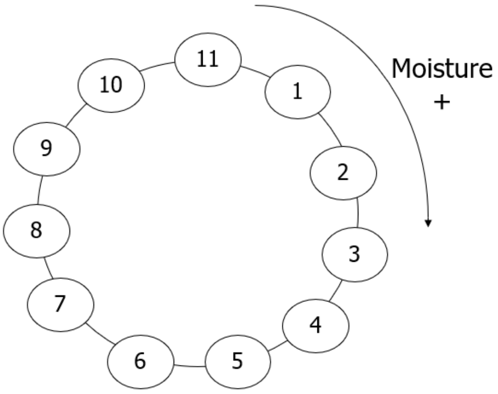

Figure 3.7: Example of a circularly permutated moisture order. Finding the link between wettest and driest is the key to solve the ambiguity.

A most important limitation of this method is the necessity of sufficient temporal coherence between all images. In this vein, Longer wavelengths are preferable over shorter ones (De Zan and Gomba 2018). Sentinel-1 12-day overpass together with the inherent fast decorrelation

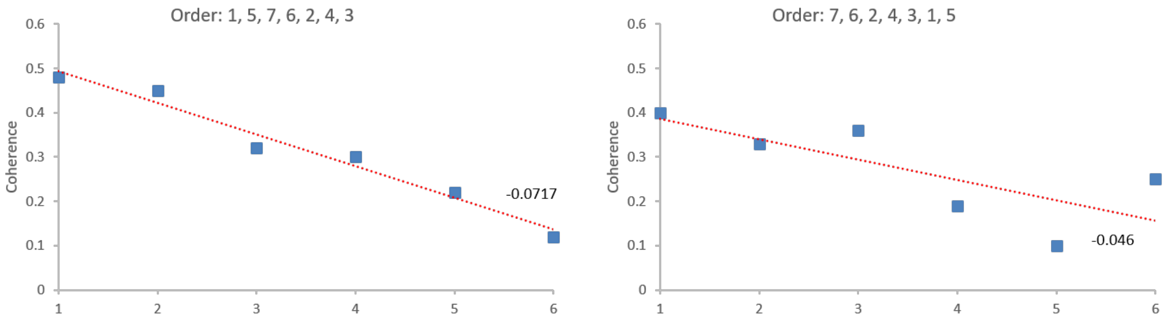

(a) (b)

Figure 3.8: Example of ambiguity solution. Coherence plots for two maximum candidates 1 (a) and 7 (b)

rate of C-band data makes it difficult to get adequate coherence over time, especially between acquisition with a large temporal gap.

Based on the assumption stated before, the procedure which takes place individually for each pixel is as follows:

1. Each one of the images is individually tested as being the wettest element of the chain. The absolute coherences between the "wettest" image and the rest are computed.
2. The results are plotted where the ordinate is the absolute coherence and the coordinate is the distance on the moisture order.
3. A trendline of the coherence data is generated and its angle with the x axis (gradient) is computed.
4. Steps 1-3 are repeated as many times as the number of acquisitions put on test. The steepest trendline is considered to be associated with the correct wettest acquisition at the head of the moisture chain.

For example, let's make use of the hypothetical 7 acquisition optimization mentioned before. The optimization algorithm sorted the 7 acquisitions monotonically in decreasing order: [3,1,5,7,6,2,4], where any circular shift has a possibility to represent the correct order. Two out of the 7 candidates will be examined for being the "wettest"; image 7 and image 1. Figure 4.6 presents the coherence plots of both moisture orders. The trendline of the left plot has the steepest downward trendline between the two and thus its moisture ordering, with image 1 as the highest moisture, is more likely to be the correct one compared to theother one. In practice, coherence plots for every possible circular shift is produced since every acquisition has the potential to be the one at the top of the moisture order.

3.3.3. Final moisture results & conversion to interferometric variables

Once the circular permutation ambiguities are solved, the final step of the inversion algorithm can take place. This final step consists of yet another minimization using a gradient descent algorithm. The distinguishing feature is that the correct moisture order obtained at the previous step is now inserted as a constraint. The moisture value of the first image has to be deemed fixed and known, since the sensitivity of the closure phase method is not adequate to recover it. Values from the available validation data will be used to compensate for the unknown initial soil moisture.

According to (Zwieback, Hensley, and Hajnsek 2017), the effect of soil moisture changes on DInSAR surface displacement measurements is random error of about 10-20% of the radar wavelength. Sentinel-1 C-band's frequency of 5,405 GHz corresponds to a wavelength of 5,5 cm, so an error of 0.55 to 1.1 cm due to soil moisture is expected. The soil moisture timeseries extracted from the inversion method are used in an attempt to compensate for this spurious displacement. The moisture related interferometric phase and coherence maps are then used to examine whether they can offer useful correction or just introduce even larger errors.

3.4. Evaluation of soil moisture product

The outcome of this study has to be evaluated and externally validated. Ideally, both remote sensing and ground truthing generated data would be used for cross-correllation and validation. However, the validation process varies between the study areas as the Netherlands have a rich database of timeseries on different kind of data which can prove to be useful for the needs of this study. The common denominator between the 2 areas is the result comparison with SMAP data.

Before that however, the SAR parameters need to be assessed in order to check whether the current dataset (repeat interval, coherence, closure phases) is adequate to obtain meaningful soil moisture data using the inversion algortihm. This will be done using the decorrellation rate estimation method (Morishita and R. Hanssen 2014) mentioned in Chapter 2.

For the purpose of the validation SMAP's "Surface Soil Moisture 9km (L4, Model Value-added)" dataset was used. This layer contains model-derived global volumetric surface soil moisture (3.9) on the top 5 cm of the soil column. The L4_SM algorithm is built on the ensemble Kalman filter, merging passive L-band observation together with estimates from a land surface model (National Snow Ice Data Center n.d.).

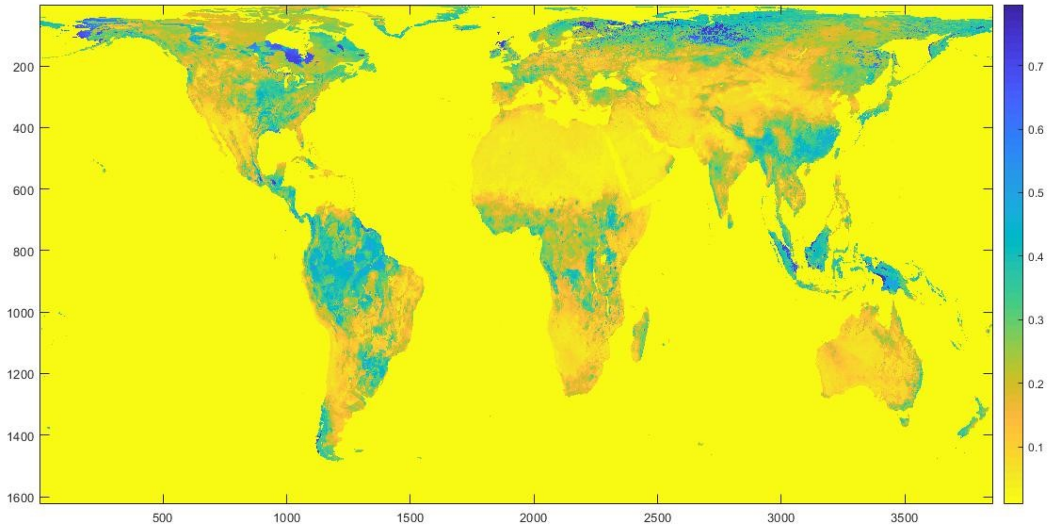

Figure 3.9: Example of world map SMAP L4 surface moisture imaging.

The Soil Moisture Active Passive project is a NASA mission aiming to set up a satellite observatory providing data about the moisture content of the upper soil (top 5 cm of the soil) as well as its state (frozen/thawed). The satellite fleet was launched January 31 of 2015 and the the first results were obtained in April of the same year. Initially it was designed to make use of an L-band radar (active component) and an L-band radiometer (passive component), but since the radar's failure in the 7th of July 2015, soil moisture data are provided by the radiometer alone (National Aeronautics and Space Administration 2015). The brightness data obtained by the radiometer are processed and analyzed in order to enhance them (sharpen resolution with additional data) and provide the desired product of soil moisture (L4_SM algorithm).

Regarding the Netherlands, the validation process apart from the SMAP spaceborne data will also include ground truthing and correlation with precipitation. For the ground truthing, time series of soil moisture data was provided by the municipality of Zegveld at the province of Utrecht. Zegveld soils have a similar texture to the ones found in Delfland in a sense that are both dominated by the presence of organics. The soil moisture is estimated with the use of 2 sensors providing hourly logs from March 2016 to September 2018. In order to be as precise as possible, as a matter of consistency and since the acquisition time of the SAR images is a known variable, the ground-based data will be selected accordingly. The precise observation time, which is provided in the form of metadata by ESA, is 19:25 CEST (17:25 UTC) and is the same for each subsequent acquisition. Consequently and since the Zegveld data are provided per hour, the correct value will be extrapolated using the moisture values at 18:00 and 19:00 CET.

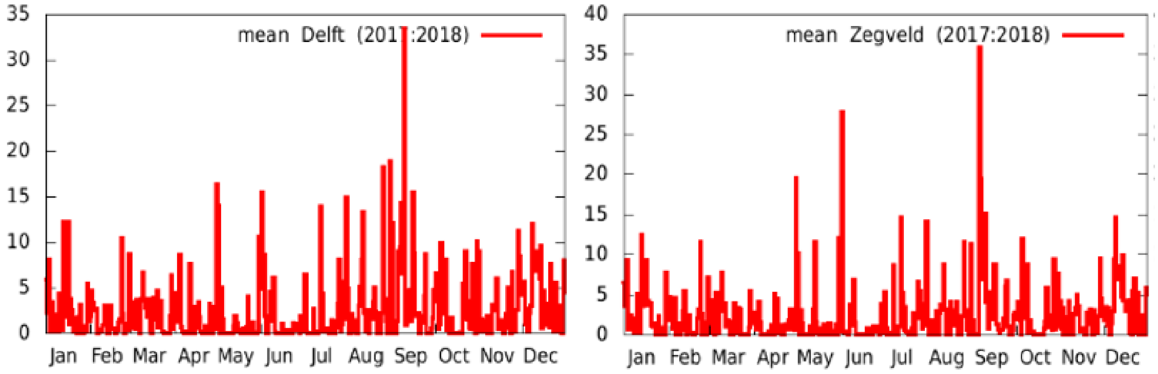

Figure 3.10: Annual cycles of daily precipitation (mm/d) for Delft (left) and Zegveld (right) documented by the KNMI stations located at the respective areas. The daily timeseries were used to evaluate the implementation of the soil moisture inversion (Koninklijk Nederlands Meteorologisch Instituut 2019)

Usually, soil moisture changes are associated with rainfall events. Normally, moisture decays over time in absence of rainfall events as the available water either evaporates under sunlight, is absorbed by vegetation or infiltrates to the soil. Regardless, in case of a rainfall event the water content will sharply increase. This somewhat consistent behaviour allows the correlation of soil moisture and its associated coherence loss with precipitation. Hence, a Pearson correlation test between the ground truthing soil moisture data and precipitation will be done. Moreover, due to the connection between soil moisture and precipitation, the Zegveld dataset throughout the study period will be correlated with the KNMI data using once again the Pearson method.

4

Results

In this chapter the main results of the closure phase generation, soil moisture inversion and land deformation corrections are presented and discussed. Due to the large number of produced maps presenting different (SAR related) parameters, only some of them will be presented at this chapter. The appendix includes complete sets of those maps.

4.1. SAR Parameters

The two most important SAR parameters for the detection of soil moisture variations according to the closure phase inversion method are the coherence of the SAR signal and of course the closure phase. Hence it is imperative to briefly present, how these parameters vary throughout the time series. As stated in Chapter 3, for each dataset of 11 acquisitions, a set of 55 and 45 coherence and closure phase maps respectively was produced in order to be used as input in the inversion method proposed by (De Zan and Gomba 2018).

Figure 4.1 shows four respective coherence maps resulting from using acquisitions with the smallest possible interval of 12 days. Brighter areas correspond to areas less changed within those twelve days. It is interesting seeing as even though the average coherence varies greatly between all four maps there are certain patterns arising from the different land types. Moreover, one can assume that this homogeneous lack of coherence in maps 1b and 1c is caused by rainfall events taking place between each pair of acquisitions. In general, coherence is dropping, as expected, as the time interval between acquisitions grows larger.

In a similar fashion, Figure 4.2 presents coherence maps for two different acquisition pairs of the time series for Netherlands. In this case, the 12 day coherence shows lower variability over time than its Mexican counterpart. This can be possibly attributed to the absence of variety in land use, since the study area in the Netherlands consists of either urban areas which naturally return high coherence and of areas with either pasture or agriculture which were exected to have low coherence values. This lack of variability explain the presentation of only two coherence maps.

Closure phase or phase triplet is the integral parameter of the method implemented. Since it is plagued with ambiguities, and different soil moisture series may result in the same triplet value, the sign is not a very useful indicator of the level of soil moisture change. The magnitue of the triplet on the other hand can provide some early warning on whether change is to be expected or not. For this reason as well as to make the maps more intuitive and easier to read, the triplet data will be presented in absolute values. The resulting maps are presented in figures 4.3 and 4.4 for Mexico and the Netherlands respectively.

Concerning the study area in Mexico (Figure 4.3), sub-figure 1a's low closure phase indicates that disturbances caused by precipitation are limited which is expected as the raining season

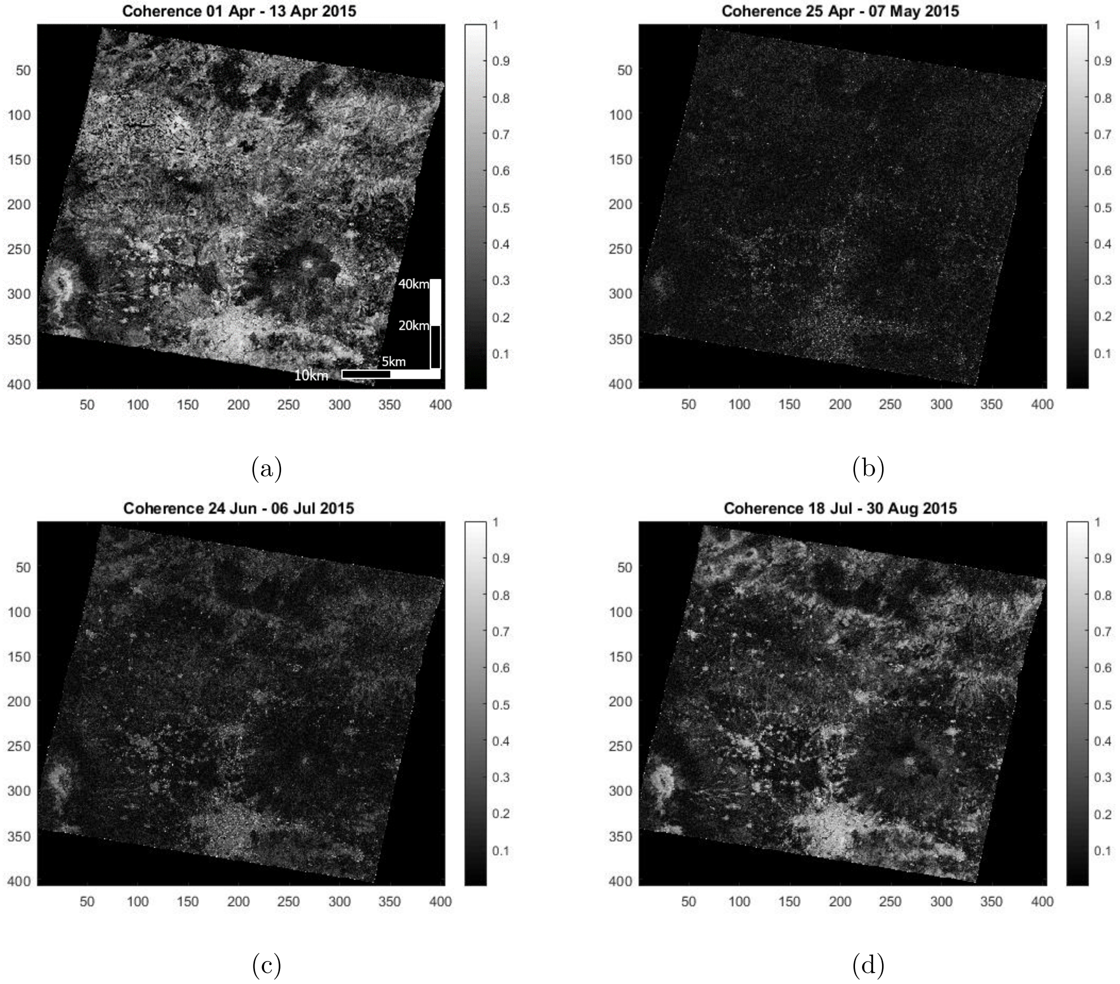

(a) (b)

(c) (d)

Figure 4.1: Coherence maps of the study area in Mexico at four different time stamps. For the sake of consistency, for all four maps displayed, SLCs with an interval of 12 days were used

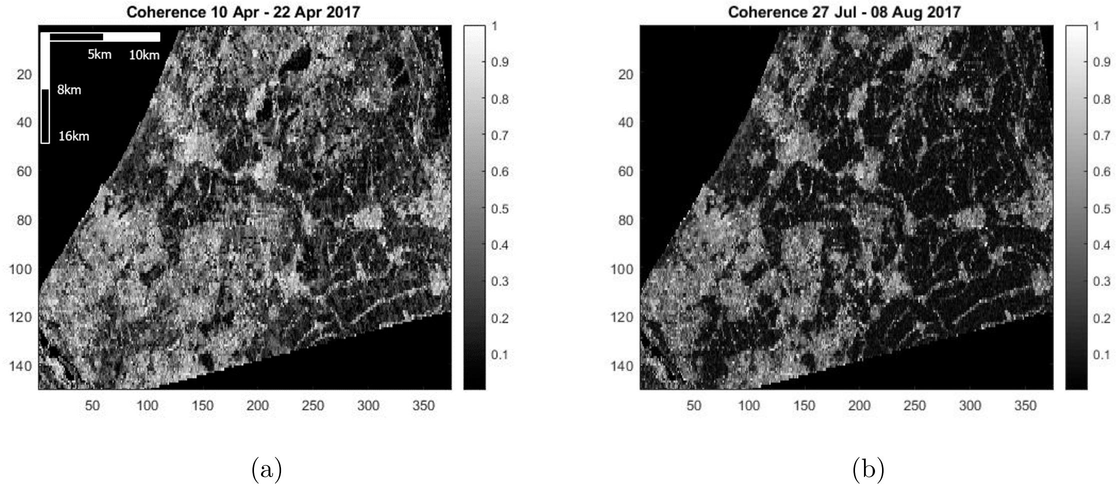

(a) (b)

Figure 4.2: Coherence maps of the study area in the Netherlands at two different time stamps both with a time interval of 12 days

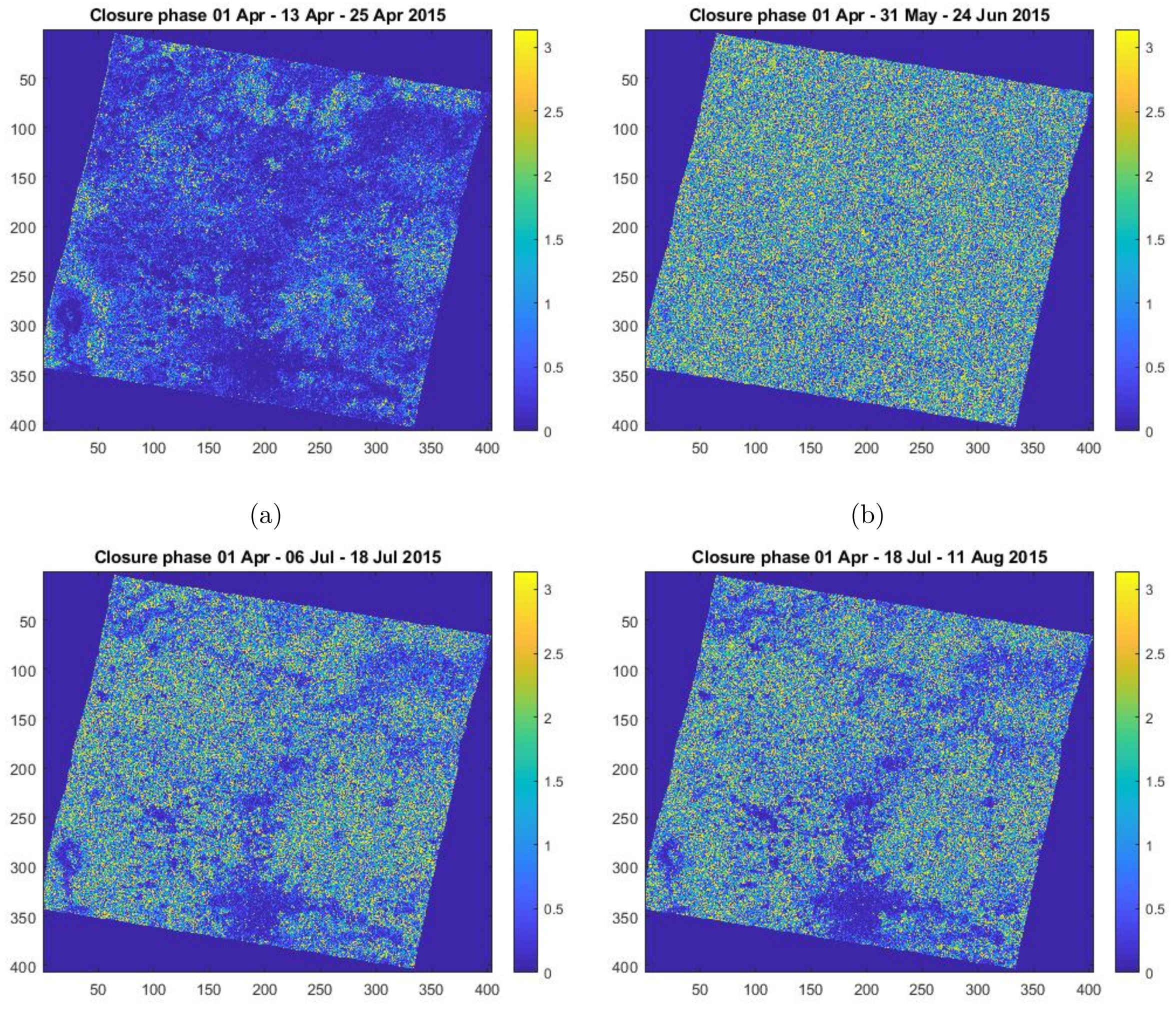

(a) (b)

(c) (d)

Figure 4.3: Closure phase maps of the study area in Mexico at four different time stamps. 1a low levels of closure phase is related to low monthly precipitation, especially when compared wwith 1b which lies in the middle of Mexico's wet season

usually does not start untl May or even June, while 1b is a prime example of a map implying a vast and sudden change in surface soil moisture at some point before the third acquisition. In 1c and 1d one can see that there are changes caused to temporal and volume decorrelation, however there are areas where change was expected to be imited and in fact is.

Now, concerning the study area in the Netherlands (Figure 4.4), the situation shares some similarities with the previously mentioned Mexico case. The most important observation is that the disturbance caused by a precipitation effect together with the moisture profile antecedent to the acquisitions may induce a signal greater or equivalent to the one caused by a large time interval. Comparison between 1a and 1b shows that the magnitude of a precipitation effect is apparent in urban areas (0.21 to 0.11) while it is similar to a temporal decorrelation effect caused by a total interval of 140 days between acquisitions (0.96 to 1.06).

Furthermore, what is even more interesting and surprising, is the fact that the greatest disturbances (greater triplet signal) were recorded in all closure maps where the middle acquisition was the one of the 4th of May, which coincides with a rather mild precipitation event. This shows that precipitation events are not solely responsible for this kind of noise induced

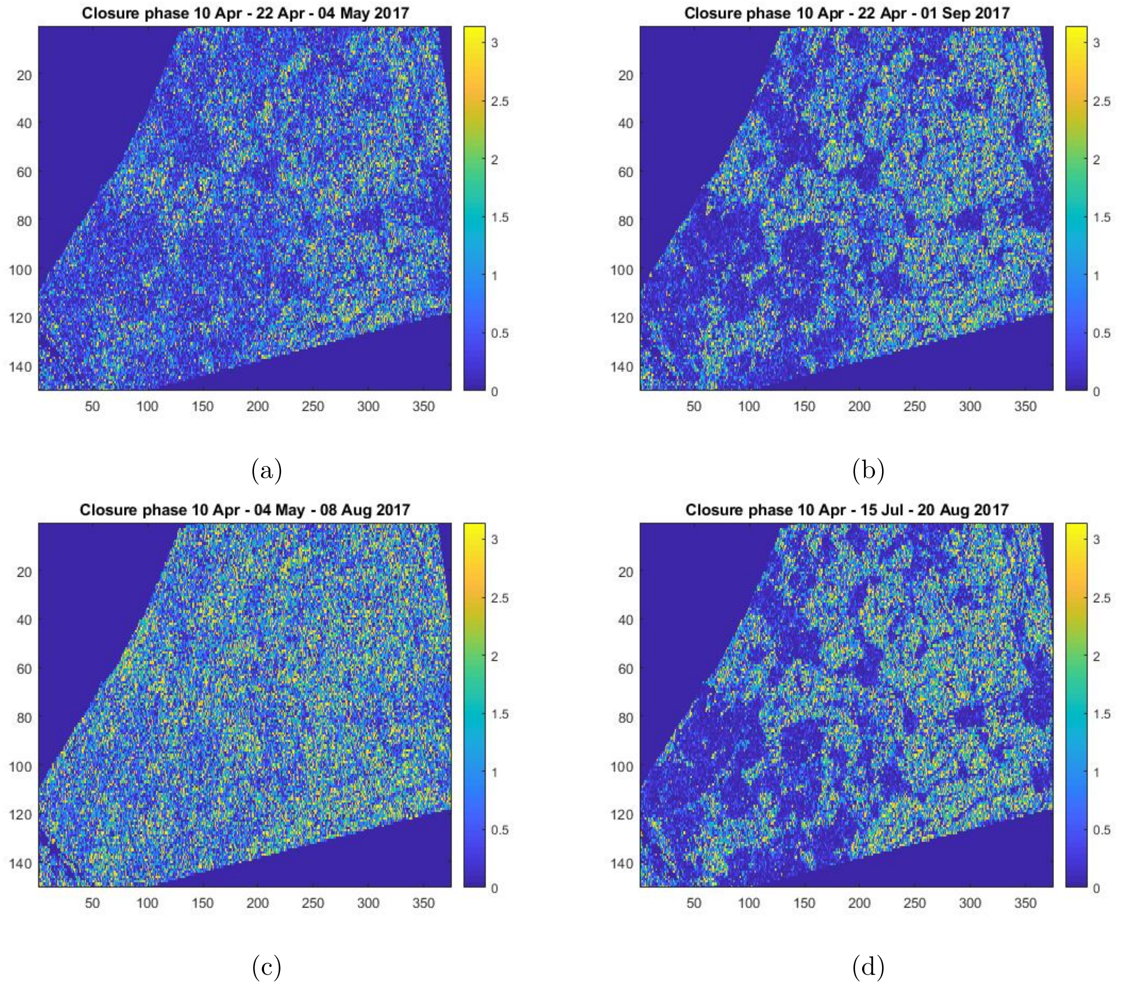

Closure phase 10 Apr - 22 Apr - 04 May 2017

Closure phase 10 Apr - 22 Apr - 01 Sep 2017

(a) (b)

Closure phase 10 Apr - 04 May - 08 Aug 2017

Closure phase 10 Apr - 15 Jul - 20 Aug 2017

(c) (d)

Figure 4.4: Closure phase maps of the study area in the Netherlands at four different time stamps.

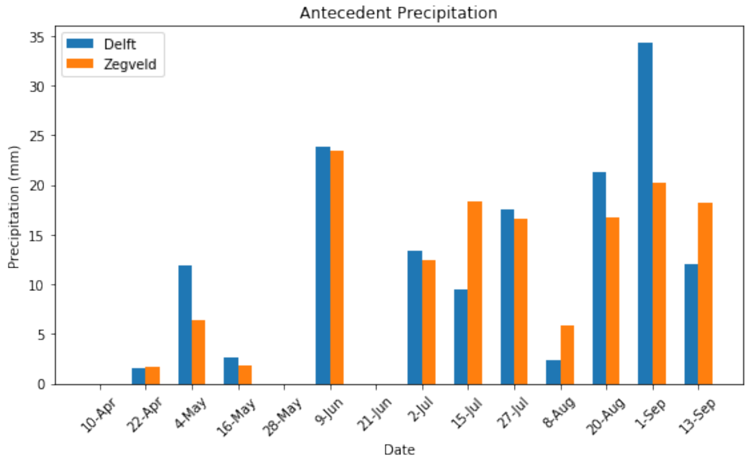

Antecedent Precipitation

Figure 4.5: Antecedent precipitation estimated by using data provided by KNMI. The sensors in Delft and Zegveld have a correlation rate of 0.88

into the signal, but rather the degree of moisture change caused by the dipole of precipitation and antecedent soil moisture. To conclude, coherence and as a result, the closure phase magnitude is defined by both precipitation induced noise as well as differences in the soil moisture

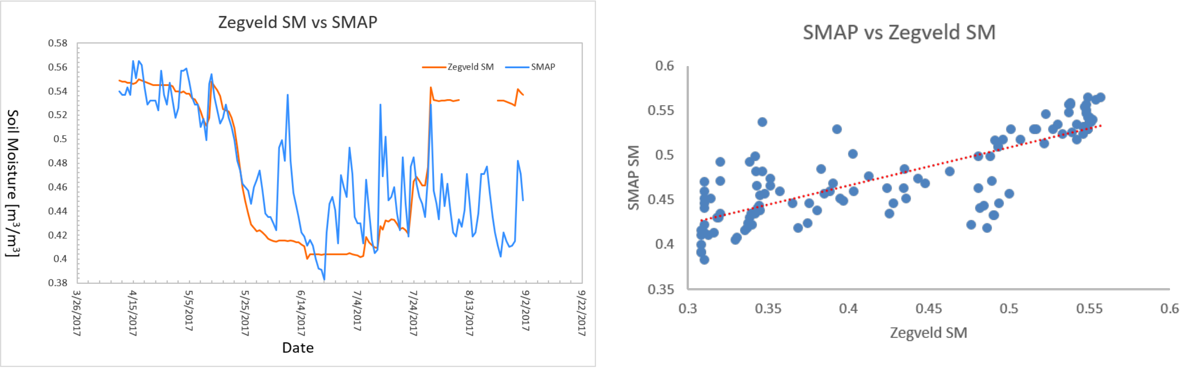

(a) (b)

Figure 4.6: Left: The Soil Moisture time series as observed by SMAP and two ground sensors at Zegveld, Netherlands. Both sensors were deactivated from 10/8 to 22/8, hence the absence of measurements. Right: The corresponding scatter plot.

state between the 3 images employed to create the phase triplet.

Naturally, precipitation is the mechanism responsible for replenishing the soil moisture, however modelling their interaction is complex and out of scope of this thesis. A Pearson correllation was run between the precipitation data provided by KNMI and the two available soil moisture products (Zegveld sensor and respective SMAP time series). The Pearson correllation factor was calculated at 0.015 and 0.001 for Zegveld and SMAP, showing that the two phenomena are uncorrellated and thus confirming that they need to be considered independently. Figure 4.5 presents the precipitation data as recorded by the KNMI network at the Delft and Zegveld stations. One can easily deduce that the two sensors are highly correllated and similar rainfall patterns can be observed.

Next, the groundtruthing of the SMAP dataset was done using the two ground sensors located at Zegveld. One must take into account that the resolution of SMAP (9x9km) is too coarse and it would require a network of sensors to get optimalresults. However, the correllation between SMAP and both sensors was high (0.79 0.74), showing that SMAP can accurately estimate soil moisture over the Netherlands. Figure ?? presents the two datasets. For the correlation the data beyond the 10/8 were not taken into account due to the time gap from 10/8 to 22/8 where both sensors were deactivated. Naturally, SMAP is less sensitive to changes due to its coarse resolution. Nevertheless, SMAP seamslessly follows the correct soil moisture pattern throughout the 140-day window.

4.2. Inversion algorithm

Before we proceed with the algorithm's results,the basic rules and assumptions binding this thesis research will be layed down.

- It is assumed that the main drivers behind phase closure signal are precipitation, soil moisture and decorrellation.
- The Halikkainen model is implemented to determine the dielectric constant of the soil at both study areas. The first assumption is that each area is covered by soil of more or less same texture and hence a single soil texture is used for each.
- Urban areas are being regarded as soil despite the obvious fallacy. Unfortunately, the implemented algorithm is unable to discern between urban and rural areas and due to migration issues between SNAP and MATLAB georeferencing of the SLCs is lost, thus a land cover mask can not be implemented.

- Due to the massive amount of computations; 30 optimizations and 11 coherence plots for ambiguity solution per pixel (164.428 pixels for Mexico, 56.250 for the Netherlands) it is virtually impossible to present intermediate results. For this reason, during the development of the code, the algorithm was initially run for random pixels to check whether the results made sense. After the code was finished algorithm was run for the whole image, pixel by pixel.

The implementation of the inversion algorith is performed for four distinct cases as shown in Table 4.1. The minimization process was run a total of 30 times, for each pixel individually to ensure that the correct solution will be chosen out of an adequate number. The number of times this process is repeated in tandem with the size of the images used affects the computational time. The duration of the computation for Models 1 to 4 was 8.4, 3.9, 2.8 and 1.7 days respectively. For reference, the grid in Mexico was 407x404 pixels while the one in Holland was 150x375 pixels. At this stage the optimization may result in either the correct solution, a circularly equivalent or a different "incorrect" one. After every optimization the resulting moisture sequences are put in an array together with their cost as an index. Every array is examined on whether it is a circular equivalent of a previous one and when that happens a frequency index is added.

Figures 4.7 and 4.8 present some of the resulting solutions for the behaviour of a single pixel throughout the time-series. Since it is a single pixel we are in no position to a priori decide which sequence is the correct one using validation data of any form. Two indicators are needed to detect the "correct" chain, the first one being the total cost of the per pixel residuals and the second one being the frequency of the different solutions.

A/A	Study area	No. of SAR acq.	Model type	Start date	End date
1	Mexico	11	Physical	April 1st 2015	August 11th 2015
2	Mexico	6	Physical	April 1st 2015	August 11th 2015
3	Holland	11	Physical	April 10th 2017	September 1st 2017
4	Holland	11	Simplified	April 10th 2017	September 1st 2017

Table 4.1: Characteristics of the four implementations of the soil moisture inversion model

In the case of the 11 acquisitions(Figure 4.7), figure (d) has the highest cost and can be thus ruled out while (a), (b), (c) have similar cost, which is possible due to the ambiguous nature of the phase triplets. Furthermore, out of the 3 remaining solutions, options (a) and (c) are circularly equivalent and thus this sequence satisfies both criteria of frequency and minimum cost. Solution (a) and its circular equivalents (such as b) in this case appeared 8 out of 30 times.

In the case of the 6 acquisitions(Figure 4.8), there are 2 occurring patterns, with the algorithm detecting either 2 (figures a,b) or 1 (figures c,d) local/absolute minima. The former group has a considerably lower function cost on average but it appears less frequent than the latter; frequency index of 5 vs 9 out of a total of 30 optimizations. In such cases the algorithm is set to prioritize the cost criterion over the frequency. Further discussion on this decision is found on the respective chapter.

The main weakness of the optimization step which reflects on the resulting moisture sequence has been observed to be the exaggeration of the minima. Both fmincon and lsqnonlin have been tested in this thesis and the differences among the 2 are negligible. The reason these two methods were chosen is that both of them have the possibility to detect local minima, in non linear multivariable function. However, in the case of phase triplets, it seems that the local minima are often over exaggerated to the point of becoming absolute minima. Consequently, although the optimization step achieves its purpose in detecting whether the moisture increases/decreases between subsequent acquisitions, it fails to grasp how each of the acquisitions is related to the rest of the dataset.

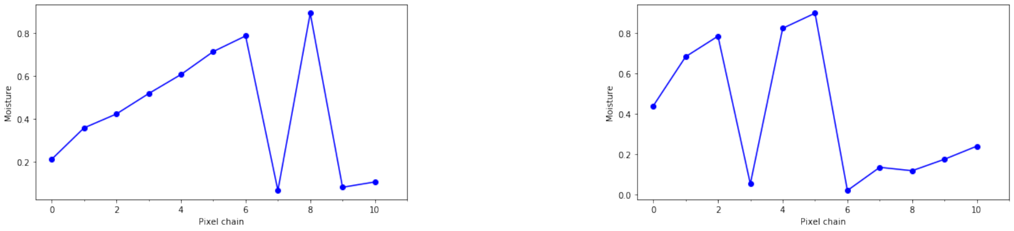

(a) Cost: 250 (b) Cost: 290

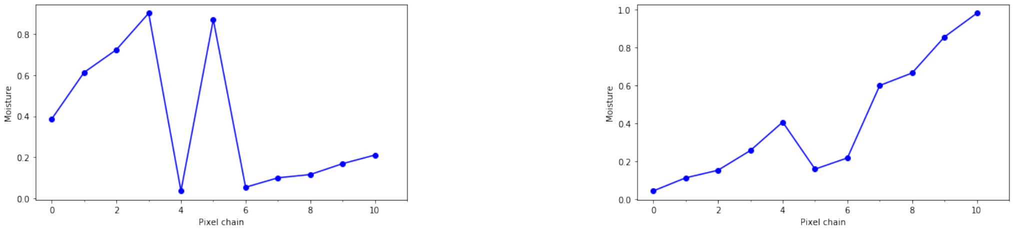

(c) Cost: 255 (d) Cost: 372

Figure 4.7: Single pixel moisture sequences estimated by the minimization algorithm in the 11 acquisition Mexico model, with random initial values. Each run of the minimization algorithm may result in a correct sequence, a circularly equivalent one or a completely different one.

(a) Cost: 25 (b) Cost: 21

(c) Cost: 35 (d) Cost: 33

Figure 4.8: Single pixel moisture sequences estimated by the minimization algorithm in the 6 acquisition Mexico model, with random initial values. Each run of the minimization algorithm may result in a correct sequence, a circularly equivalent one or a completely different one.

4.3. Inverted moisture results & validation

Now that the ambiguities have been dealth with and the moisture order per pixel has been established, the constrained inversion developed by De Zan and Gomba 2018 can be performed.

4.3.1. Mexico Model 1

The results of the first model are presented in Figure 4.12. Unfortunately, the validation in Mexico can not be done using ground data since no public access sensors were found. Figure 4.9 presents the comparison between the modelled and the SMAP product over the whole area, with the modelled moisture having the same trend as the respective one generated from SMAP albeit in a much more crude form. The inability of the optimization step to detect all local minima is reflected on the end result with the inverted moisture data unable to correctly model the moisture drop in acquisitions 3 & 6 (25/4/2015 & 12/6/2015). However, the inversion model correctly presents the upward trend from the start of the time series up to the 8th acquisition (6/7/2015). After the moisture peaks there is a sharp drop to an absolute minima instead of a local as estimated by NASA's satellite. Furthermore, although the inversion constrain has been set to coincide with the SMAP estimates, the model steadily slightly overestimates soil moisture until the maxima and then underestimates it.

Upon taking a closer look at the eleven generated soil moisture maps, one can see that there is little spatial variability at images three to seven. In fact, the speckle takes over and it is hardly possible to discern anything. This spatial variability improves drastically after the seventh image with patterns emerging, indicating that the inversion algorithm works differently depending on the land cover type.

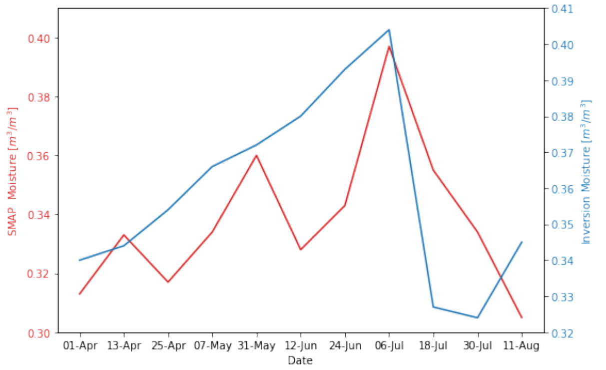

Figure 4.9: Comparison of Mexico inversion results with validation data (SMAP).

Upon closer inspection of the resulting moisture plots, one can see that the modelled moisture varies depending on the land cover type. The studied area was divided into five major land cover types: urban, forest, low vegetation to bare soil and 2 types of cropland. This distinction was made using land cover data provided by ESA as shown in Figure 4.10. Cropland was split in two sub types in order to get some insight into the areas on the northwest part of the region whose response differs, compared to the rest of the cropland.

First, the decorrelation rate is estimated to evaluate the impact of temporal decorrelation on the different land cover types. According to 4.11, on one hand, the coherence of urban and low vegetation to bare soil land types does not decay over time, meaning that the effect of temporal decorrelation is negligible. On the other hand, croplands and forested areas are more susceptible to decorrelation, since coherence decays fast and long term coherence is close to zero. In fact the decorrelation rate was estimated to be 7 days for cropland 2 and 12 days for forest and cropland 1. Consequently, the 12 day interval of Sentinel-1 is not adequate to counter

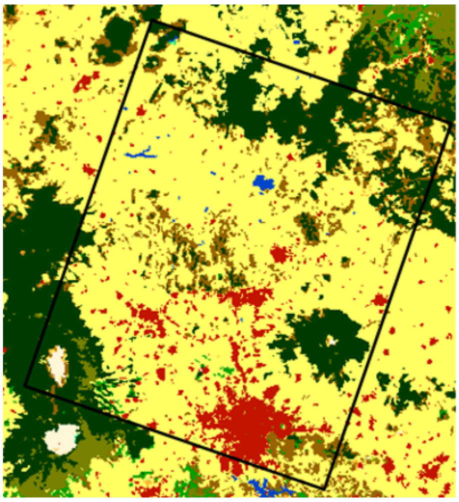

Figure 4.10: The region of Puebla and its land types as detected by ESA. Red is urban, Yellow is cropland, White is bare soil and Green is forest (ESA CCI Land Cover).

the rate the signal decorrelates over vegetated areas, thus we expect temporal decorrelation to affect the inversion algorithm.

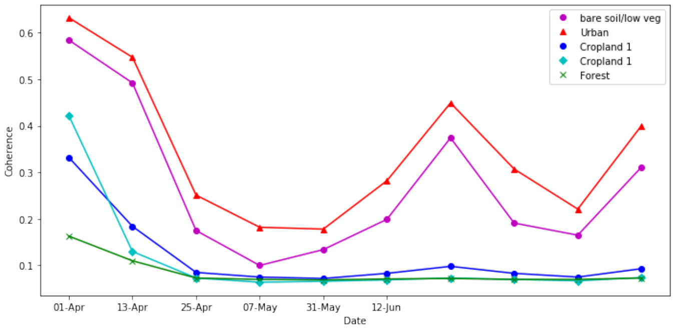

Figure 4.11: Histograms of the decorrelation rate τ for the different land cover types.

According to the results the urban type and the little to no vegetation have very similar, if not identical soil moisture behavior. This is an unexpected finding since the man-made environment of an urban area is supposed to behave quite differently compared to nature. A possible explanation to that would be that urban areas in rural Mexico are not covered purely by concrete meaning that the effects of precipitation soil is also apparent. Furthermore, the SMAP algorithm masks out and disregards urban areas. Consequently, SMAP measurements above such urban areas reflect the soil moisture in the non-built part of it.

In an attempt to further assess the consistency of the results and to better understand and quantify how coherent the results are per land type, Figure 4.13 was produced. This Figure shows the index of the image with the highest moisture, individually per pixel, according to the algorithm's outcome. It can be seen, that for most pixels image four is the one with the highest moisture, although there are a lot of patterns coinciding with the land types already mentioned. Moreover,there are also a lot of pixels where the index points to a different image. This means that for many pixes, the algorithm could not detect the correct maximum resulting in an incorrect moisture sequence and thus image speckle. Table 4.2 shows which image appeared mostly within the pixel pool of each land type, as well as the variance of pixels within the said land type. On one hand, it comes to no surprise that urban and bare soil land types have the lowest variance indicating homogeneity, which gradually increases from lower vegetation to the two cropland types and finally to forest. The high variance of the latter two shows that the inversion algorithm behaves poorly in areas covered by vegetation and the results are rather inconsistent. This poor behavior can be attributed to the aforementioned decorrelation rate τ.

A/A	Land cover type	Majority	Variance
1	Urban	8	3.1
2	Bare Soil/ Low Vegetation	8	3.9
3	Cropland 1	8	7.3
4	Cropland 2	9	6.7
5	Forest	8	9.2

Table 4.2: Majority and variance of highest moisture image index

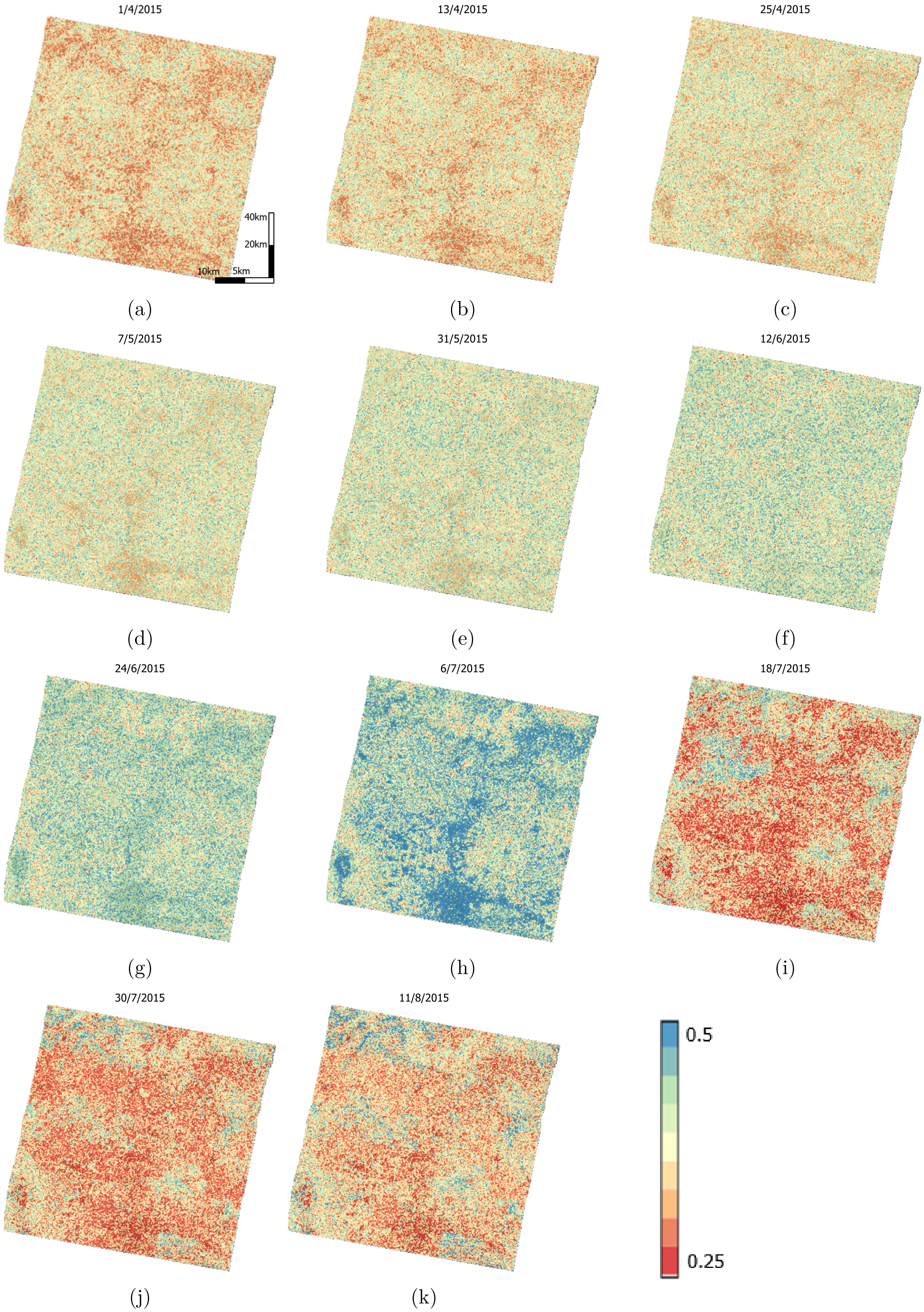

(a) (b) (c) (d) (e) (f) (g) (h) (i) (j) (k)

Figure 4.12: Volumetric Soil Moisture (m^3/m^3) inversion results for the 11 acquisition Mexico model.

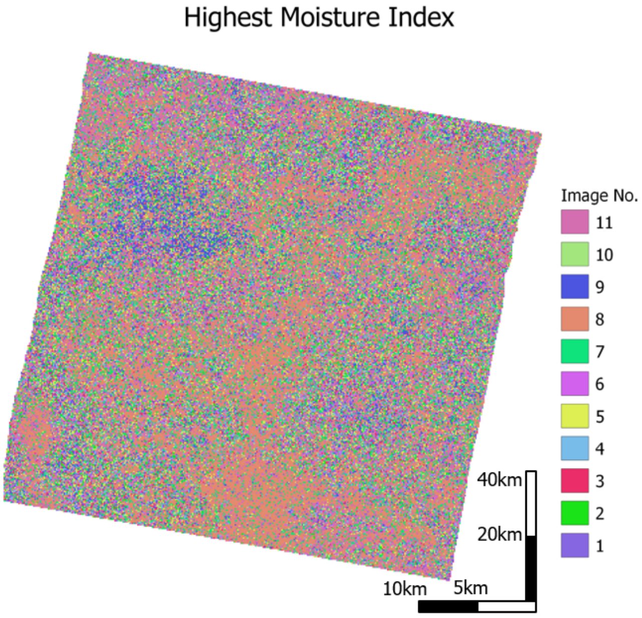

Figure 4.13: Index of the image with the highest moisture level per pixel.

The moisture variation as modelled and as observed by SMAP, per land cover type is presented in Figure 4.14. As stated before, the optimization algorithm is unable to detect all local minima and maxima at all land types. Moreover, the magnitude of moisture changes estimated by the inversion algorithm is lower than the one observed by SMAP. Upon closer inspection, the two land cover types having the lower moisture shifts are the ones with the higher variance (Table 4.2), which in turn are the ones with the most noise, possibly induced by temporal decorrelation, in their results. For example, at areas classified as forest, according to the algorithm, soil moisture barely changes (0.03 m^3/m^3 from max to min) compared to the respective SMAP results (0.13 m^3/m^3 from max to min). On the contrary, urban and sparsely vegetated areas correctly reflect the magnitude of soil moisture change observed by SMAP, albeit doing so with an offset

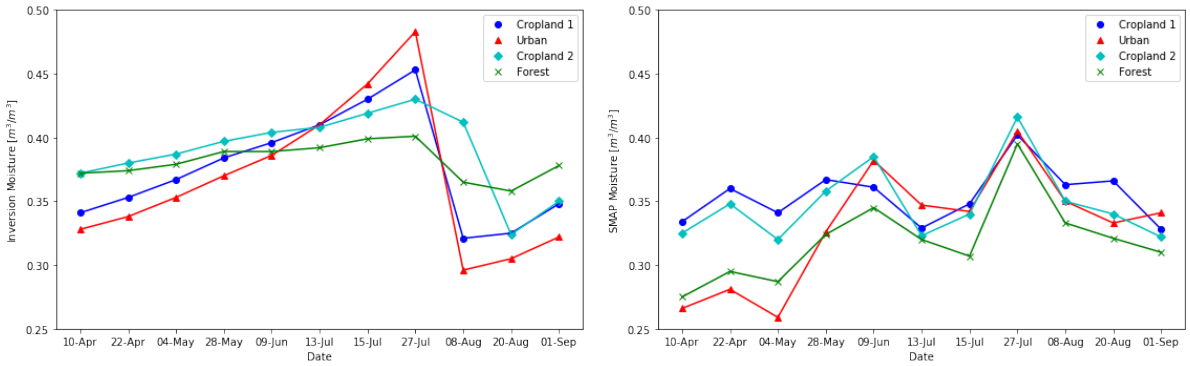

(a) Inversion algorithm (b) SMAP

Figure 4.14: Mexico inversion results for different land types and their respective SMAP values. Cropland 1 refers to the major cropland, while Cropland 2 refers to the northwest region.

4.3.2. Mexico Model 2

In a similar fashion, the results of the second inversion using the 6 acquisitions are presented in Figure 4.16. This model is able to follow the moisture trend (Figure 4.15), similarly to the 1st one. The issue with the local minima remains in this model, since it is unable to detect the moisture drop in acquisition 3 (25/4/2015). Looking back at Tables 3.1 and 4.1 model 2 lags behind the other 3 in terms of available phase information with 66,7& and 81.8% respectively. This means that, on paper, a weaker performance is to be expected from this model due to information deficit. The comparison between the land cover types, is repeated for model 2 and the results are presented in Figure 4.17.

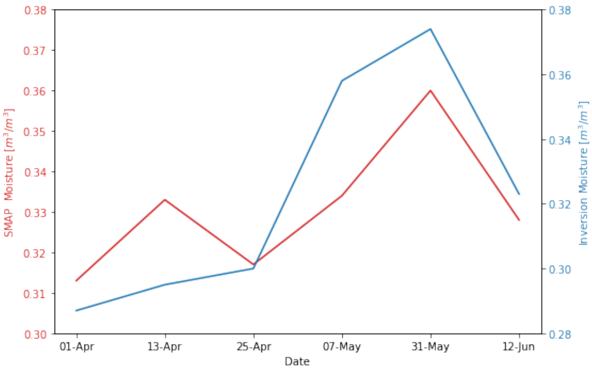

Figure 4.15: Comparison of Mexico Model 2 inversion results with validation data (SMAP).

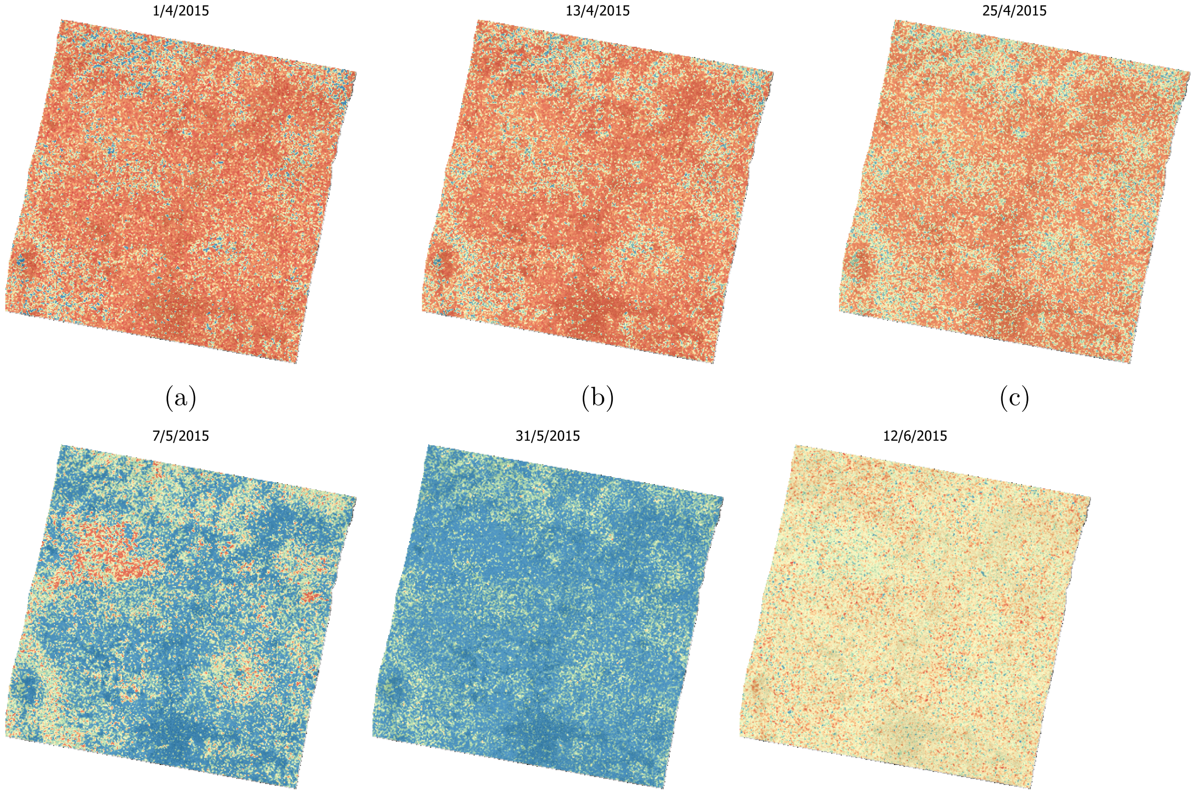

(a) (b) (c)

(d) (e) (f)

Figure 4.16: Volumetric Soil Moisture (m^3/m^3) inversion results for the 6 acquisition Mexico model

A glaring difference compared to Model 1 is that moisture changes and especially their magnitude in forested areas are better predicted by Model 2. Another major difference between the 2 models, is that the quality of the soil moisture prediction deteriorates over urban areas, bare soils and low vegetation. In fact, Model 2 predicts a maximum at image 4, while according to SMAP soil moisture peaks at image 5. Figure 4.11 showed that these land types are marginally affected by temporal decorrelation. Therefore, we can use them to draw a comparison between the 2 models. And since Model 2 can not even correctly estimate the image with the highest moisture level, it is safe to conclude that the information deficit of Model 2 effectively hampers the implementation of the inversion algorithm and can not be compensated by a reduced temporal decorrelation stemming from the shorter total time window.

When comparing the correlation coefficients of al four land cover types between both models (Figure 4.3 one may conclude that Model 2 performs better than Model 1. However, the increase in correlation is biased since there are less data points to correlate (6 instead of 11).

Land cover type	Model 1 (11 SAR images)	Model 2 (6 SAR images)
Urban	0.523	0.819
Cropland 1	0.326	0.542
Cropland 2	0.507	0.647
Forest	0.438	0.949

Table 4.3: Comparison of the correlation coefficients for the four land cover types between Models 1 & 2. Correlation is independent of the magnitude of values so offsets are irrelevant.

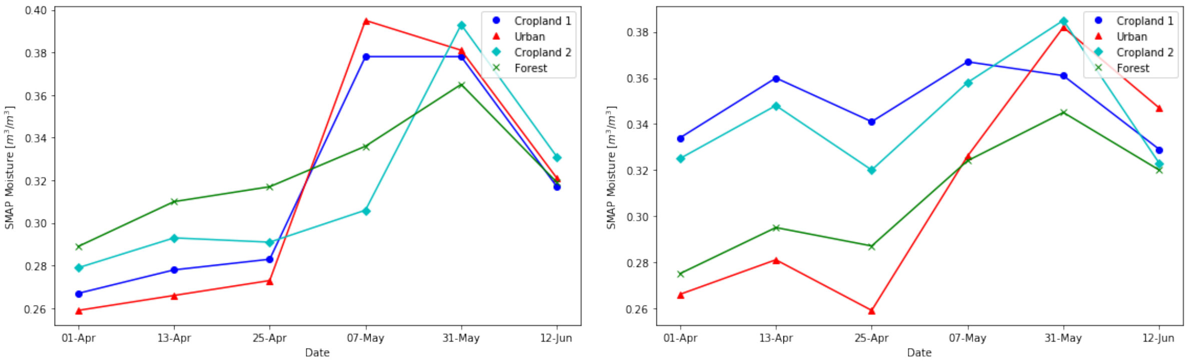

(a) (b)

Figure 4.17: Mexico inversion results for different land types and their respective SMAP values. Cropand 1 refers to the major cropland, while Cropland 2 refers to the northwest region.

4.3.3. Holland Physical & Simplified Model

Moving on the the second study area of this thesis, the first model consists of the same inversion model as the two models implemented for Mexico, while the second model is based on the premises of a simplified inversion model, under the assumption that there is a direct link between closure phases and moisture change. Figures 4.19 & 4.20 present the produced moisture maps of the study area for the physical and the simplified model respectively. Meanwhile, Figure 4.21 compares the inverted moisture sets resulting from both models with SMAP.

Both models show a subpar performance, at least when compared with the study case in Mexico. Neither of the two achieve in following the general moisture trend observed by SMAP. Although the inversion was constrained within limits which were selected to have results similar

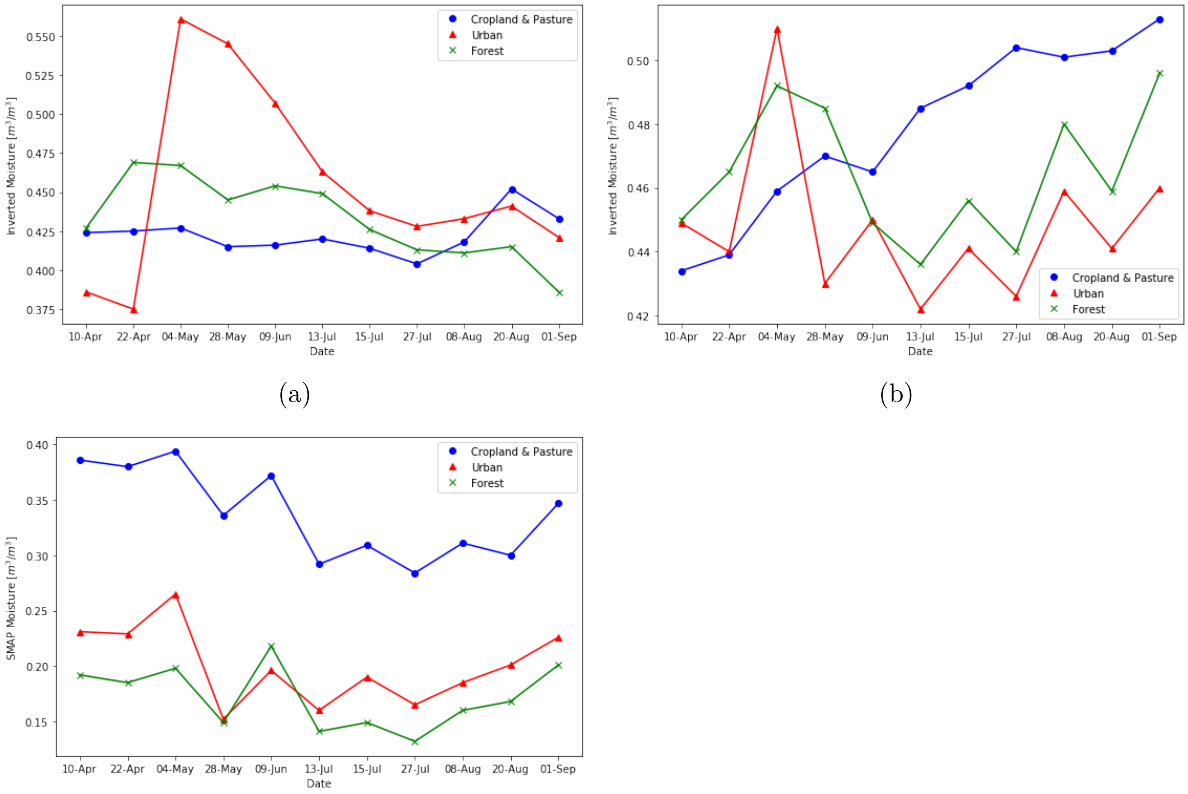

(a)

(b)

(c)

Figure 4.18: Inversion results for the three different land types and their respective SMAP values.

to the ones from SMAP, the moisture value of the initial acquisition far exceeds the respective one from SMAP. This time the inversion algorithm detects more local maxima and minima than it did in Mexico, however these do not correlate well with the moisture values observed by SMAP. Furthermore, both models result in moisture orders which show a high level of variation among each other. Both show significant spatial variability, due to the different land cover types. Consequently, no conclusions can be made, unless these land cover types are investigated. For this region, land cover data were retrieved from (Copernicus-Land Monitoring Service 2015) and 3 major types were selected: Urban, Forest and Cropland. For each land cover type several subsets were selected to get a better grasp of the situation. Both physical and simplified models fail to accurately recreate the moisture trends for croplands, forest and pasture. The correlation coefficient for each model and land cover type is shown in Table 4.4.

In order to attempt to explain the performance of the model over the Netherlands, the decorrelation rate is estimated to evaluate the impact of temporal decorrelation, in a similar manner to what was done in the study area of Mexico. According to Figure 4.22, the coherence decays over time in every land cover type except for the urban type. Croplands, pasture (such as Delfland) and forested areas are quite susceptible to temporal decorrelation, since the decay is almost instantaneous and the long term coherence is almost zero. The decorrelation rate was estimated to be just 6 days for pasture (Delfland) and cropland and 9 days for forest. Based on this findings, the situation in the Netherlands is much more grim than it was in Mexico, because 12 day interval of the Sentinel-1 mission, is not frequent enough to make up for the coherence decay.

Furthermore, in the Netherlands the signal reflected from vegetated areas decorrelates twice as fast as the respective one at Mexico, which may explain the underwhelming results of the

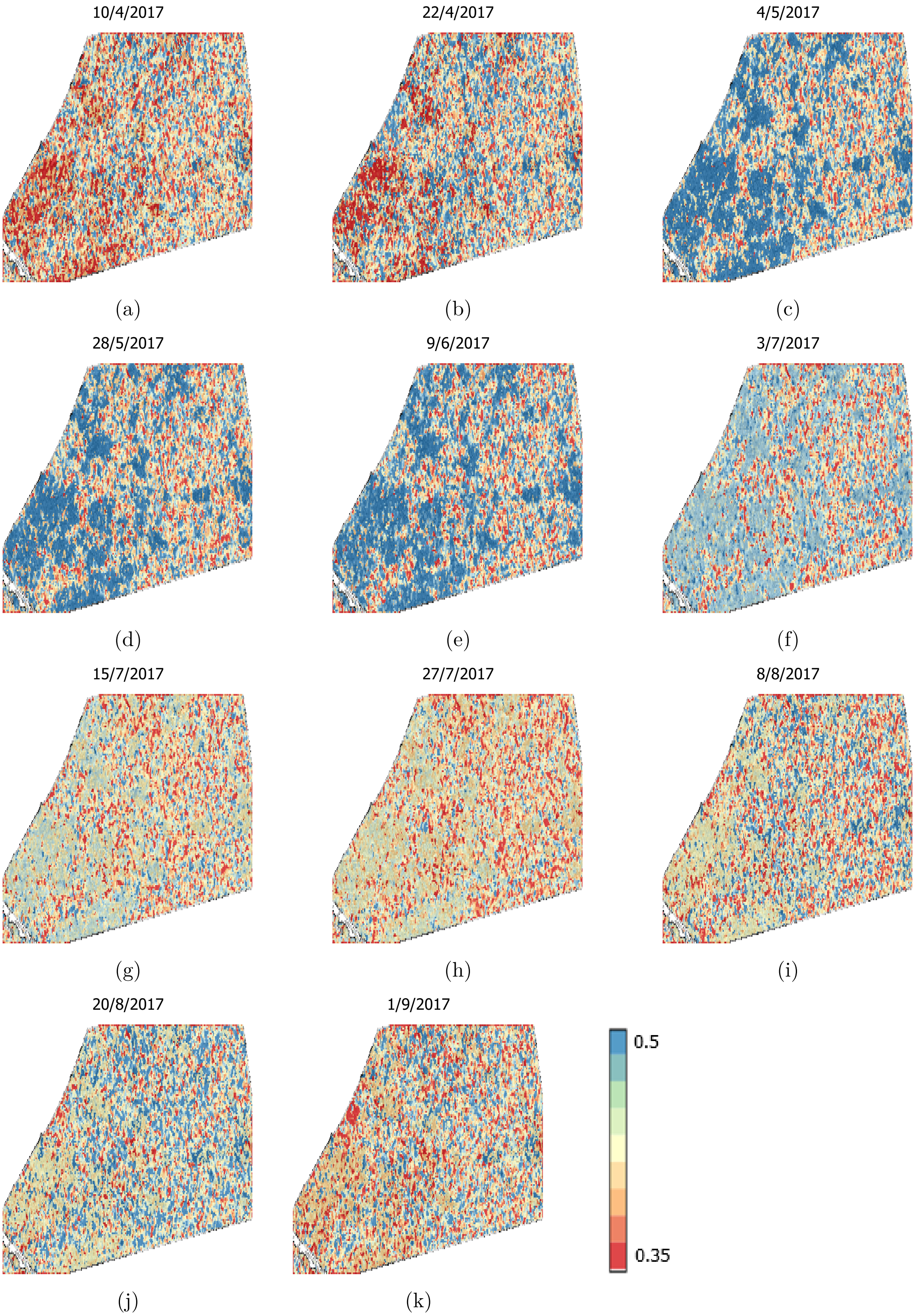

(a) (b) (c) (d) (e) (f) (g) (h) (i) (j) (k)

Figure 4.19: Volumetric Soil Moisture (m^3/m^3) inversion results for the 11 acquisition Physical Holland model

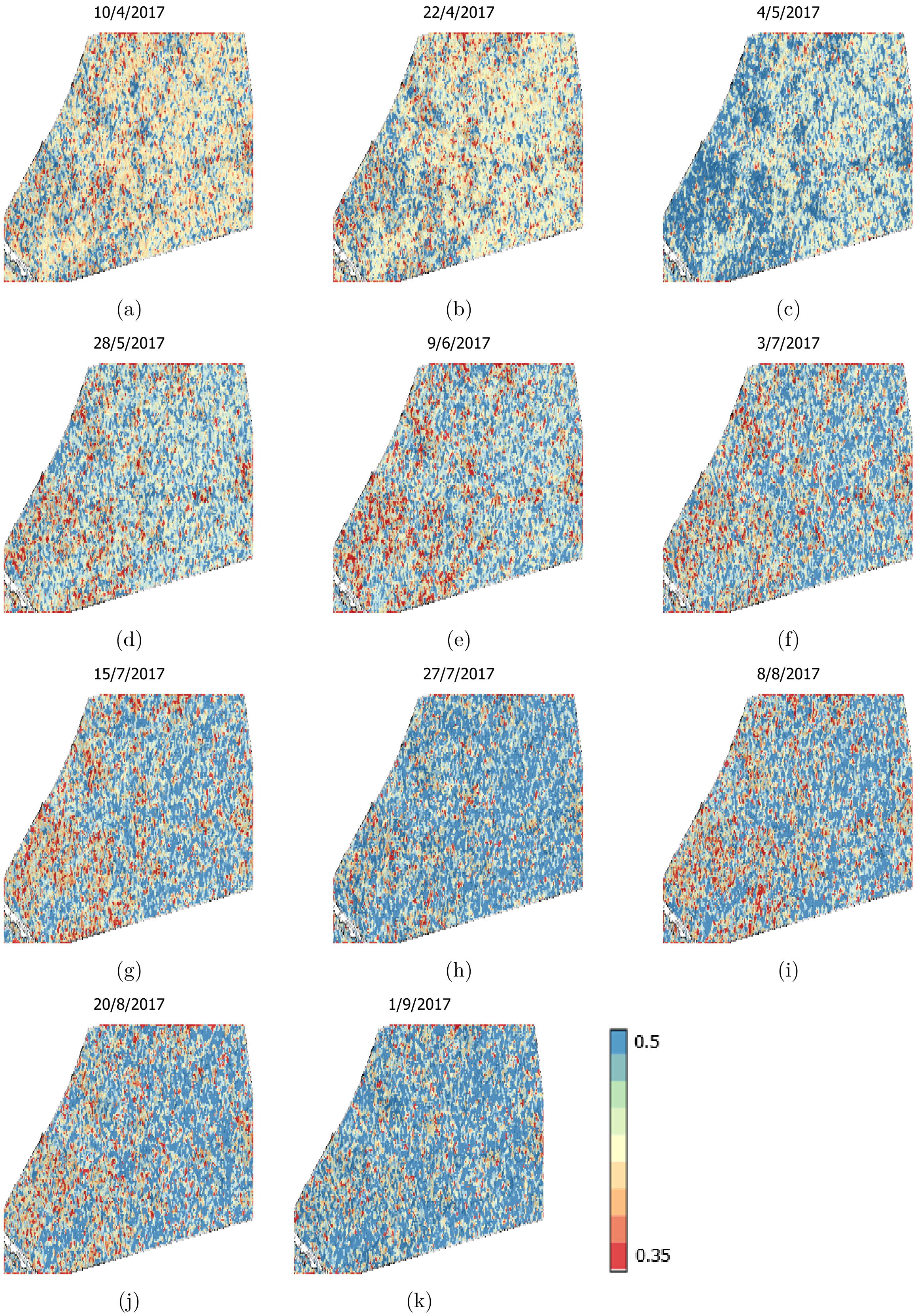

(a) (b) (c) (d) (e) (f) (g) (h) (i) (j) (k)

Figure 4.20: Volumetric Soil Moisture (m^3/m^3) inversion results for the 11 acquisition Simplified Holland model

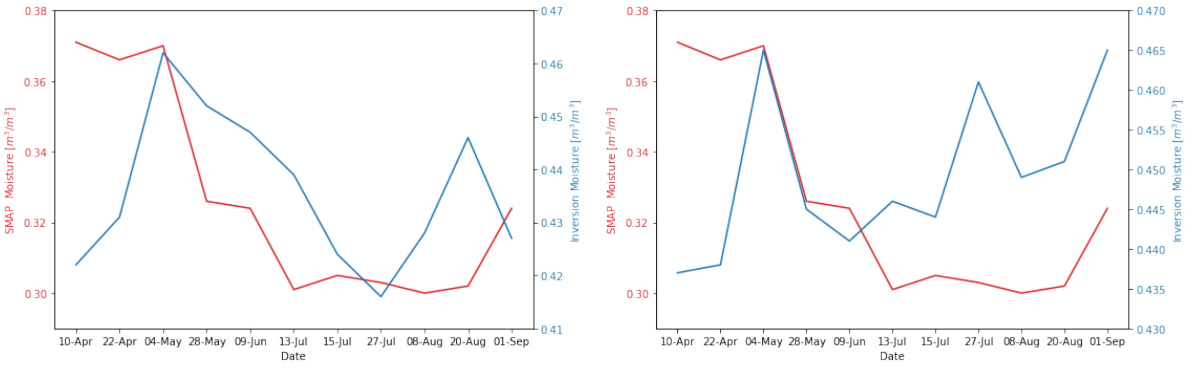

(a) (b)

Figure 4.21: Comparison of the Physical (a) and the Simplified (b) Holland model inversion results with the available validation data (SMAP).

inversion algorithm.

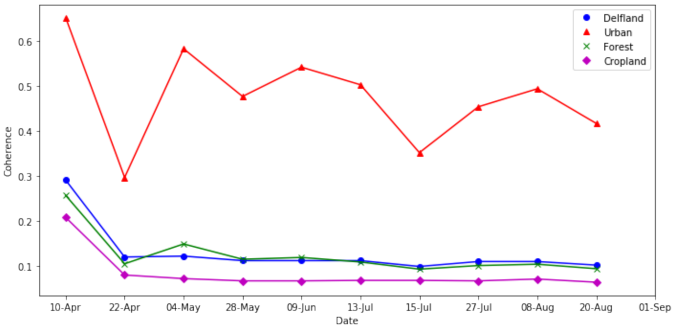

Figure 4.22: Histograms of the decorrelation rate τ for the different land cover types.

Land cover type	Physical Inversion Model	Simplified Inversion Model
Urban	-0.086	0.638
Cropland	0.134	-0.780
Forest	0.186	0.174

Table 4.4: Comparison of the correlation coefficients for the three land cover types between the two employed models.

Another interesting fact about the inversion model employed, is that surface water bodies have non zero phase closure, resulting in moisture change, which is unreal. This ”moisture change” results from the fact that the backscatter above water is very low and thus the coherence is close to zero. Consequently, the SAR signal reflected from water bodies is pure noise.

In order to do some investigation on this phenomenon, the following water bodies were selected to be studied: Westeinderplassen, Braassemermeer, Vinkeveense plassen and the system of Wetlands east of Gouda. Land cover data as well as the selected water bodies are presented in Figure 4.23. The average coherence signal of these water bodies was found to be 0.11 with a maximum of 0.17.This average can now be used as a threshold, to determine whether the signal is pure noise or there is some useful information which can be extracted. Upon examination, the average coherence levels of pasture and cropland does not exceed 0.16, meaning that there is hardly any useful soil moisture information to be extracted ((Wei and Sandwell 2010)).

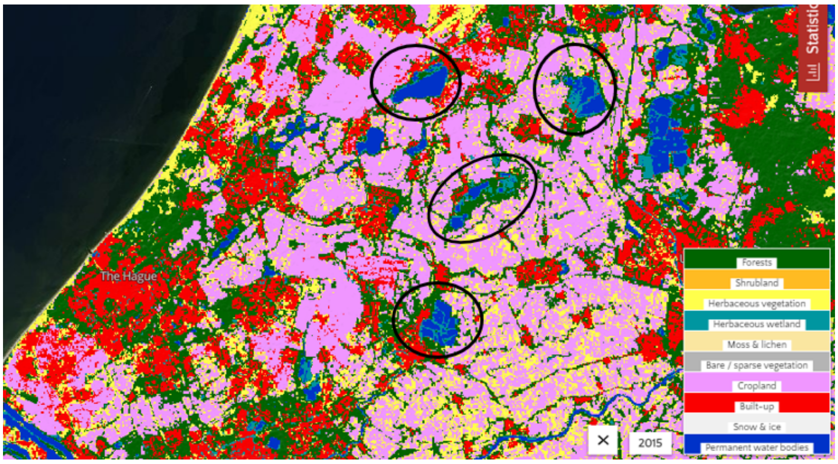

Figure 4.23: The region of Netherlands studied and its land types as detected by (Copernicus-Land Monitoring Service 2015). The water bodies studied are circled.

4.4. Interferometric phase corrections

Determining the moisture sequence, apart from its hydrological interest, enables the correction of interferometric parameters like coherence and phase. Such corrections are essential to InSAR applications where moisture changes induce noise to the system. For this conversion the forward model proposed by De Zan, Parizzi, et al. 2013 is implemented employing the moisture dataset from both study areas.

At this section a couple of examples of compensated phase and displacement correction from each study area will be shown. Regarding Mexico, Figures 4.24 & 4.25 present two typical phase correction maps and a displacement correction respectively.

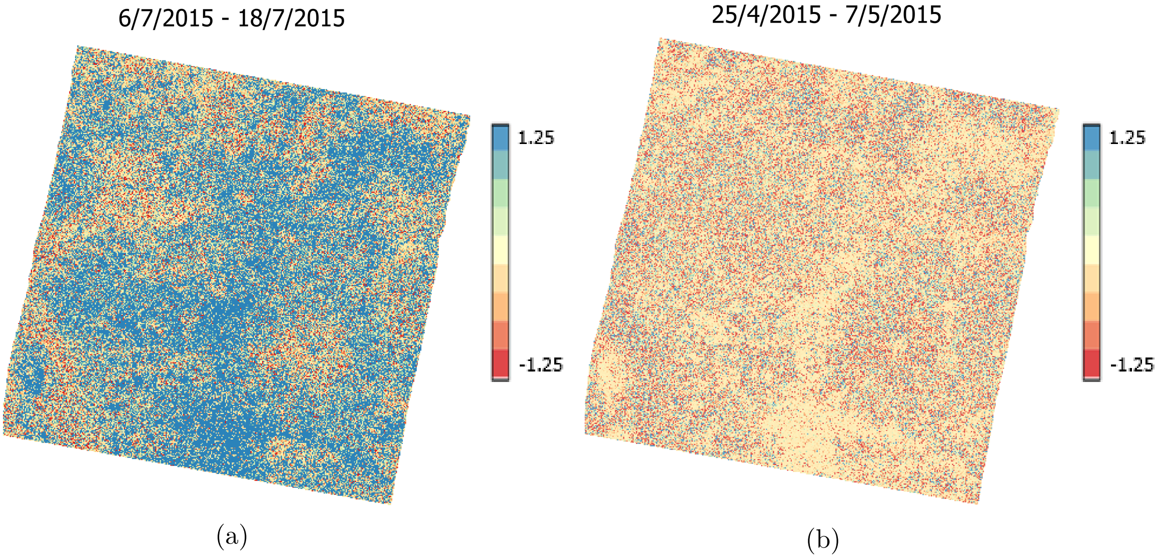

(a)

(b)

Figure 4.24: Compensated interferometric phase (mean Dlos = 0.47mm)(a) and (mean Dlos = -0.14mm) (b)

C-band phase differences can amount up to 5.5 mm per interferogram. Assuming the phase corrections can be stacked, this would result in a total of 15.2 mm land subsidence

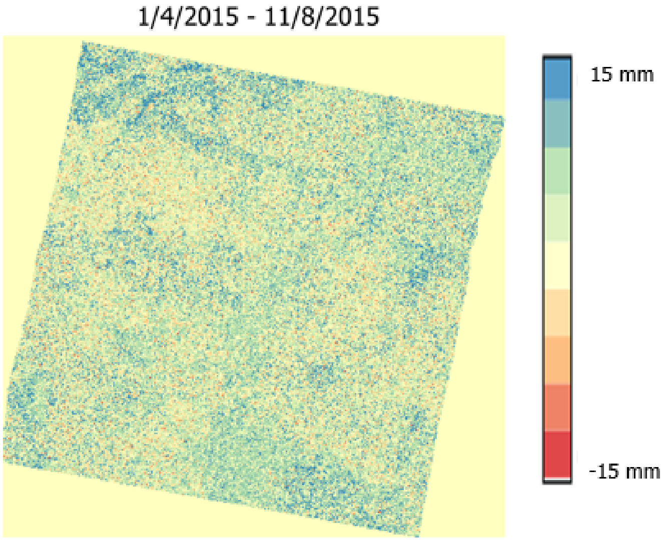

Figure 4.25: Total moisture induced displacement

corrections due to shifts in moisture in a window of 130 days, in the region Puebla. According to Puebla subsides slowly at a rate of 4.4 cm/year, meaning that the signal correction is not at all negligible (false signal up to 1/3 of the yearly subsidence, during the rain season alone).

Regarding the Netherlands, Figure 4.26 presents a typical phase correction map and a displacement correction respectively. Since both models performed poorly, the resulting correction are expected to not reflect reality. Nevertheless, it is still interesting to see what are the reading in Delfland. The maximum deformation is 11 mm over 140 days of summer with little precipitation. Since the physical model underestimated the moisture shift, the real one can rank even higher.

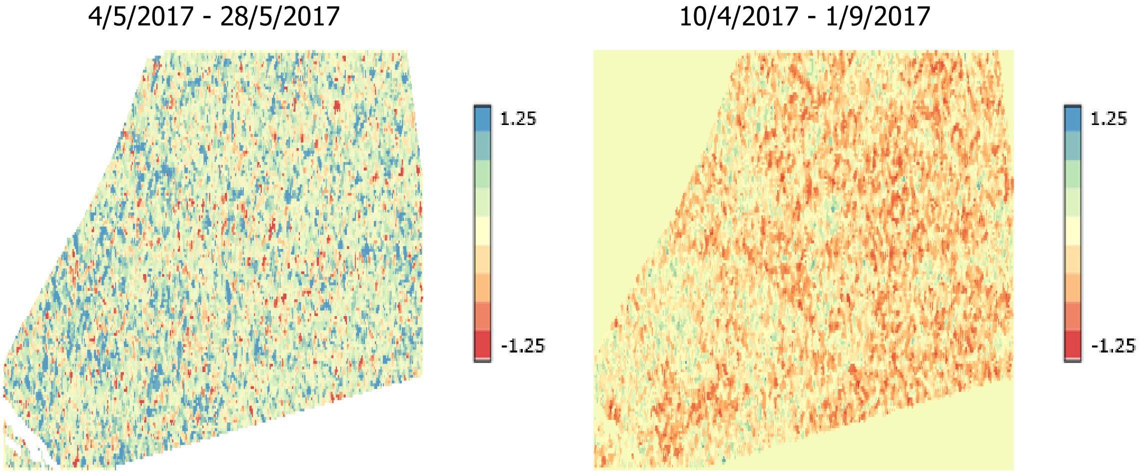

(a) (b)

Figure 4.26: Compensated interferometric phase (mean Dlos = 0.47mm)(a) and Total moisture induced displacement (b)

5

Conclusions & Recommendations

In this thesis, the potential of Sentinel-1 C-band phase closure as a tool to estimate soil moisture and the associated correction in InSAR parameters has been studied. To be more specific, two alternatives of the Interferometric Model for Soil Moisture introduced by De Zan, Parizzi, et al. 2013, De Zan and Gomba 2018 and reinforced by the contribution of Zwieback, Hensley, and Hajnsek 2017 are applied in two study areas: Puebla region in Mexico and Zuid & Nord-Holland in the Netherlands.

This chapter will give short answers to the individual research questions set in the early stages of the research. Finally, a couple of recommendations for further research on the topic will be presented.

5.1. Conclusions

The main research question is:

Is it possible to detect soil moisture changes with the method of closure phase inversion, using Sentinel-1 C-band data?

This question will be answered by answering the sub questions.

- Does the phase closure inversion method proposed by De Zan work in C-band?

Based on the findings of this thesis, C-band Sentinel-1 product has indeed the potential to be used for this purpose. However, there are certain conditions which have to be met for the successful inversion. The results showed that the current state and setup of the algorithm does not have the ability to overcome vegetation at least not with the 12-day repeat interval. The algorithm generated consistent soil moisture products over bare soils and areas with low vegetation, however the quality deteriorated when vegetation came into play. According to the pixel statistics at Table 4.2 and Figure 4.13, the chances of each of the 11 images to be identified as the one with the moisture maximum were spread evenly with a noticeable edge given to the actually correct one. This implies that the potential is there, however the current results are far from satisfactory.

- How does land cover affect the closure phase dataset?

Land cover dictates the level of coherence between images to a certian extent. Therefore it is inadvertently responsible for the closure phase signal as well. As a general rule of thumb, low coherence generates strong and noise plagued phase signal, which makes extracting useful data highly unlikely, at least with the methodology employed. This was quite apparent in the Netherlands where vegetated areas were inndistinguishable from water bodies in terms of coherence levels. All in all, a consistently high magnitude closure phase signal deters the inversion algorithm from solving the circular ambiguities and discern the underlying soil moisture patterns.

- Is the detected moisture spatially consistent with land cover?

The consistency seem to depend entirely on the land cover type. Looking at the results, it is apparent that areas in Mexico with little to no vegetation generate a highly consistent signal, but the quality decays over areas with dense vegetation, in Mexico and the Netherlands alike. The investigation conducted showed that this decay is directly associated with the increased decorrelation rate over vegetated areas.
The fact that the Mexico model managed to generate two spatially discrete moisture patterns over the same land cover type (cropland 1 and 2), shows that the potential is indeed there, but more research is required to overcome the issues which were identified at this thesis.

- Can soil moisture be used to reduce the uncertainty of land deformation values obtained with InSAR?

All findings point to the soil moisture being able to reduce the uncertainty. In Mexico, for example, the phase compensation was not negligible at all. Additionally, in Delfland where the physical model underestimated the local soil moisture changes heavily, the total deformation signal was almost equal to the one in Mexico (15.2mm to 14.4mm). Consequently, soil moisture signal could be pivotal in alleviating land deformation measurements from a certain degree of uncertainty.

5.2. Recommendations

- The results of the phase closure inversion algorithm in the Netherlands left a lot to be desired, especially in comparison with Mexico. The physical model using the Halikkainen empirical dielectric constant was imperfect for this area since organics were not being accounted for. It would be certainly interesting to look into it, in order to broaden its field of application.

- To my surprise, urban areas in Mexico provided a clear ”soil moisture” coherent with SMAP observations. Moreover, the quality of the results was on par with those over bare soil/ low vegetated areas. My assumption is that it has to do with the urban drainage infrastructure and urban texture overall. Although the result can not be actual soil moisture, it is intriguing to find out more about this interaction.

- So far, and apart from this thesis, only L-band data have been used to replicate this method. In theory due to the longer wavelength, ergo larger penetration L-band is indeed a more suitable choice. It would be wise to use both L-band and C-band, maybe also Ku-band on the same study area as a means to get tangible comparable results.

- This method is not very efficient as it requires a large amount of data and has it’s fair share of pre-processing between acquiring the SAR images and producing the moisture maps. Due to the ambiguities plaguing phase closures, the optimization process needs a large number of repetitions in order to have a good cross section of potential solutions. This, together with the number of the SAR images employed and a potentially large grid size, means that the computing power required is substantial. i would recommend using a a terminal with parallel computing or partitioning the process.

- According to Monnier, Perrin, and Malbet 2003 the available phase information acquired from phase closures is directly linked to the number of images in use. In this thesis sets of 11 images were used, meaning that just 82% ofphase information was at my disposal. This gap can be diminished by using a time series consisting of more acquisitions. This was not able to be done during this study due to the limited resources available. It would be interesting to investigate the implementation of this method on a larger SAR dataset. Of course that would introduce even greater amounts of temporal decorrelation over vegetated areas.

- In both areas the decorrelation rate was higher or equal to the repeat interval. As a result the phase signal was plagued with temporal decorrelation. It is suggested to repeat this method, involving techniques to thicken the dataset. A possible solution could be to use multipolar InSAR.

- Although this research was initiated with the phase corrections in mind as an endgoal, further research on its applicability and efficiency purely for hydrological purposes would be advised. Maybe it could be used in tandem with a ground truthing network comprising of soil moisture sensing stations, even operated by citizen scientists.

Bibliography

Aalbers, E. E. (2015). Evaporation in conceptual rainfall-runoff models: Testing model realism using remotely sensed evaporation. URL: https://repository.tudelft.nl/islandora/object/uuid%5C%3Aa2edc688-2270-4823-aa93-cb861cf481a2.

Actueel Hoogtebestand Nederland (n.d.). Actueel Hoogtebestand Nederland. URL: http://ahn.nl.

Albinet, Clement et al. (2012). "TropiSCAT: A ground based polarimetric scatterometer experiment in tropical forests". In: IEEE Journal of Selected Topics in Applied Earth Observations and Remote Sensing 5.3, pp. 1060–1066.

Bodemdalingskaart (2018). Actuele Bodemdalingskaart Nederland. URL: https://bodemdalingskaart.nl/.

Brocca, Luca, Florisa Melone, and T. Moramarco (2005). "Empirical and conceptual approaches for soil moisture estimation in view of event-based rainfall-runoff modeling". In: Technical Documents in Hydrology 77, pp. 1–8.

Brus, DJ, FPJ Lame, and RH Nieuwenhuis (2009). "National baseline survey of soil quality in the Netherlands". In: Environmental Pollution 157.7, pp. 2043–2052.

climate-data.org (n.d.). Climate-Data org. URL: https://en.climate-data.org.

Copernicus-Land Monitoring Service (2015). Global Land Cover. URL: https://lcviewer.vito.be/.

De Zan, Francesco and Giorgio Gomba (2018). "Vegetation and soil moisture inversion from SAR closure phases: First experiments and results". In: Remote sensing of environment 217, pp. 562–572. DOI: https://doi.org/10.1016/j.rse.2018.08.034.

De Zan, Francesco, Giorgio Gomba, and Natsumi Yokoya (2018). "The ambiguities related to Closure-Phase Model Inversion". In: EUSAR 2018; 12th European Conference on Synthetic Aperture Radar. VDE, pp. 1–4.

— (n.d.). Soil Moisture and Closure Phases. Tech. rep. DLR.

De Zan, Francesco, Alessandro Parizzi, et al. (2013). "A SAR interferometric model for soil moisture". In: IEEE Transactions on Geoscience and Remote Sensing 52.1, pp. 418–425. DOI: 10.1109/TGRS.2013.2241069.

De Zan, Francesco, Mariantonietta Zonno, and Paco López-Dekker (2015). "Phase inconsistencies and multiple scattering in SAR interferometry". In: IEEE Transactions on Geoscience and Remote Sensing 53.12, pp. 6608–6616.

DINOloket (n.d.). DINOloket, Data and Information from the Dutch Subsurface. URL: http://dinoloket.nl.

Dobson, Myron C et al. (1985). "Microwave dielectric behavior of wet soil-Part II: Dielectric mixing models". In: IEEE Transactions on Geoscience and Remote Sensing 1, pp. 35–46.

Duerinck, H. M. (2014). Observed soil moisture - precipitation feedback in Illinois: A statistical analysis over different scales. URL: https://repository.tudelft.nl/islandora/object/uuid%5C%3A44197cb1-3b6e-40c1-b7a4-981475cb1221?collection=education.

Engdahl, Marcus et al. (2013). "Multitemporal InSAR in land-cover and vegetation mapping". In:

Engen, Gier and Harald Johnsen (2010). "Sentinel-1 Doppler and ocean radial velocity (RVL) algorithm definition,"" in: Tromsø: Northern Research Institute.

Ent, Rudi van der et al. (2010). "Origin and fate of atmospheric moisture over continents". In: Water Resources Research 46.9. DOI: 10.1029/2010WR009127.

Event Horizon Telescope (2019). Astronomers Capture First Image of a Black Hole. URL: https://eventhorizontelescope.org/.

Fenicia, F et al. (2006). "Is the groundwater reservoir linear? Learning from data in hydrological modelling". In: Hydrology and Earth System Sciences Discussions 10.1, pp. 139–150.

Fernández, Jaime et al. (2015). "Copernicus POD service operations—Orbital accuracy of Sentinel-1A and Sentinel-2A". In: Proc. Int. Symp. Space Flight Dyn, pp. 1–14.

Ferrari, Luca (2003). "The geochemical puzzle of the Trans-Mexican Volcanic Belt: mantle plume, continental rifting, or mantle perturbation induced by subduction?" In: Mexico2.html" N.

Ferretti, A et al. (2007). "InSAR Principles-Guidelines for SAR Interferometry Processing and Interpretation". In: The Netherlands: ESA Publications.

Gómez-Tuena, Arturo et al. (2003). "Temporal control of subduction magmatism in the eastern Trans-Mexican Volcanic Belt: Mantle sources, slab contributions, and crustal contamination". In: Geochemistry, Geophysics, Geosystems 4.8.

Hallikainen, Martti T et al. (1985). "Microwave dielectric behavior of wet soil-part 1: Empirical models and experimental observations". In: IEEE Transactions on Geoscience and Remote Sensing 1, pp. 25–34.

Hanssen, R. F. (2001). Radar Interferometry; Data Interpretation and Error Analysis. Vol. 2. Dordrecht: Kluwer Academic Publishers.

Jin, Mengjie et al. (2017). "Evaluation and improvement of SMOS and SMAP soil moisture products for soils with high organic matter over a forested area in Northeast China". In: Remote Sensing 9.4, p. 387.

Karim, Nurul Izzati Abd, Samira Albati Kamaruddin, and Rozaimi Che Hasan (2018). "The Petrophysical Relationship between the Dielectric Permittivity and Water Content of Peat Soil Moisture Measurements". In: 2018 2nd International Conference on Smart Sensors and Application (ICSSA). IEEE, pp. 147–151.

Koninklijk Nederlands Meteorologisch Instituut (2019). Monthly precipitation observations. URL: https://climexp.knmi.nl.

Kottek, Markus et al. (2006). "World map of the Köppen-Geiger climate classification updated". In: Meteorologische Zeitschrift 15.3, pp. 259–263.

Lal, Rattan et al. (1994). Soil erosion research methods. CRC Press.

Legates, David et al. (2010). “Soil moisture: A central and unifying theme in physical geography”. In: Progress in Physical Geography: Earth and Environment 35.1, pp. 65–86. DOI: 10.1177/0309133310386514.

Lesschen, Jan Peter et al. (2012). Mogelijkheden voor koolstofvastlegging in de Nederlandse landbouw en natuur. Tech. rep. Alterra.

Liu, Jun et al. (2013). “The influence of organic matter on soil dielectric constant at microwave frequencies (0.5–40 GHZ)”. In: 2013 IEEE International Geoscience and Remote Sensing Symposium-IGARSS. IEEE, pp. 13–16.

Lumen Physical geography (2017). Factors that Influence Mass Wasting. URL: https://courses.lumenlearning.com/geophysical/chapter/factors-that-influence-mass-wasting/.

Marc Hijma (2017). Geology of the Dutch coast. The effect of lithological variation on coastal morphodynamics. [Online; accessed 1-October-2019]. URL: http://publications.deltares.nl/1220040_007_0003.pdf.

Mialon, Arnaud et al. (2015). “Comparison of Dobson and Mironov dielectric models in the SMOS soil moisture retrieval algorithm”. In: IEEE Transactions on Geoscience and Remote Sensing 53.6, pp. 3084–3094.

Mironov, Valery L and Pavel P Bobrov (2003). “Soil dielectric spectroscopic parameters dependence on humus content”. In: IGARSS 2003. 2003 IEEE International Geoscience and Remote Sensing Symposium. Proceedings (IEEE Cat. No. 03CH37477). Vol. 2. IEEE, pp. 1106–1108.

Mironov, Valery L and Sergey V Fomin (2009). “Temperature and mineralogy dependable model for microwave dielectric spectra of moist soils”. In: Piers online 5.5, pp. 411–415.

Mohanty, Binayak P et al. (2017). “Soil moisture remote sensing: State-of-the-science”. In: Vadose Zone Journal 16.1.

Monnier, JD, G Perrin, and F Malbet (2003). “Astrophysics with closure phases”. In: European Astronomical Society Publications Series 6, pp. 213–213.

Morishita, Yu and Ramon Hanssen (2014). “Temporal decorrelation in L-, C-, and X-band satellite radar interferometry for pasture on drained peat soils”. In: IEEE Transactions on Geoscience and Remote Sensing 53.2, pp. 1096–1104.

Morrison, Keith et al. (2011). “Laboratory measurement of the DInSAR response to spatiotemporal variations in soil moisture”. In: IEEE Transactions on Geoscience and Remote Sensing 49.10, pp. 3815–3823.

National Aeronautics and Space Administration (2015). NASA Soil Moisture Radar Ends Operations, Mission Science Continues. URL: https://www.jpl.nasa.gov/news/news.php?feature=4710.

National Snow Ice Data Center (n.d.). SMAP L4 Global 3-hourly 9 km EASE-Grid Surface and Root Zone Soil Moisture Analysis Update, Version 4 SMAP Level-4 (L4) surface and root zone soil moisture data are provided in three products: URL: https://nsidc.org/

data/spl4smau/?_ga=2.117485321.1285382400.1561025765-588684023.1557361871.

Nitti, Davide Oscar et al. (2010). “Impact of DEM-assisted coregistration on high-resolution SAR interferometry”. In: IEEE Transactions on Geoscience and Remote Sensing 49.3, pp. 1127–1143.

Owe, Manfred and Adriaan A Van de Griend (1998). “Comparison of soil moisture penetration depths for several bare soils at two microwave frequencies and implications for remote sensing”. In: Water resources research 34.9, pp. 2319–2327.

Paloscia, S et al. (2013). “Soil moisture mapping using Sentinel-1 images: Algorithm and preliminary validation”. In: Remote Sensing of Environment 134, pp. 234–248.

Ravi, Sujith et al. (2010). “Land degradation in drylands: Interactions among hydrologic–aeolian erosion and vegetation dynamics”. In: Geomorphology 116.3-4, pp. 236–245.

Ray, Ram L, Jennifer M Jacobs, and Pedro de Alba (2010). “Impacts of unsaturated zone soil moisture and groundwater table on slope instability”. In: Journal of geotechnical and geoenvironmental engineering 136.10, pp. 1448–1458.

Samiei Esfahany, S (2017). “Exploitation of distributed scatterers in synthetic aperture radar interferometry”. In: DOI: 10.4233/uuid:22d46f1e-9061-46b0-9726-760c41404b6f.

Sansosti, Eugenio et al. (2006). “Geometrical SAR image registration”. In: IEEE Transactions on Geoscience and Remote Sensing 44.10, pp. 2861–2870.

Schubert, Adrian et al. (2014). “Spaceborne SAR product geolocation accuracy: A Sentinel-1 update”. In: 2014 IEEE Geoscience and Remote Sensing Symposium. IEEE, pp. 2675–2678.

Segura-Castruita, Miguel A (2006). “Soil Characteristics Determining the Soil Water Retention of Soil from Pumiceous Origin From Puebla-Tlaxcala Valley, Mexico.” In: The 18th World Congress of Soil Science.

STEP ESA (n.d.). SNAP - ESA Sentinel Application Platform v2.0.2. URL: http://step.esa.int/main/.

Thienen-Visser, K van, JP Pruiksma, and JN Breunese (2015). “Compaction and subsidence of the Groningen gas field in the Netherlands”. In: Proceedings of the International Association of Hydrological Sciences 372, pp. 367–373.

Thomas, David and Nick Middleton (1997). World atlas of desertification. Arnold.

Tobita, Mikio et al. (1998). “Deformation of the 1995 North Sakhalin earthquake detected by JERS-1/SAR interferometry”. In: Earth, Planets and Space 50.4, pp. 313–325.

Tohari, Adrin, Makoto Nishigaki, and Mitsuru Komatsu (2007). “Laboratory rainfall-induced slope failure with moisture content measurement”. In: Journal of Geotechnical and Geoenvironmental Engineering 133.5, pp. 575–587.

Urbina-Flores, DP et al. (2016). “Microbiological and physico-chemical characterization of soil of an agroforestry system in Tetela de Ocampo, Puebla Mexico”. In: Journal of Pure and Applied Microbiology 10.2, pp. 915–923.

Wagner, Wolfgang, Guido Lemoine, and Helmut Rott (1999). “A method for estimating soil moisture from ERS scatterometer and soil data”. In: Remote sensing of environment 70.2, pp. 191–207.

Wei, Meng and David T Sandwell (2010). “Decorrelation of L-band and C-band interferometry over vegetated areas in California”. In: IEEE Transactions on Geoscience and Remote Sensing 48.7, pp. 2942–2952.

Yoshimura, K. et al. (2004). “Colored moisture analysis estimates of variations in 1998 Asian monsoon water sources”. In: Journal of the Meteorological Society of Japan 82.5, pp. 1315–1329. DOI: `10.2151/jmsj.2004.1315`.

Zhang, Dianjun and Guoqing Zhou (2016). “Estimation of soil moisture from optical and thermal remote sensing: A review”. In: Sensors 16.8, p. 1308.

Zwieback, Simon, Scott Hensley, and Irena Hajnsek (2015a). “A polarimetric first-order model of soil moisture effects on the DInSAR coherence”. In: Remote Sensing 7.6, pp. 7571–7596.

— (2015b). “Assessment of soil moisture effects on L-band radar interferometry”. In: Remote Sensing of Environment 164, pp. 77–89.

— (2017). “Soil moisture estimation using differential radar interferometry: Toward separating soil moisture and displacements”. In: IEEE Transactions on Geoscience and Remote Sensing 55.9, pp. 5069–5083.

Zwieback, Simon, Xingyu Liu, et al. (2016). “A statistical test of phase closure to detect influences on DInSAR deformation estimates besides displacements and decorrelation noise: Two case studies in high-latitude regions”. In: IEEE Transactions on Geoscience and Remote Sensing 54.9, pp. 5588–5601.